TITLE: ELECTRICALLY CONDUCTIVE, CORROSION-RESISTANT COATINGS THROUGH DEFECT CHEMISTRY FOR METALLIC INTERCONNECTS

Type of report: Final Technical Report

Reporting Period Start Date: October 1, 2004

Reporting Period End Date: December 31, 2006

Principal Author: Professor Anil V. Virkar

DOE Award Number: DE-FC26-04NT42220

Date Report Was Issued: May 11, 2007

Name and Address of Submitting Organization:

Department of Materials Science & Engineering
University of Utah
122 S. central Campus Drive
Salt Lake City, UT 84112
Anil V. Virkar (801) 581-5396
anil.virkar@m.cc.utah.edu

SCNG Contact: Ayyakkannu Manivannan: (304) 285-2078
ayyakkannu.manivannan@netl.doe.gov

Project Timeline: Start: 10/1/2004
End: 3/31/2006

Total Project Cost:		
	Total:	$372,004.00
	DOE Share:	$297,004.00
	Non-DOE:	$75,000.00

ABSTRACT

The principal objective of this work was to develop oxidation protective coatings for metallic interconnect based on a defect chemistry approach. It was reasoned that the effectiveness of a coating is dictated by oxygen permeation kinetics; the slower the permeation kinetics, the better the protection. All protective coating materials investigated to date are either perovskites or spinels containing metals exhibiting multiple valence states (Co, Fe, Mn, Cr, etc.). As a result, all of these oxides exhibit a reasonable level of electronic conductivity; typically at least about ~0.05 S/cm at 800°C. For a 5 micron coating, this equates to a maximum ~0.025 Ωcm^2 area specific resistance due to the coating. This suggests that the coating should be based on oxygen ion conductivity (the lower the better) and not on electronic conductivity. Measurements of ionic conductivity of prospective coating materials were conducted using Hebb-Wagner method. It was demonstrated that special precautions need to be taken to measure oxygen ion conductivity in these materials with very low oxygen vacancy concentration.

A model for oxidation under a protective coating is presented. Defect chemistry based approach was developed such that by suitably doping, oxygen vacancy concentration was suppressed, thus suppressing oxygen ion transport and increasing effectiveness of the coating. For the cathode side, the best coating material identified was $LaMnO_3$ with Ti dopant on the Mn site (LTM). It was observed that LTM is more than 20 times as effective as Mn-containing spinels. On the anode side, $LaCrO_3$ doped with Nb on the Cr site (LNC) was the material identified. Extensive oxidation kinetics studies were conducted on metallic alloy foils with coating ~1 micron in thickness. From these studies, it was projected that a 5 micron coating would be sufficient to ensure 40,000 h life.

TABLE OF CONTENTS

EXECUTIVE SUMMARY

Defect chemistry based approach was successfully used to identify prospective coating materials with very low oxygen transport properties; a principal requirement for a satisfactory coating on metallic interconnects. The materials identified were Ti-doped $LaMnO_3$ (LMT) and Nb-doped $LaCrO_3$ (LNC). As little as one micron coating was found to be very effective in suppressing oxidation kinetics. For example, it was shown that LMT was more than ten times effective in suppressing oxidation kinetics of metallic interconnect as a Mn-Cr-spinel. In fact, based on all of the reported coating materials, normalized for coating thickness (that is, comparison based on the same coating thickness), the coating materials developed in Phase I are superior to all other coating materials reported to date. In order to identify coating materials with low oxygen transport, oxygen ion conductivity was measured using the Hebb-Wagner blocking electrode method. Thin coatings were deposited on stainless steels as well as on nickel-based alloys. For screening purposes, prospective coatings were deposited by sputtering. The choice of sputtering was made since it allows the deposition of ultra-thin, dense coatings, necessary for a systematic study of oxidation kinetics and assessment of coating effectiveness. If the coating is too thick, it is not possible to obtain sufficient information concerning oxidation kinetics in a reasonable period of time. That is, to obtain kinetic parameters that describe the kinetics of oxidation, it is necessary that the coating be sufficiently thin. Efforts were also devoted towards the development of a low-cost process, without using sputtering. It was demonstrated that a ~6 micron coating could be successfully deposited on SS430. Important results from Phase I work are listed below.

1) The proposed defect chemistry-based approach was successfully demonstrated. It was shown that LMT coating was the most effective one and LSM was the least effective of the materials investigated[1]. A point to emphasize is that LSM coating has already been shown to be more effective in suppressing oxidation kinetics than Mn-Cr spinel. It was shown that a mere 1 micron coating of $LaMn_{0.9}Ti_{0.1}O_3$ (LMT) was effective in drastically suppressing oxidation kinetics of nickel-based alloy foils. Maximum oxide scale thickness formed after 45 days (1080 hours) of thermal treatment at 800^oC in air was only 0.7 micron. The corresponding ASR at 800^oC was ~12 $m\Omega cm^2$ (0.012 Ωcm^2). Projected thickness of the oxide scale after 40,000 hours with a 5 micron coating is ~4.5 microns only, with a projected ASR of ~61 $m\Omega cm^2$ (~0.061 Ωcm^2). Substantially improved oxidation resistance was also observed on coated SS430 foils.

2) Excellent oxidation resistance was also observed in SS430 foils coated with $LaCrO_3$-based coatings. A mere 1 micron coating decreased the oxidation kinetics by more than an order of magnitude. It was observed that in uncoated samples, after 14 days at 800^oC in humidified hydrogen, the oxide scale thickness was ~7 microns. However, that in the samples coated with a 1 micron $LaCrO_3$-based coating, the oxide scale thickness was less than 0.7 microns. Experiments are underway for longer times.

---

[1] Prior work has already shown that LSM is more than three times as effective as Mn-Cr-spinel. Thus, LMT is ten times as effective as the spinel coating.

3) Excellent oxidation resistance was also observed on SS430 foils coated with LMT. A mere 1 micron coating decreased the oxidation kinetics by a factor of 6, when oxidized in air in a 7 day test. Experiments are underway for longer times.

4) The area specific resistance (ASR) measurements on the coated (1 micron) and uncoated foils showed that after 45 days in air at 800°C, the ASR of the coated foils was typically less than one third that of uncoated foils. The measured ASR after 45 days (1080 hours) oxidation was typically less than 12 $m\Omega cm^2$ ($0.012\ \Omega cm^2$). Even lower ASR is expected with thicker (~5 micron) coatings.

5) Experiments were conducted on the measurement of oxygen ion conductivity using blocking electrodes at 800^0C. Results showed that the blocking electrodes function successfully. It was decided to use a three electrode configuration (with guard electrode) to eliminate the effects of surface conductivity. Lower values of conductivity were obtained for the sputter coated YSZ/perovskite couple as compared to the co-pressed sandwich structure. This was attributed to better equilibration to steady state in the thinner (sputter deposited) samples. The lowest value of conductivity was 2.0×10^{-7} Scm^{-1} and was obtained for LMT

6) Preliminary work conducted on the development of thin coatings by a low-cost process, which can in principle be easily scaled to mass production methods, was successful. The low-cost process, is hot-rolling (hot-forming). For future work the approach would consist of screen-printing fine powder of the prospective coating materials (the ones for the cathode side and the anode side will likely be different) on commercially available stainless steel foils followed by hot-rolling.

REPORT DETAILS

Proposed Tasks:

Task 1.0 – Identification of Suitable Non-Perovskite Oxide Materials and Fabrication and characterization of Non-Perovskite Materials, $LaMnO_3$ (LaMn), Ti-doped $LaMnO_3$ (LaTiMn), $LaCrO_3$ (LaCr) and Nb-doped $LaCrO_3$ (LaNbCr), and Other Perovskites as prospective coating materials:

Subtask 1.1: Identification of Non-Perovskite and Other Perovskite Materials as Coatings:
Subtask 1.2: Synthesis of Perovskite Powders and Fabrication of Sintered Parts:
Subtask 1.3: Physical and Electrical Characterization of Sintered Ta and Nb-doped TiO_2, other materials, LaMn, LaTiMn, LaCr, and LaNbCr:
Subtask 1.4: Collaborations with Other SECA Researchers:

Task 2.0 – Deposition of Ta-doped and Nb-doped TiO_2, other possible materials, LaTiMn and LaNbCr on metallic interconnect foils, oxidation studies, and ex-situ and in-situ (in stacks) characterization of coated interconnect:

Subtask 2.1: Deposition of doped TiO_2, other possible materials, LaMn, LaTiMn, LaCr, and LaNbCr coatings on alloy foils by sputtering
Subtask 2.2: Oxidation studies in air, fuel and dual atmospheres:
Subtask 2.3: Characterization of coated samples before and after oxidation:
Subtask 2.4: Development of a Coupon Testing Methodology in Conjunction with Other SECA Researchers:
Subtask 2.5: The Measurement of ASR of Coated and Oxidized Coupons:
Subtask 2.6: Validation of the Coupon Testing Methodology Developed by Testing a Short SOFC Stack:

Status of Task Completion:

Task 1.0 – Identification of Suitable Non-Perovskite Oxide Materials and Fabrication and characterization of Non-Perovskite Materials, $LaMnO_3$ (LaMn), Ti-doped $LaMnO_3$ (LaTiMn), $LaCrO_3$ (LaCr) and Nb-doped $LaCrO_3$ (LaNbCr), and Other Perovskites as prospective coating materials:

Subtask 1.1: Identification of Non-Perovskite and Other Perovskite Materials as Coatings: Completed.
Subtask 1.2: Synthesis of Perovskite Powders and Fabrication of Sintered Parts: Completed.
Subtask 1.3: Physical and Electrical Characterization of Sintered Ta and Nb-doped TiO_2, other materials, LaMn, LaTiMn, LaCr, and LaNbCr: Completed.
Subtask 1.4: Collaborations with Other SECA Researchers: Discussions conducted underway with GE in Torrance, CA. No samples were supplied.

Task 2.0 – Deposition of Ta-doped and Nb-doped TiO_2, other possible materials, LaTiMn and LaNbCr on metallic interconnect foils, oxidation studies, and ex-situ and in-situ (in stacks) characterization of coated interconnect:

Subtask 2.1: Deposition of doped TiO_2, other possible materials, LaMn, LaTiMn, LaCr, and LaNbCr coatings on alloy foils by sputtering: Completed.
Subtask 2.2: Oxidation studies in air, fuel and dual atmospheres: Completed. Only limited work was done on dual atmospheres. Thus, no definitive trends could be detected.
Subtask 2.3: Characterization of coated samples before and after oxidation: Completed.
Subtask 2.4: Development of a Coupon Testing Methodology in Conjunction with Other SECA Researchers: Completed. A coupon testing procedure was developed. Discussions were held with other SECA researchers.
Subtask 2.5: The Measurement of ASR of Coated and Oxidized Coupons: Completed.
Subtask 2.6: Validation of the Coupon Testing Methodology Developed by Testing a Short SOFC Stack: Completed. Since fabrication of cells and stacks was, limited work was conducted using facilities at a local company. Long term stack testing will be required to demonstrate the methodology. Out of stack tests are in complete accord with the defect chemistry concept proposed.

2. OXIDATION RESISTANT AND ELECTRICALLY CONDUCTIVE PEROVSKITE COATINGS THROUGH DEFECT CHEMISTRY FOR CATHODE SIDE

2.1 Introduction

Solid oxide fuel cells (SOFCs) are solid-state energy conversion devices that produce electricity by electrochemically reacting fuel and oxidant gases across a solid electrolyte. One of the most critical components in planar solid oxide fuel cell (SOFC) stacks is interconnect, which is used to connect individual cells in series. Interconnect serves a dual purpose of electrically connecting cathode of one cell to the anode of the adjacent cell, as well as keeping the anodic and the cathodic gases separate. The basic requirements of a prospective interconnect material are explained in previous chapter.

As the operating temperature of SOFC is typically about 800°C it is a difficult task to find an appropriate interconnect material which will satisfy all of the above stringent requirements. Doped $LaCrO_3$ [1-4] has been widely explored as a ceramic interconnect material for high temperature SOFCs, operating between 800 and 1000°C. Its brittleness, high cost, and difficulty in manufacturing complex shapes have been the principal shortcomings of this material for application in planar SOFC. However, it is used in the Siemens tubular SOFC in which it is a relatively thin strip deposited directly on the tube.

The development of intermediate temperature SOFC (operating at 800°C, and below) has made it possible to use metallic interconnect materials. Unlike doped $LaCrO_3$ ceramics, metals are inexpensive and easy to fabricate into complex shapes. However, rapid oxidation kinetics, easy spalling tendency of the oxide scale and the formation of chromia as an oxide (which has a high electrical resistivity and a high volatility as hexavalent Cr [5-7]) restrict the use of many of the commercially available iron-based and nickel-based alloys as SOFC interconnect to short term applications. Currently, Fe-Cr alloys are being explored for application as SOFC interconnect [8-12]. The Fe-Cr alloys, typically ferritic stainless steels, are generally better matched in thermal expansion coefficient (around $11\text{-}13 \times 10^{-6}\ K^{-1}$) with that of other cell components than Ni-Cr alloys, and are relatively inexpensive. These alloys form Fe-Cr containing spinel oxide scales which exhibit good electrical conductivity. The main impediments to using these alloys as interconnect are rapid oxidation kinetics and spalling tendency of the oxide scale.

The other category of alloys that is used as interconnect material is the group of Ni-Cr super-alloys [13-19]. The Ni-Cr alloys generally have higher thermal expansion coefficient (around $15 \times 10^{-6}\ K^{-1}$) that is not well matched with the other cell components. This can in part be mitigated by using thin flexible alloy foils. The oxide scale formed typically contains Cr_2O_3, which is prone to volatilization and degrades cell performance [20,21]. Also, Cr_2O_3 exhibits higher electrical resistivity than Fe-Cr spinel oxides. However, the above shortcomings are outweighed by two important advantages; good adherence of the Cr_2O_3 oxide scale on the base alloy, and sluggish oxidation kinetics compared to Fe-Cr alloys.

One of the approaches for reducing the oxidation kinetics is the deposition of ceramic protective coatings on alloy foils or plates. Larring and Norby studied a number of perovskites and spinels, including Mn-Co-spinel as prospective coating materials [22]. Kim et al. studied the effect of dip coated $(La_{0.85}Sr_{0.15})_{0.9}MnO_3$ (LSM) perovskite on the electrical properties of an Fe-16Cr alloy [23]. Armstrong et al. examined the kinetics of oxidation of Haynes 230 with Mn-Cr spinel as well as LSM coatings [24]. They observed that the LSM coating was three times more effective in suppressing oxidation kinetics than the spinel coating [24]. Yang et al. studied the effectiveness of a $Mn_{1.5}Co_{1.5}O_4$ spinel coating on Crofer22 APU in mitigating Cr migration and minimizing interfacial resistance [25, 26]. Similarly, Chen et al. evaluated the effects of $MnCo_2O_4$ spinel coating on SS430 and concluded that such a coating significantly reduced Cr_2O_3 scale formation and increased the electronic conductivity of the scale [27]. With the exception of the work by Armstrong et al. [24], in much of the reported literature, the criterion used for selecting a coating material has usually been high electronic conductivity and in some cases possibly low Cr diffusivity. Also, with the exception of work by Armstrong et al. [24], in the majority of the studies, the coating was typically 10 to 25 microns in thickness. Too thick a coating suffers from increased tendency for delamination or spalling. Preliminary calculations show that for long term stability, the total thickness of coating + oxide scale should be typically less than 10 microns for many base alloys and coating materials of interest, and preferably ≤ 5 μm.

It has been observed in all reported studies that oxide scale forms under the coating, implying transport of oxygen through the coating as an essential step in the oxidation of coated alloys and thus oxygen diffusivity through the coating as an important parameter. The importance of the need for low oxygen ion diffusivity through the coating has been appreciated but this does not seem to have been addressed in the selection of the coating material.

The focus of the present work was on identifying coating materials for cathodic side (oxidizing atmosphere) of SOFC with as low oxygen ion conductivity as possible to minimize the transport of oxygen to the metal surface, and at the same time having an acceptable electronic conductivity. Work by Armstrong et al. showed that LSM was more effective in suppressing oxidation kinetics than spinel [24]. For this reason, $LaMnO_3$-based perovskite was selected as the baseline material. In order to suppress oxygen ion transport, $LaMnO_3$ was doped with Ti on the Mn site. A perovskite was selected over a spinel since cation transport is generally known to be more sluggish in perovskites [28]. $LaMnO_3$ was selected since its electronic conductivity is high, oxygen transport is known to be sluggish, and it is used as one of the components in SOFC.

$LaMn_{0.9}Ti_{0.1}O_{3+\delta}$ (LTM), i.e. $LaMnO_3$ doped with Ti (higher valent dopant) was synthesized by a conventional solid-state route. In order to determine the role of doping in the suppression of oxygen vacancy concentration, samples of undoped $LaMnO_3$ (LM) and samples doped with Sr of composition $La_{0.95}Sr_{0.05}MnO_{3-\delta}$ (LSM) were also synthesized. Oxidation kinetics of Haynes 230 (H230) (composition given in table 2.I) foils coated with LM, LSM, and LTM were investigated and results were interpreted in terms of defect chemistry and electrical conductivity measurements on the oxide coating materials. The oxidation kinetics results were compared with a theoretical model. Area specific resistance (ASR) of the oxidized samples was measured.

Table2.1: Composition (mole%) of H230 alloy

Elements	Ni	Cr	Fe	Mo	Mn	Co	W
Mole %	56	26	3.4	1.3	0.74	5.3	4.8

2.2 Theoretical

2.2.1: Kinetics of Oxidation: A dense protective coating of a ceramic perovskite material, with low oxygen ion conductivity and good electronic conductivity, was deposited on H230 alloy foils. Chromia, Cr_2O_3, is the predominant constituent in the oxide scale formed during the oxidation of the baseline alloy. In samples with a protective coating, some oxidation of the baseline alloy is expected, with scale formed between the coating and the alloy. Fig. 2.1 shows a schematic diagram of a coated metal foil after an oxidative treatment.

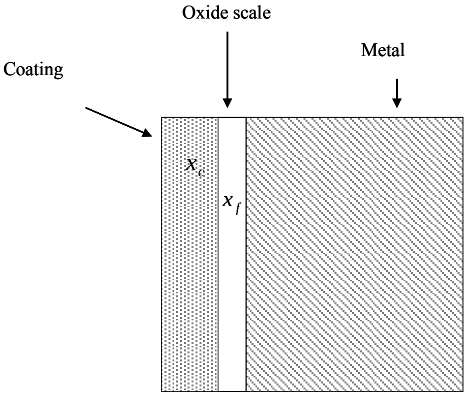

Fig. 2.1: A schematic diagram of a ceramic coated foil oxidized in air.

The kinetics of oxidation of a coated alloy foil can be described by an equation of the following type [29]:

$$k_c x_f^2 + 2k_f x_c x_f = k_f k_c t \tag{2.1}$$

where x_f and x_c are the thicknesses of the oxide scale and the protective coating respectively, and k_f and k_c are respectively the parabolic rate constant parameter for oxidation of the pristine alloy and the kinetic parameter describing oxygen permeation through the coating. The k_f is given by [29]

$$k_f = \frac{EV_M}{2F}\left(\frac{\sigma_i^f \sigma_e^f}{\sigma_i^f + \sigma_e^f}\right) \tag{2.2}$$

where σ_i^f and σ_e^f are respectively ionic and electronic conductivities of the oxide scale, V_M is the molar volume of the oxide scale, E is the Nernst voltage corresponding to the oxide scale formation (which is related to the free energy of formation of the oxide), and F is the Faraday constant; while k_c is given by [29]

$$k_c = \frac{EV_M}{2F}\left(\frac{\sigma_i^c \sigma_e^c}{\sigma_i^c + \sigma_e^c}\right) \approx \frac{EV_M}{2F}\sigma_i^c \tag{2.3}$$

where σ_i^c and σ_e^c are respectively ionic and electronic conductivities of the coating material. The latter simplification assumes $\sigma_i^c << \sigma_e^c$, which is quite accurate for the type of material selected for coating in this work. Solution to equation (2.1) is given by

$$x_f = \frac{\sqrt{\left(k_f^2 x_c^2 + k_f k_c^2 t\right)} - k_f x_c}{k_c} \tag{2.4}$$

There are two limiting cases of the above equation, namely

1) $k_f x_c^2 << k_c^2 t$

2) $k_f x_c^2 >> k_c^2 t$

For the first limiting case, we obtain,

$$x_f = \sqrt{k_f t} \tag{2.5}$$

In this case, the coating is ineffective in suppressing oxidation kinetics of the alloy. Oxygen permeation through the coating is fast and oxidation kinetics is dictated only by k_f. This is essentially equivalent to the situation when metal foil is uncoated.

For the second limiting case, we obtain,

$$x_f = \frac{k_c}{2x_c} t \tag{2.6}$$

Alternatively, the derivative of equation (2.4) evaluated at $t \to 0$ is given by

$$\left.\frac{dx_f}{dt}\right|_{t\to 0} = \left.\frac{k_f k_c}{2\sqrt{k_f^2 x_c^2 + k_f k_c^2 t}}\right|_{t\to 0} = \frac{k_c}{2x_c} \tag{2.7}$$

That is, the initial slope of the plot of x_f vs. t is related only to k_c and x_c; that is, parameters of the coating. In this case, the kinetics of oxide growth with time is linear and limited only by oxygen permeation through the coating. Such a coating is effective in suppressing oxidation kinetics of the alloy and this is the desired situation. Thus, by suitably choosing x_c and k_c, desired suppression of oxidation kinetics is possible.

The main objective of this study was to tailor the coating materials to obtain as low a value of k_c as possible. Fig. 2.2 shows plots of theoretically calculated oxide scale thickness formed underneath the coating (from Eqn. (2.4)) vs. time. For these calculations k_f was assumed to be 10^{-12} cm^2/s at 800^{o}C, which corresponds to an alloy prone to rapid oxidation. The coating thickness is assumed to be 5 µm. The value of k_c was varied between 1 x 10^{-15} to 1 x 10^{-11} cm^2/s. It is observed that for values of k_c ranging between 1 x 10^{-15} and 1 x 10^{-14} cm^2/s the oxidation kinetics is nearly linear over the duration, while for values of k_c ranging between 1 x 10^{-13} to 1 x 10^{-11} cm^2/s, it is nearly parabolic over the same duration. For a k_c of 1 x 10^{-15} cm^2/s, and with a coating of 5 µm thickness, after 40,000 hours the thickness of the oxide scale formed, x_f, is only 1.4 µm. Thus, a 5 µm coating with k_c of 1 x 10^{-15} cm^2/s is expected to be quite satisfactory for SOFC applications, even if an alloy prone to rapid oxidation is used as interconnect. The main objective of this work was to prepare coating materials that exhibit k_c values less than 1 x 10^{-14} cm^2/s, and preferably as low as 1 x 10^{-15} cm^2/s.

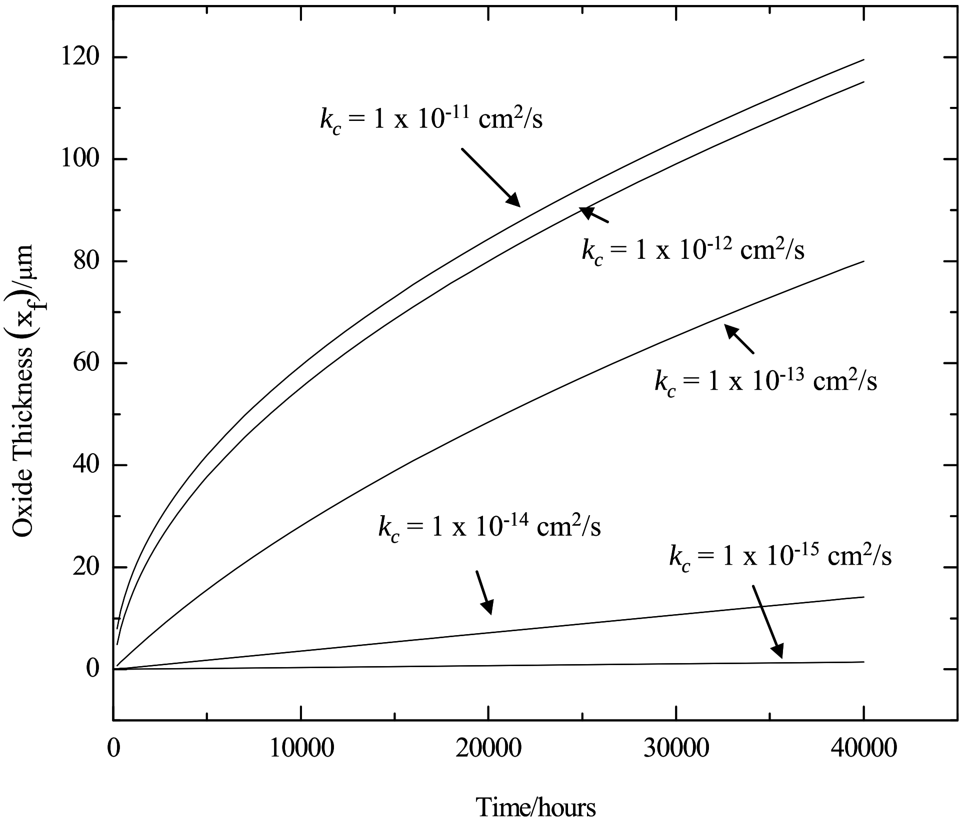

Fig. 2.2: Theoretically calculated oxide scale thickness, x_f, vs. time of oxidation, t, at 800°C for different values of k_c at a fixed value of the parabolic rate constant for the base alloy assumed as $k_f = 1 \times 10^{-12}$ cm^2/s. This value of k_f represents rather aggressive oxidation kinetics of the base alloy. The figure shows that a coating of 5 micron thickness with $k_c = 1 \times 10^{-15}$ cm^2/s can drastically suppress oxidation kinetics of an alloy prone to otherwise rapid oxidation.

2.2.2 Ionic Conductivity and Defect Chemistry:

As shown by equations (2.2) and (2.3), kinetic parameters depend upon ionic and electronic conductivities, which in turn depend upon defect chemistry. General equation for ionic conductivity is given by

$$\sigma_i = z_i e \mu_i n_i = \frac{z_i^2 e^2 D_i n_i}{k_B T} \tag{2.8}$$

where z_i is the valence, μ_i is the mobility, D_i is the diffusivity, n_i is the concentration, e is the electronic charge, k_B is the Boltzmann constant, and T is the temperature. For the present interest in oxygen ion conductivity of the coating, the above becomes

$$\sigma_i = \frac{4e^2}{k_B T} D_{O^{2-}} n_{O^{2-}} = \frac{4e^2}{k_B T} D_{V_O^{\bullet\bullet}} n_{V_O^{\bullet\bullet}} \tag{2.9}$$

where $D_{V_O^{\bullet\bullet}}$ is the oxygen vacancy diffusivity and $n_{V_O^{\bullet\bullet}}$ is the oxygen vacancy concentration (#/cm^3). It is assumed that transport occurs predominantly by a vacancy mechanism. In terms of fractional vacancy concentration $\left[V_O^{\bullet\bullet}\right]$, the oxygen vacancy concentration is given by $n_{V_O^{\bullet\bullet}} = n_{O^{2-}}^{o}\left[V_O^{\bullet\bullet}\right]$, where $n_{O^{2-}}^{o}$ denotes the number of oxygen sites per unit volume, which is nearly the same as $n_{O^{2-}}$, the latter representing the number of oxygen ions per unit volume. Usually, $D_{V_O^{\bullet\bullet}}$ in a given material at a given temperature is assumed to be constant. Thus, the ionic conductivity is mainly influenced by the oxygen vacancy concentration, which in turn can be varied by doping with aliovalent ions, and/or by changing oxygen partial pressure. In the present work, $LaMnO_3$ was doped with Sr (lower valent ion) on the La site to form $La_{0.95}Sr_{0.05}MnO_{3-\delta}$ (LSM) or Ti on the Mn site to form $LaMn_{0.9}Ti_{0.1}O_{3+\delta}$ (LTM). The expectation is that Sr doping will increase oxygen vacancy concentration with respect to $LaMnO_3$ and Ti doping will suppress oxygen vacancy concentration with respect to $LaMnO_3$. Thus, oxygen ion conductivity of LSM should be higher than that of LM, and oxygen ion conductivity of LTM should be lower than that of LM. This means LTM should be a better coating material than LSM. Since LSM has already been shown to be superior to Mn-Cr spinel, it is the expectation that LTM as a coating should be far superior to Mn-Cr spinel.

2.2.3: Defect Chemistry of LSM and LTM:

$LaMnO_3$ is presumed to exhibit Schottky defects. Within the law of mass action formalism, the fractional defect concentrations are related to each other by

$$\left[V_{La}'''\right]\left[V_{Mn}'''\right]\left[V_O^{\bullet\bullet}\right]^3 = K_s \tag{2.10}$$

where $\left\lfloor V_{La}^{'''} \right\rfloor$, $\left\lfloor V_{Mn}^{'''} \right\rfloor$, and $\left\lfloor V_{O}^{\bullet\bullet} \right\rfloor$ are respectively fractional vacancy concentrations on A-sublattice (La), B-sublattice (Mn), and O-sublattice, and all vacancies are assumed charged (Kroger-Vink notation used). When Sr is doped on A-site, it is incorporated in $LaMnO_3$ by the creation of oxygen vacancies, by a formula of the type $La_{(1-x)}Sr_xMnO_{(3-x/2)}$, which corresponds to x/2 as the oxygen vacancy concentration, assuming charge compensation by point defects only. However, Mn can exist in +3 and +4 states. In an oxidizing atmosphere, the oxygen vacancies created by Sr doping are in part annihilated by filling them up by oxygen from the ambient via a reaction of the type

$$\frac{1}{2}O_2 + V_O^{\bullet\bullet} \rightarrow O_O^{\times} + 2h^{\bullet} \tag{2.11}$$

leading to a general formula $La_{(1-x)}Sr_xMnO_{(3-x/2+\varepsilon)}$, with $\varepsilon < x/2$. Thermogravimetric measurements have been reported with oxygen stoichiometry in excess of '3, i.e. $3+\lambda$ [30]. This, however, occurs with simultaneous vacancy formation on the cation sublattices, and suppressing oxygen vacancy concentration, since the formation of oxygen interstitials is known to be energetically unfavorable in the perovskite structure. Thus, one may represent LSM as $La_{(1-x)}Sr_xMnO_{(3-x/2+\varepsilon)}$ or $La_{(1-x')}Sr_{x'}MnO_{(3+\lambda)}$. This is a matter of choice. In what follows, the defect chemistry will be described in terms of maximum oxygen stoichiometry restricted to 3 (that is normalized to '3') with vacancy creation on cation sublattices. The Sr-doping thus enhances electron (hole) conductivity and to some extent also increases the oxygen ion conductivity. Therefore, LSM is not the preferred coating material, although it is still superior to Mn-Cr spinel [24].

It is required that the coating material exhibit as low an oxygen vacancy concentration as possible without significantly compromising electronic conductivity. The suppression of oxygen ion vacancy concentration is possible by doping on the cation site by a higher valent ion as described in what follows:

Titanium incorporation on the B-site of $LaMnO_3$, represented by a formula of the type $LaMn_{(1-x)}Ti_xO_{(3+x/2)}$, should lead to the creation of cation vacancies by a reaction of the type

$$Ti^{\times} \rightarrow Ti_{Mn}^{\bullet} + \frac{1}{6}V_{La}^{'''} + \frac{1}{6}V_{Mn}^{'''} \tag{2.12}$$

where the main compensating defects are assumed to be vacancies on the cation sublattices. This is equivalent to adding x amount of "$LaTiO_{3.5}$" to (1-x) amount of $LaMnO_3$, or site-specific doping [31,32]. The electroneutrality condition can be given as (assuming the presence of some oxygen vacancies)

$$3\left\lfloor V_{La}^{'''} \right\rfloor + 3\left\lfloor V_{Mn}^{'''} \right\rfloor + n = 2\left\lfloor V_O^{\bullet\bullet} \right\rfloor + \left\lfloor Ti_{Mn}^{\bullet} \right\rfloor + p \tag{2.13}$$

where n and p are electron and hole concentrations respectively, with all concentrations given on a per unit cell basis. In the above case predominant defects are point defects. Thus, equation (2.13) can be written as

$$3\left[V_{La}^{'''}\right]+3\left[V_{Mn}^{'''}\right]=2\left[V_{O}^{\bullet\bullet}\right]+\left[Ti_{Mn}^{\bullet}\right] \tag{2.14}$$

At sufficiently high concentrations of Ti, it may be further assumed that $\left[V_{O}^{\bullet\bullet}\right]<<\left[V_{La}^{'''}\right],\left[V_{Mn}^{'''}\right]$. Then equation (2.14) becomes

$$3\left[V_{La}^{'''}\right]+3\left[V_{Mn}^{'''}\right]=\left[Ti_{Mn}^{\bullet}\right] \tag{2.15}$$

Assuming further that vacancy concentrations on the La and Mn sites are approximately equal, one can write

$$\left[V_{La}^{'''}\right]=\left[V_{Mn}^{'''}\right]=\frac{x}{6} \tag{2.16}$$

It is important to note that this assumption is not necessary for the defect chemistry based approach given here. This assumption is made for simplicity. Even without this assumption, the general conclusions remain the same – only the details are altered. Using the Schottky product for $LaMnO_3$, the oxygen vacancy concentration is given by

$$\left[V_{O}^{\bullet\bullet}\right]=\frac{6^{2/3}K_{s}^{1/3}}{x^{2/3}} \tag{2.17}$$

It is understood that equation (2.17) is applicable only in Ti-doped LM above some threshold concentration, x_o, and is not applicable in the limit $x \to 0$. For $x < x_o$, the oxygen vacancy concentration will be given by the intrinsic value, that corresponding to 'pure' LM, given by $\left[V_{O}^{\bullet\bullet}\right]_o = 9^{1/5}K_{s}^{1/5}$. The intrinsic ionization reaction is given by

$$0 \to e' + h^{\bullet} \tag{2.18}$$

and the corresponding law of mass action constant is given by

$$K_i = np \qquad (2.19)$$

The oxygen incorporation reaction is given by equation (2.11). The corresponding law of mass action constant is given by

$$K_p = \frac{p^2}{\left[V_O^{\bullet\bullet}\right] p_{O_2}^{1/2}} \qquad (2.20)$$

Solving the above equations gives,

$$p = 6^{1/3} K_s^{1/6} K_p^{1/2} x^{-1/3} p_{O_2}^{1/4} \qquad (2.21)$$

Again it is understood that the above equation is applicable to Ti-doped materials above some threshold concentration, x_o, and is not applicable in the limit $x \to 0$. For $x < x_o$, the hole concentration will be that corresponding to ‘intrinsic’ behavior. Similarly, for Ti-doped material, electron concentration is given by

$$n = 6^{-1/3} K_s^{-1/6} K_p^{-1/2} K_i x^{1/3} p_{O_2}^{-1/4} \qquad (2.22)$$

Now the electronic conductivity in S/cm is given by

$$\sigma_e = Ne(\mu_e n + \mu_h p) \qquad (2.23)$$

where, μ_e and μ_h are respectively electron and hole mobilities in cm^2/volt.sec, and N denotes the number of unit cells per unit volume. Substituting equations (2.21) and (2.22) into equation (2.23) gives

$$\sigma_e = \sigma_e^c = Ax^{1/3} p_{O_2}^{-1/4} + Bx^{-1/3} p_{O_2}^{1/4} \qquad (2.24)$$

where A and B represent factors independent of x and p_{O_2}, and σ_e^c denotes electronic conductivity of the coating. Equation (2.24) shows that when doped with Ti, the electron conductivity increases but electron hole conductivity decreases. LM is known to be predominantly a p-type conductor over a wide range of oxygen partial pressures. Thus, the above may be approximated by

$$\sigma_e^c \approx Bx^{-1/3} p_{O_2}^{1/4} \tag{2.25}$$

and it is expected that electronic conductivity should decrease with increasing Ti doping. The net ionic conductivity is given by equation (2.9). Substituting for the oxygen vacancy concentration in terms of Ti concentration gives

$$\sigma_i = \frac{4e^2 6^{2/3} K_s^{1/3}}{k_B T} N D_{V_O^{\bullet\bullet}} x^{-2/3} \tag{2.26}$$

or

$$\sigma_i = \sigma_i^c = \sigma_o x^{-2/3} \tag{2.27}$$

where σ_o is independent of Ti concentration and σ_i^c refers to ionic (oxygen) conductivity of the coating. Equations (2.25) and (2.27) demonstrate that the oxygen ion conductivity and the electronic conductivity of the coating should decrease with increasing Ti doping. It is expected that in general $\sigma_e^c >> \sigma_i^c$. Thus, with Ti doping k_c should decrease thereby suppressing interconnect oxidation kinetics. The decrease of σ_e^c, however, implies that the area specific resistance (ASR) due to the coating will increase. It is to be noted however that as long as the suppression of electronic conductivity is not large, the contribution of the coating to the total ASR will likely be negligible. Also, as the electronic conductivity of chromia scales is much lower, it is the expectation that the net ASR of interconnect with Ti-doped LM coating (LTM) will be lower than interconnect with LM or LSM coating due to slower oxidation when coated with LTM, and much lower than uncoated interconnect.

The measurement of very low oxygen ion conductivity is rather difficult and requires Hebb-Wagner type blocking electrode technique. However, the measurement of total conductivity of the coating material, which is predominantly electronic, provides an independent verification of the defect chemistry based approach. Further, if suppression of oxidation kinetics can be achieved on coated samples with LTM exhibiting superior performance to LSM, it will validate the defect chemistry based approach for the suppression of oxidation kinetics (by suppressing oxygen ion conduction through the coating). The following experimental procedure was used to test the hypothesis concerning the role of defect chemistry of the coating in suppression of oxidation kinetics of the alloy.

2.3 Experimental

2.3.1 Synthesis, Characterization, and Sputtering of Ceramic Coating Materials:

Ceramic coating materials were synthesized by a conventional solid state route using La_2O_3 (Alfa, 99.99% pure), MnO_2 (Alfa, 99.99% pure), SrO (Alfa, 99.99% pure) or TiO_2 (Alfa, 99.99% pure) in appropriate amounts. All of the above reactant powder mixtures were ball-milled using zirconia media (0.25" dia) for 24 hours followed by calcination at 1100°C for 2 hours. The phase purity of compounds formed after calcination was confirmed by X-ray diffraction (Phillips X'pert). The calcined powder was pressed to form small bars of dimensions 45 mm x 10 mm x 3 mm using a uniaxial hydraulic press. The bars were sintered at 1400°C for 2 hours. Density of the bars was determined by the standard fluid immersion method. Sputtering targets of dimensions 7.5 cm in diameter and 3 mm in thickness of all three ceramic materials were fabricated by die-pressing powders into discs followed by sintering at 1400°C for 2 hours. After sintering, these discs were attached to copper backing plates using a silver epoxy. Backing plate was necessary to prevent unwanted cracking of target discs, which can occur due to heat generated during the process of sputtering.

Electrical characterization was carried out using a D.C. four probe conductivity technique**.** Four contact electrodes were made on the ceramic bars using silver paste followed by curing at 600°C for 1 hour. Silver wires (Alfa, 0.25 mm diameter) were wrapped around the silver contacts to form four silver leads. The distances between the inner (voltage) leads and the outer (current) leads were approximately 30 mm and 40 mm, respectively. The sample was heated to 500°C in a tube furnace and was stabilized for one hour. A constant current of 0.04 amperes was passed through the outer electrical probes using a Keithly 6220 constant current source, and voltage was measured across the inner electrical probes using a Keithly 2000 multimeter. Conductivity was measured in the temperature range from 500°C to 800°C by increasing the temperature in steps of 50 degrees. Total conductivity of the sample at a given temperature was calculated using the following formula:

$$\sigma_{total} = \frac{I}{V} \times \frac{L}{A} \tag{2.28}$$

where I is the current, V is the voltage drop measured across the inner probes, L is the distance between the inner probes (30 mm) and A is the cross sectional area of the bar sample (30 mm^2). Total conductivity was plotted as a function of temperature for different ceramic materials.

Alloy foils of H230 (12 mm x 12 mm) were thoroughly cleaned with acetone and water. A Denton-18 RF Sputtering system was used to deposit 1 μm thick ceramic coatings on both sides of the alloy foils. The target materials used were $La_{0.95}Sr_{0.05}MnO_{3-\delta}$ (LSM), $LaMnO_3$ (LM), and $LaMn_{0.9}Ti_{0.1}O_{3+\delta}$ (LTM). The chamber was evacuated to 2 x 10^{-6} atmospheres. Sufficiently low chamber pressure was necessary to ensure the deposition of dense and adherent coatings on the foils. RF power of 150 watts was applied to obtain a sputtering rate of ~16 nm/min. X-ray diffraction analysis was carried out on coated foils to examine the crystal structure of the coatings.

2.3.2 Oxidation Kinetics Studies and Characterization of Oxidized Samples:

H230 foils coated separately with $La_{0.95}Sr_{0.05}MnO_{3-\delta}$ (LSM), $LaMnO_3$ (LM), and La $Mn_{0.9}Ti_{0.1}O_{3+\delta}$ (LTM), were oxidized in a tube furnace at 800°C in air (p_{O_2} = 0.21 atm) for 168, 336, 504 and 1080 hours. Pristine metal foils were also oxidized along with coated ones to compare the oxidation behavior of metallic interconnects with and without protective coatings.

Small pieces were cut from the oxidized foils, mounted edgewise in an epoxy mold, polished to a mirror finish and examined under a scanning electron microscope (SEM, Hitachi S-3000N) in back scattered (BSE) mode. The oxide scale thickness was measured at several locations and the mean value was calculated. This process was adopted due to the non-uniformity in oxide scale thickness along the length of the sample. The principal reason for the non-uniformity in the oxide scale thickness is the non-uniformity in the as received base alloy, in which microstructural non-uniformities are well in excess of several microns – much greater than either the coating thickness or the oxide scale thickness. Simultaneously, elemental composition across metal/oxide and oxide/coating interfaces was measured using energy dispersive X-ray (EDAX) technique. Also the surfaces of the oxidized samples were examined under the SEM to determine possible morphological changes that occur during oxidation.

Square of the oxide scale thickness, x_f^2, was plotted vs. time for the uncoated foil to determine k_f of H230 alloy. For the coated foils, the oxide scale thickness, x_f, was plotted vs. time. Using the k_f determined from the oxidation kinetics of the uncoated foil, a best fit to equation (2.4) was obtained for data on coated foils from which the k_c of the coating was determined. A phase analysis of the oxidized samples was conducted using X-ray diffraction technique (Phillips, X'pert diffractometer).

2.3.3 Measurement of Area Specific Resistance (ASR):

Schematic of the apparatus used to measure ASR is shown in Fig.2.3. Silver foils of 0.5 cm^2 area with attached silver wires were placed on either side of an oxidized sample and the other ends of the silver wires were connected to a Keithley 2000 multimeter. The oxidized sample, along with the silver foils on each side, was placed between two ceramic discs (for support) and pressed with the help of a spring loading assembly. Suitable pressure was applied by properly adjusting the springs. The assembly was inserted inside the furnace (with springs outside the furnace) and heated to 500°C. A constant current of 1 amp was passed through the sample and values of resistance across the sample were recorded at 50 degree intervals up to 800°C. Silver foils were used instead of platinum/silver paste to prevent possible penetration of paste into the protective coating through cracks or fissures, which can yield an artificially low resistance. The recorded value of resistance consisted of resistance of silver wires, silver foils, alloy foil, coating, and the oxide scale. The resistance of the assembly without the foil sample was also measured over the temperature range.

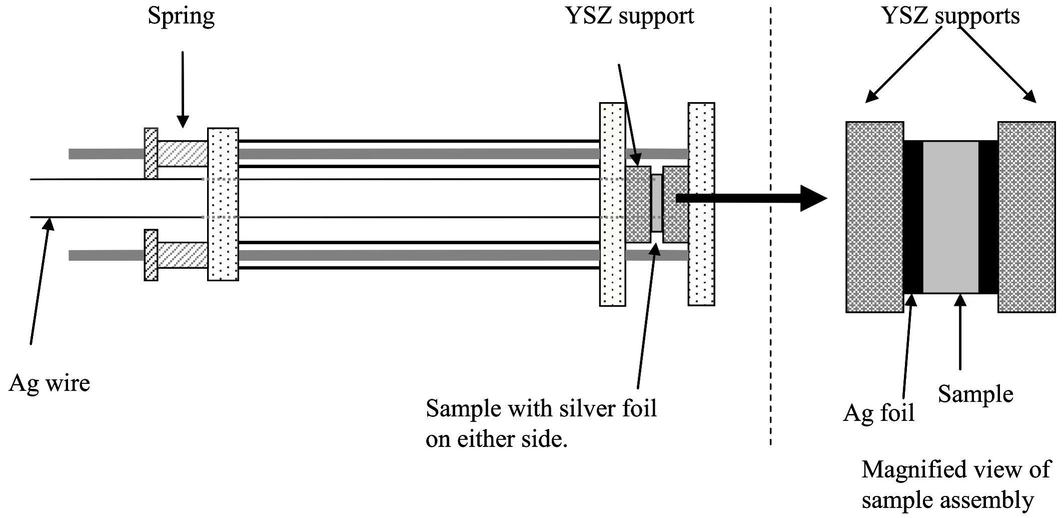

Fig. 2.3: A schematic diagram of the set up used to measure ASR.

This resistance, which is mainly due to the silver wires, was subtracted from the resistance measurement on the foil to obtain the resistance due to the oxide scale. The resistance of the protective coating is negligible (coating ASR ~5 x $10^{-6}\ \Omega\text{cm}^2$) and can be ignored, and so can the resistance of alloy foil since it too is negligible. This gave the resistance for oxide scales on both sides of sample. Thus, dividing this value by two and multiplying by the area of silver foil, area specific resistance (ASR) for the oxide scale was calculated at each measurement temperature, given by

$$(ASR)_{oxide} = \frac{(R_{With\_sample} - R_{Without\_sample}) \times Area}{2} \tag{2.29}$$

ASR measurements were conducted on uncoated and coated alloy foils oxidized for various periods of time up to a maximum of 1080 hours. The ASR of uncoated and coated H230 foils was plotted vs. temperature for various oxidation times.

2.4 Results and Discussion

2.4.1: Synthesis, Characterization, and Sputtering of Ceramic Coating Materials:

The XRD pattern of LM matched with that of JCPDS data file no. 35-1353. It has an othorhombic crystal structure with lattice parameters: a = 5.537 A^o, b = 5.741 A^o, c = 7.694 A^o. XRD patterns of LTM and LSM calcined powders showed the same orthorhombic perovskite structure as that of LM. No traces of free SrO or TiO_2 were observed in the respective XRD patterns (Fig.2.4). Thus, it appears that TiO_2 and SrO fully dissolved in LM. Ionic radii of La^{3+} and Sr^{2+} are 1.185 A^o and 1.27 A^o, respectively, while those of Mn^{3+} and Ti^{4+} are 0.785 A^o and 0.745 A^o, respectively [33]. Thus, in the case of LSM, it is expected that Sr substituted for La while in the case of LTM, Ti substituted for Mn.

Densities of the sintered samples were typically greater than 95% of theoretical. Fig. 2.5 shows plots of total electrical conductivity measured by four probe DC technique on ceramic coating materials as a function of temperature. $LaMnO_3$ (LM) is predominantly an electronic conductor and hence the total conductivity is essentially electronic (and the same is the case with LSM and LTM). The plots clearly show that the electronic conductivity (or total conductivity) of LTM is the lowest while that of LSM is the highest at all temperatures. Thus, doping LM by a higher valent (donor) ion decreased its electronic conductivity while doping it by a lower valent ion (acceptor) increased its electronic conductivity. These results are in accord with defect chemistry analysis given section 2.3. It is important to note that even the lowest value of electronic conductivity (48 S/cm at 800^{o}C) of LTM is quite high and is not expected to be a limiting factor in determining the interconnect ASR. Note that for a coating of 10 microns thickness, a practical upper limit, electronic conductivity of 1 S/cm leads to a contribution of only ~0.001 Ωcm^2 to the total ASR. That is, as long as the electronic conductivity of the coating material is high enough (above 1 S/cm), it has negligible influence on the net ASR, and is not a factor of relevance in the selection of the coating material. X-ray diffraction pattern of as-coated H230 foil with a 1 μm coating of LTM is shown in Fig.

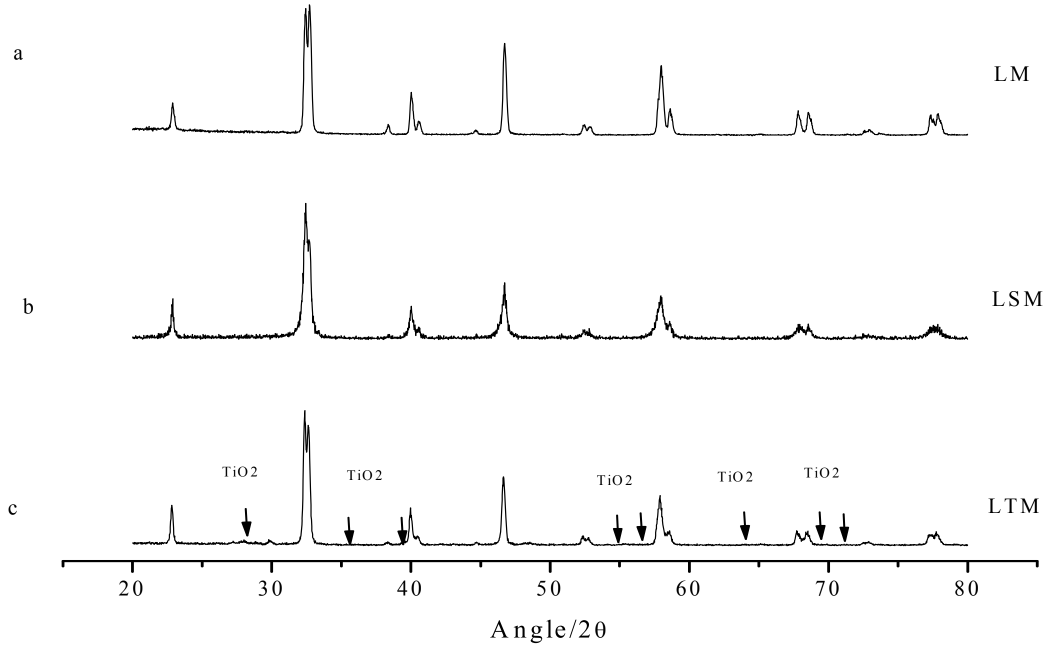

Fig.2.4: XRD patterns of LM, LSM, and LTM.

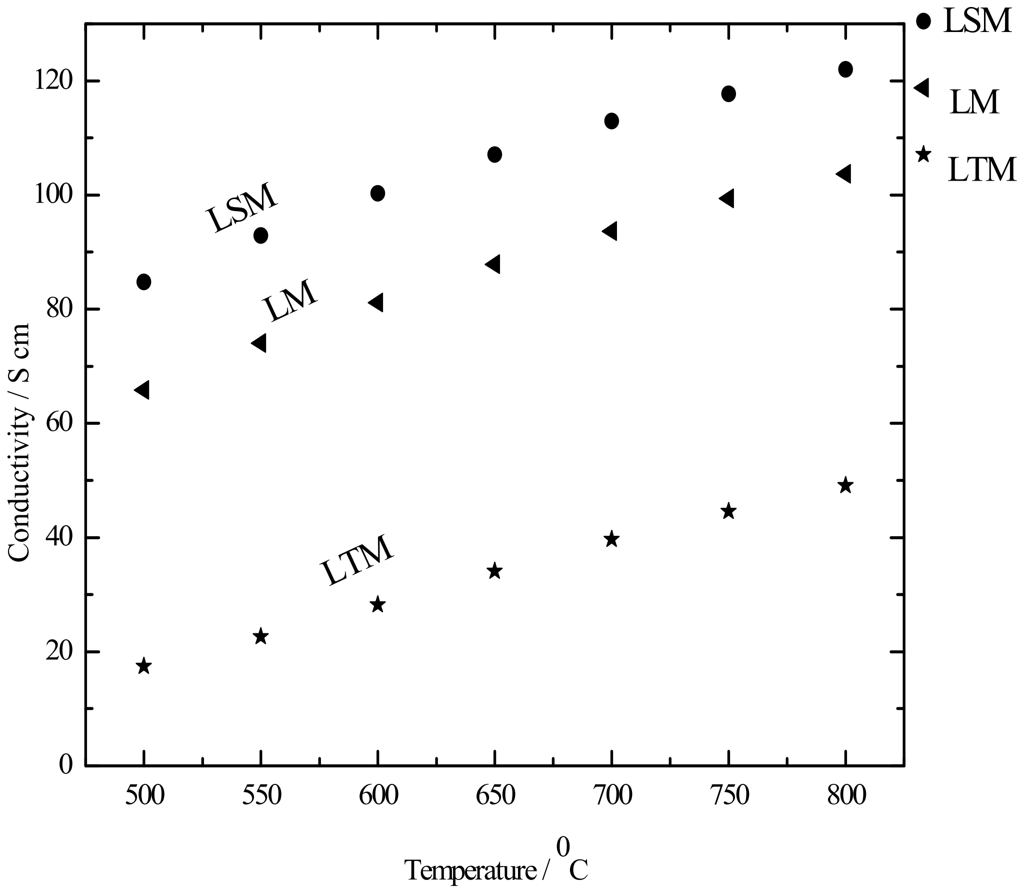

Fig. 2.5: Total conductivity vs. temperature for LM, LSM, and LTM.

2.6a. It is apparent from the XRD pattern that the as-deposited coating is amorphous. However, after annealing at 800°C for 5 hours, the XRD pattern showed the formation of a crystalline phase, which exactly corresponds to the XRD pattern of the target material (Fig. 2.6b). This suggests that the composition and the crystal structure of the coating are the same as that of the target material. Fig. 2.7 shows surface SEM micrographs of as-coated H230 foil with 1 μm LTM coating. SEM examination showed that the coating was adherent and dense. This suggests oxygen transport through the coating occurs by the transport of oxygen ions only (with coupled transport of electron holes), a necessary requirement for the coating to be effective in suppressing oxidation kinetics by the mechanism discussed herein, and not by gaseous diffusion of oxygen molecules through the pores.

2.4.2 Oxidation Studies and Characterization of Oxidized Samples: Fig. 2.8a and Fig. 2.8b show XRD patterns of uncoated H230 alloy foil and H230 alloy foil with 1 μm thick LTM coating, oxidized in air at 800°C for 1080 hours. Cr_2O_3 and $Mn_{1.5}Cr_{1.5}O_4$ are the oxide scale products, Cr_2O_3 being the predominant oxide phase in the scale.

Fig. 2.9 shows SEM micrographs of the surfaces of uncoated H230 foil and of H230 foil with a 1 µm coating of LTM, oxidized in air at 800^{o}C for 168 hours. Significant differences were observed between the uncoated and the coated foils. The uncoated foil was completely covered with a grainy oxide layer but the coated foil appeared relatively unchanged. Fig. 2.10 shows edgewise SEM micrographs of an uncoated H230 foil and H230 foils with 1 µm coatings of LSM and LTM, oxidized in air at 800^{o}C. for 1080 hours. It is clear from the micrographs that the oxide scale forms underneath the coating. Fig. 2.11 shows EDAX analysis on H230 foil with 1 µm LTM

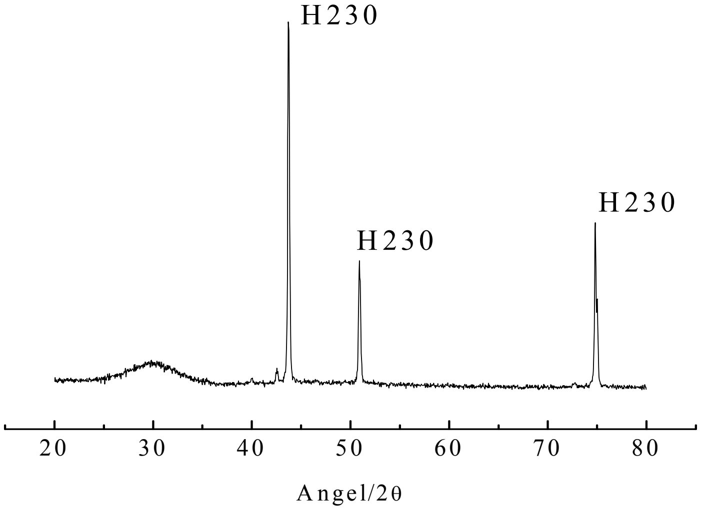

Fig. 2.6a: An XRD pattern of as-coated H230 alloy foil (1 µm LTM coating).

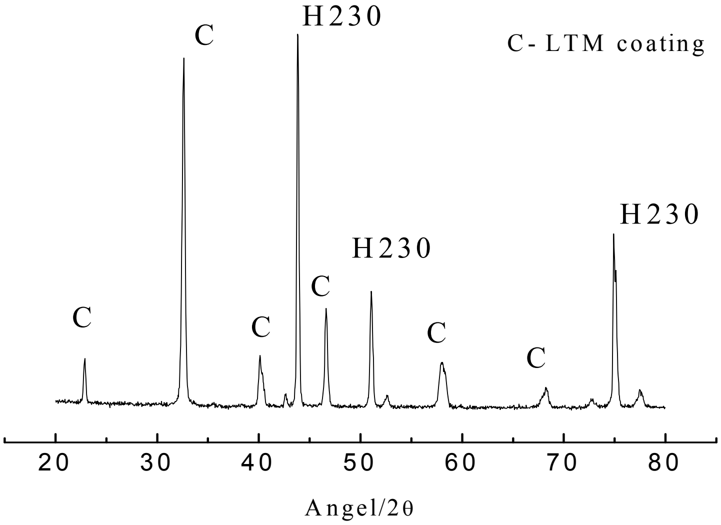

Fig. 2.6b: An XRD pattern of coated H230 alloy foil (1 µm LTM coating), annealed at 800^o for 5 hours.

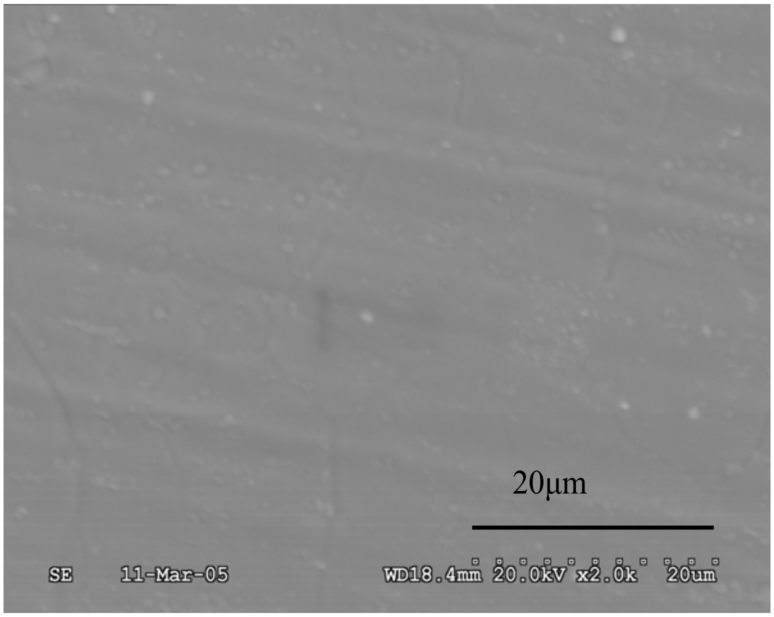

Fig.2.7: SEM micrograph of the surface of as coated H230 foil (1 μm LTM coating).

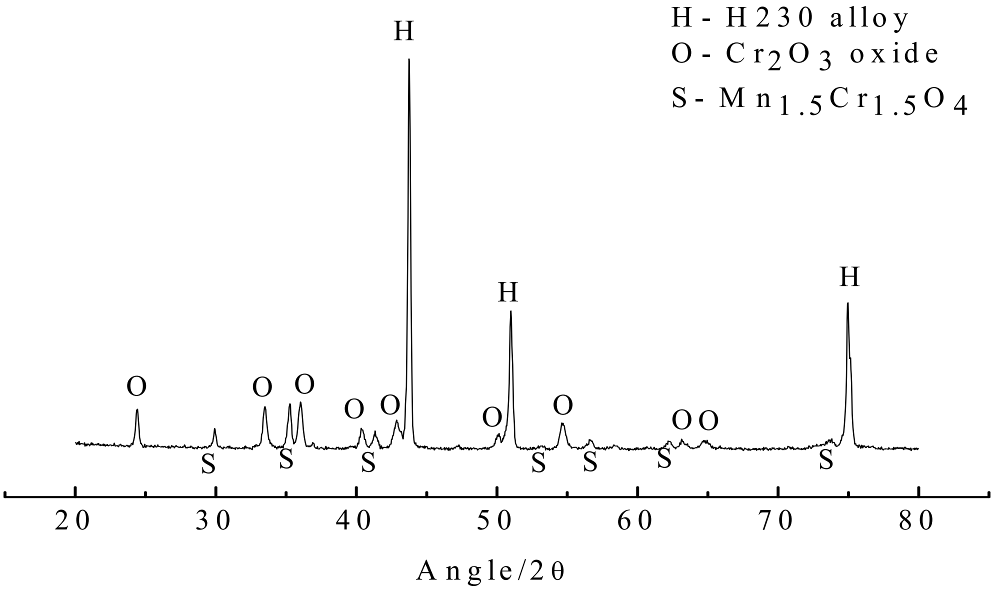

Fig. 2.8a: An XRD pattern of uncoated H230 foil oxidized for 1080 hrs in air at 800^{o}C.

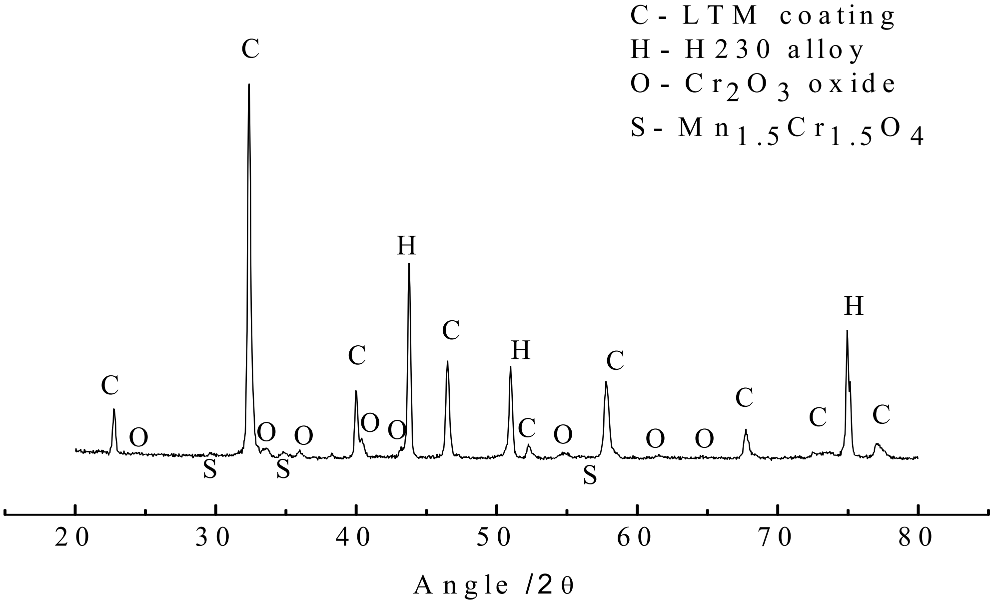

Fig. 2.8b: An XRD pattern of H230 foil coated with 1 μm of LTM oxidized for 1080 hrs in air at 800°C

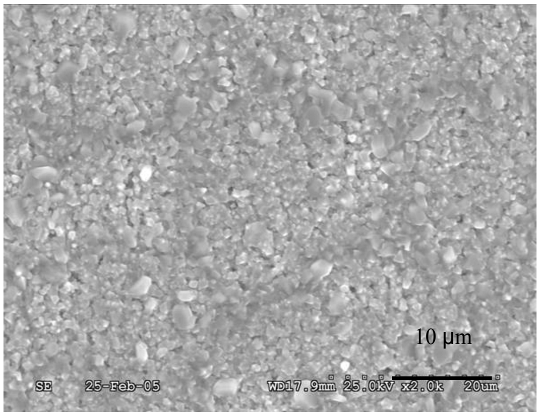

H230 Uncoated foil

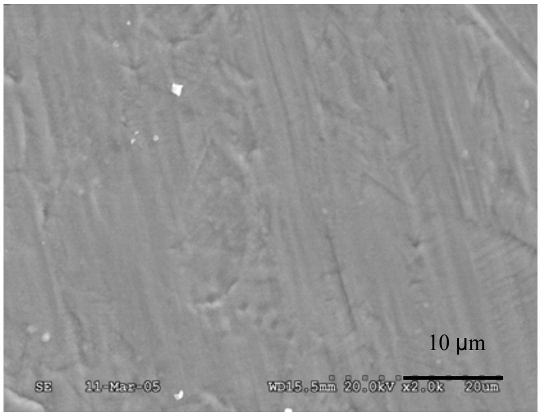

H230 coated with 1 μm LTM

Fig. 2.9: SEM micrographs of the surfaces of uncoated and LTM-coated (1 μm) H230 foils, oxidized for168 hrs in air at 800°C.

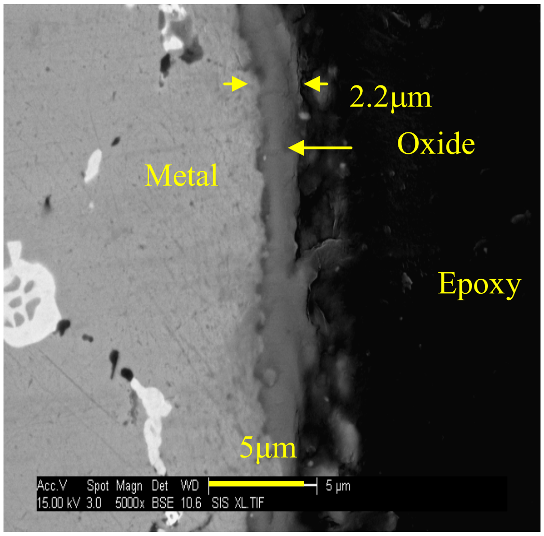

H230 foil

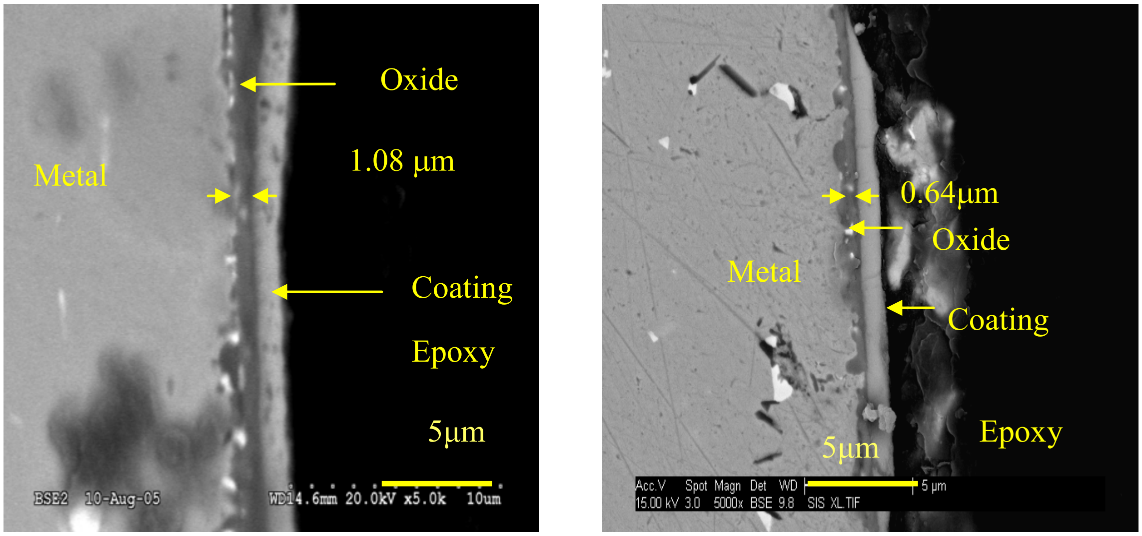

H230 foil coated with 1 µm LSM

H230 foil coated with 1 µm LTM

Fig. 2.10: SEM micrographs (edgewise) of uncoated, LSM-coated (1 µm) and LTM-coated (1 µm) H230 foils oxidized for 1080 hrs in air at 800°C.

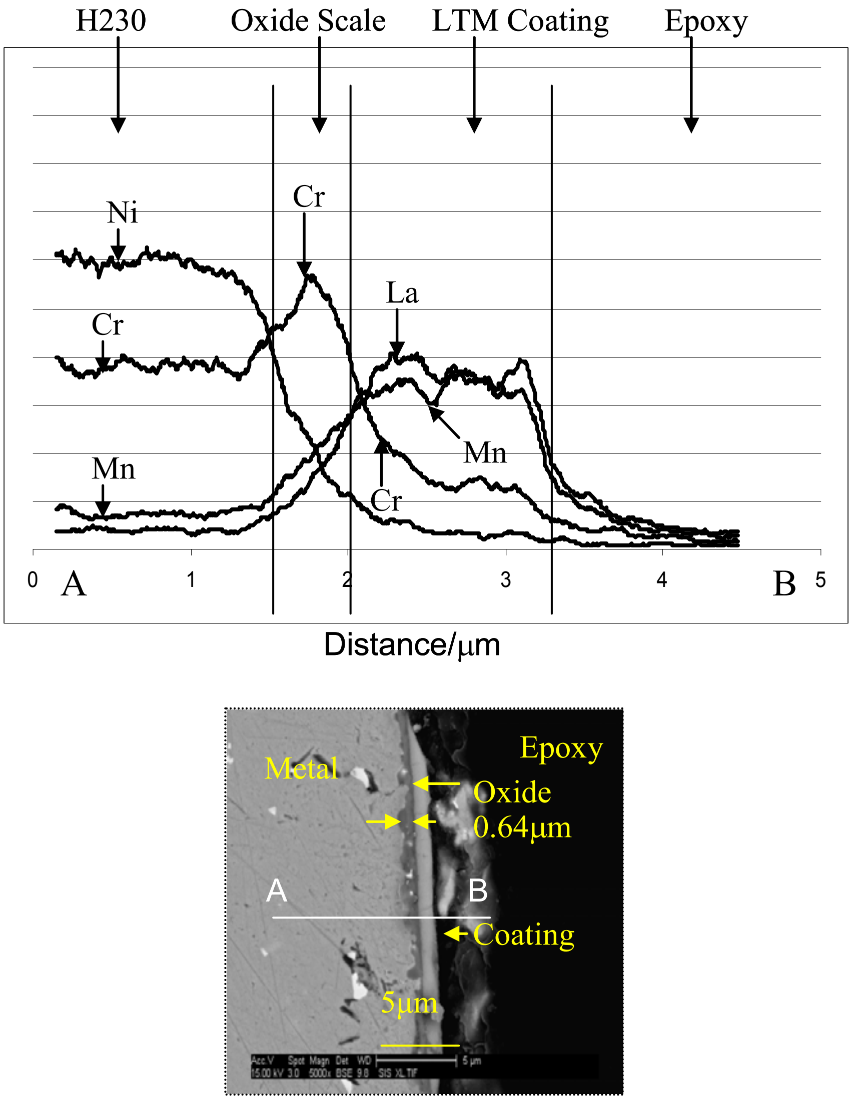

Fig. 2.11: EDAX analysis of H230 coated with 1 μm LTM oxidized in air at 800°C for 1080 hours.

coating, oxidized in air at 800°C for 1080 hours, which also confirms the formation of oxide scale underneath the coating. This shows that oxygen transports through the coating, forming an oxide scale on the surface of the alloy underneath the coating. The EDAX analysis shows spatial variations in compositions that appear smoothened out. This in part is related to the fact that the beam size is on the order of a micron, while the oxide scale and the coating are also on the same order of magnitude. However, it is to be noted that there is a significant concentration of chromium in the LTM coating. Thus, it appears that some interdiffusion on the cation sublattice must have occurred. That is, the coating composition did change during the process of oxidation. Similarly, some diffusion of La and Mn has also occurred into the oxide scale. In this context, the chemistry of oxide scale on an uncoated H230 foil is in general different from that which forms in coated foils. The significance of this will be discussed later.

Fig. 2.10 shows that the uncoated H230 foil formed the thickest oxide scale of 2.2 μm followed by foils coated with LSM (1.08 μm) and LTM (0.63 μm). The observation that LTM-coated foil exhibited the smallest oxide scale is in accord with the defect chemistry-based approach discussed in sections 2.2 and 2.3, which suggests that of the coating materials used in this study, LTM has the lowest oxygen ion conductivity and LSM has the highest.

2.4.3 Kinetics of Oxidation:

Fig. 2.12 shows a plot of the square of oxide scale thickness, x_f^2, vs. time of oxidation, t, for H230 uncoated foils. The slope of the plot gives the k_f, i.e. parabolic rate constant, which is equal to 1.21 x 10^{-14}cm^2/s.

Fig. 2.13 shows plots of oxide scale thickness vs. time of oxidation for H230 foils with 1 μm thick coatings of LM, LSM, and LTM. Also shown in the figure is a plot of x_f vs. time for uncoated H230. The growth of the oxide layer vs. time for the coated samples can be expressed by equation (2.4) (or equation (2.1)). The values of k_c i.e. kinetic parameter for oxygen permeation through the coating can be obtained by fitting the quadratic equation (2.4) through the experimentally obtained data points in Fig. 2.13 using k_f = 1.21 x 10^{-14} cm^2/s determined for the base alloy. From the best fit to the data, the corresponding values of k_c for various coating materials were estimated. The values are: For LSM, k_c = 1.51 x 10^{-14} cm^2/s, for LM, k_c = 7.1 x 10^{-15} cm^2/s, and for LTM, k_c = 3.96 x 10^{-15} cm^2/s. These results are again consistent with expectations based on defect chemistry; LSM should have the highest oxygen ion conductivity of the three coating materials studied, and thus should exhibit the highest k_c, as observed. Similarly, LTM should have the lowest oxygen ion conductivity of the three materials studied, and thus should exhibit the lowest k_c, as observed. It is apparent from the plots that the quadratic curve for the data points obtained for LTM coated H230 is almost linear over the duration of oxidation and thus can also be approximated by equation (2.6). These graphs, therefore, are in support of the hypothesis that even a small change in defect chemistry of the perovskite alters its oxygen ion conductivity significantly, and that donor doping on the B site of $LaMnO_3$ suppresses oxygen ion conductivity.

Based on the values of k_c and k_f from the above measurements, theoretical values of the thickness of oxide scale, x_f, that would form after 40,000 hours of operation at 800°C, which is the targeted service life of SOFC in stationary applications, can be estimated. For uncoated H230 foil and H230 foil with a 5 μm thick coating of

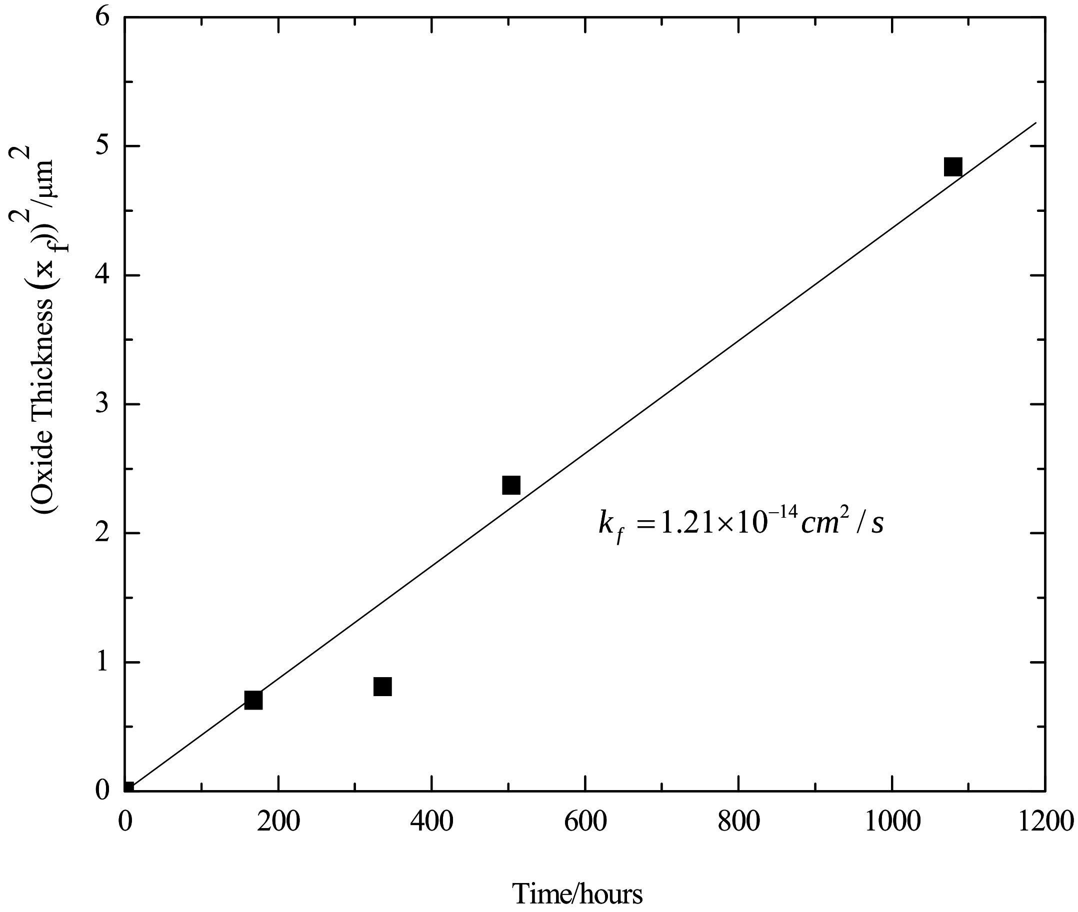

Fig. 2.12: A plot of (oxide scale thickness)^2 vs. time of oxidation at 800°C for uncoated H230 foil.

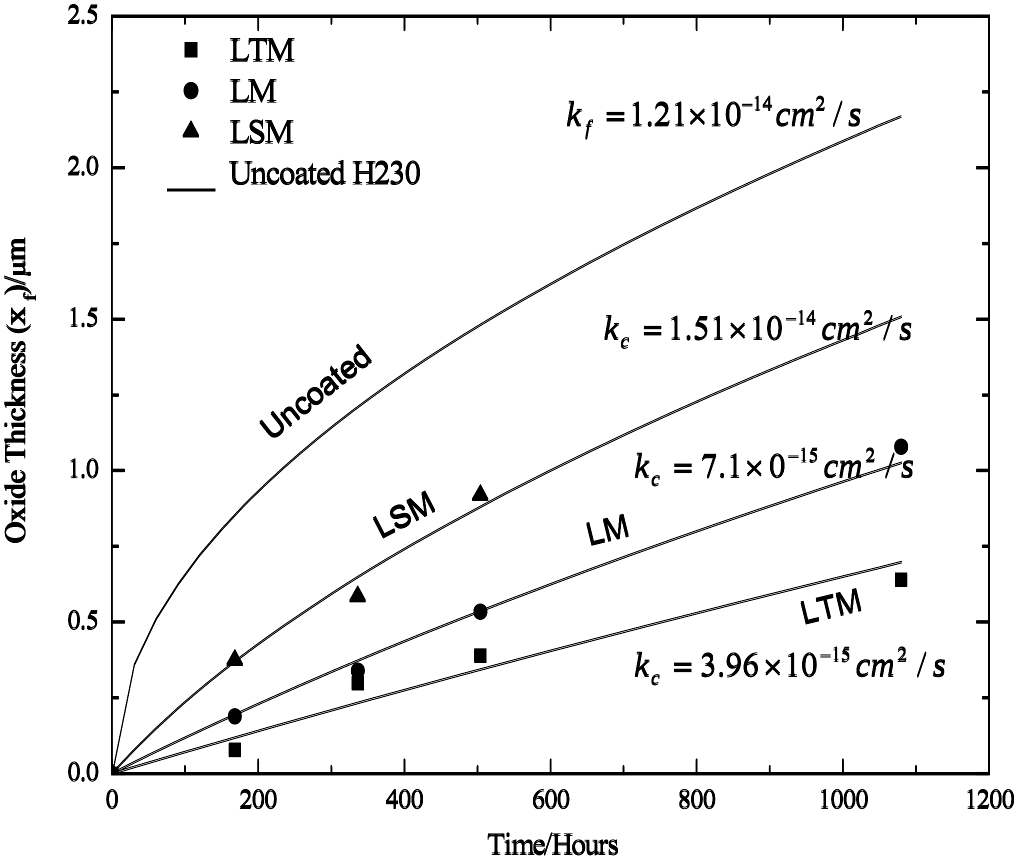

Fig. 2.13: Plots of oxide scale thickness vs. time of oxidation at 800°C for uncoated H230 and H230 with 1 µm coatings of LSM, LM and LTM. Lines through data points are fits to equation (2.4).

LSM, LM, and LTM, the x_f was estimated at 40,000 hours. The estimated values of x_f are: 13.2 μm for uncoated H230, 9.7 μm for LSM-coated, 7.1 μm for LM-coated, and 4.9 μm for LTM-coated. Plots of x_f vs. time are given in Fig. 2.14. Though there is a significant difference in oxide scale thicknesses between uncoated H230 and LTM-coated H230, the projected 4.9 μm oxide scale thickness for SOFC applications over 40,000 hour life is still too thick. Thus, with the LTM coating developed here, the thickness of the coating will have to be increased. Fig. 2.15 shows the estimated oxide scale thickness, x_f, vs. time of oxidation for H230 foil with 15 μm, 5 μm, and 1 μm thick LTM coatings as well as for uncoated H230 foil. With a 15 μm coating of LTM, the estimated oxide scale thickness, x_f, after 40,000 hours is only 1.8 μm, which is rather small and represents a reduction in scale thickness by 87% over uncoated H230. Thus, from these calculations, it is clear that even though 1 μm coating of LTM significantly suppressed the oxidation kinetics of H230, it still is too thin for long duration interconnect application and a thicker LTM coating of around 15 μm is required for adequate protection. Alternatively, a material with a k_c ~1 x 10^{-15} cm^2/s needs to be developed which should satisfy the 40,000 hours requirement at a coating thickness of 5 μm.

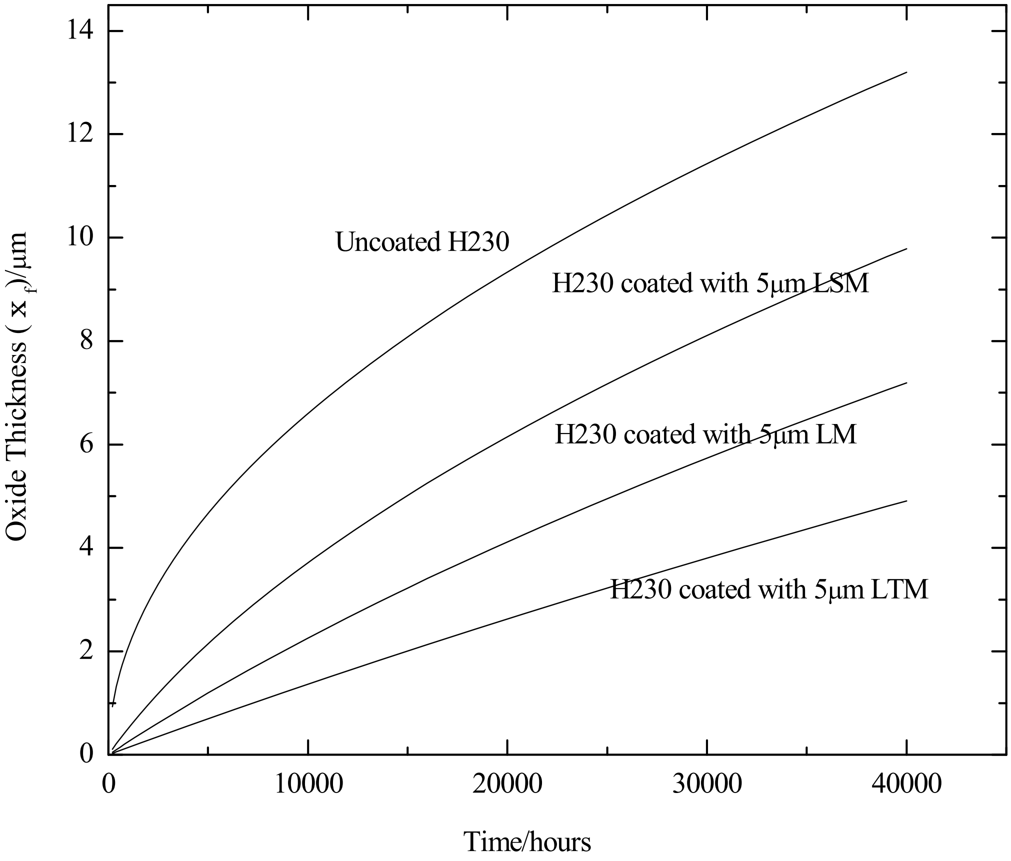

Fig. 2.14: Theoretical plots of oxide scale thickness vs. time of oxidation at 800°C for uncoated H230 and H230 with 5 μm thick coatings of LSM, LM and LTM.

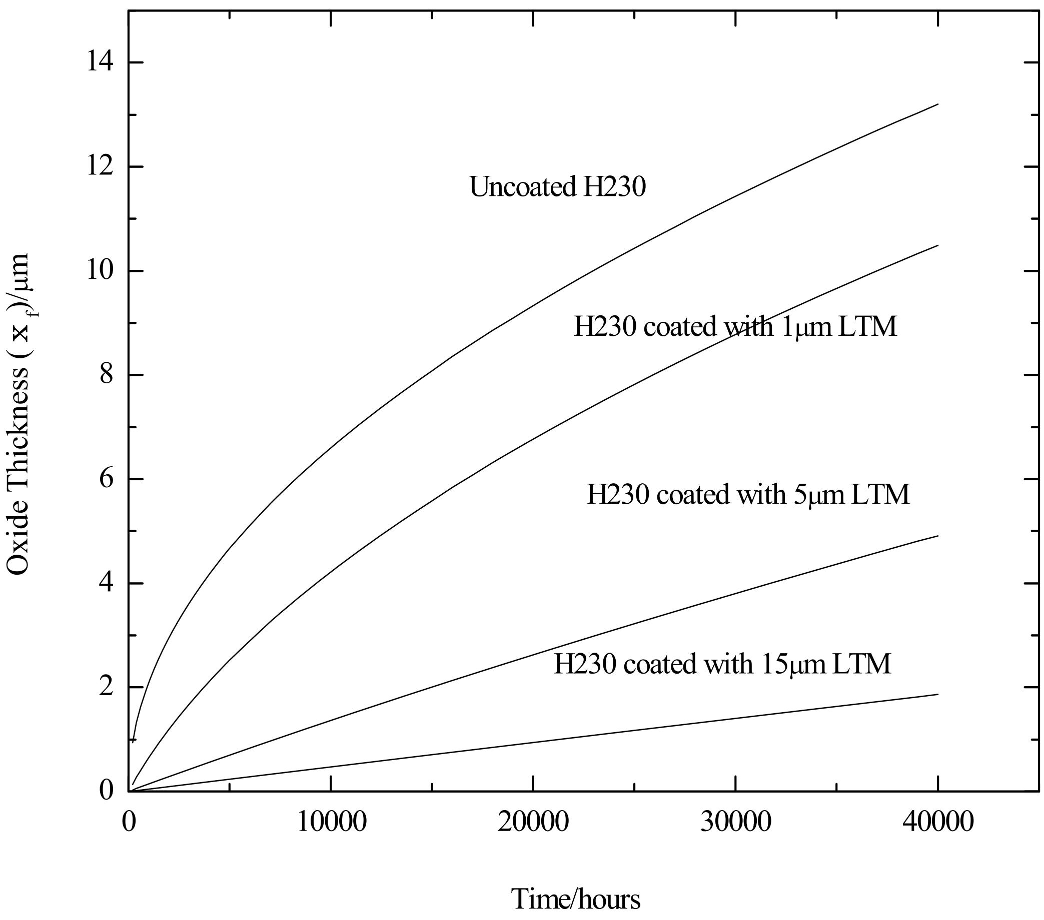

Fig. 2.15: Theoretical plots of oxide scale thickness vs. time of oxidation at 800°C for uncoated H230 and H230 with LTM coatings of thickness 1 μm, 5 μm, and 15 μm.

2.4.4 Area Specific Resistance (ASR):

Fig. 2.16 shows ASR vs. temperature plots for uncoated H230 foil, and H230 foils with 1 μm coatings of LTM and LSM, oxidized in air for 504 hours at 800°C. The ASR was the highest for uncoated foil and the lowest for LTM-coated foil, with the LSM-coated foil exhibiting intermediate behavior. These results further support the hypothesis concerning the role of defect chemistry of the coating material in determining oxidation kinetics of coated foils. In Fig. 2.16, the ASR data are plotted on an Arrhenius graph. The lowest ASR value at 800°C, 0.014 Ωcm^2, was obtained for H230 foil with 1 μm coating of LTM oxidized for 504 hours. The ASR for the LSM-coated sample is ~0.034 Ωcm^2 and for the uncoated sample the ASR value is ~0.07 Ωcm^2.

Several important conclusions can be drawn from these results. First, note that for the LTM-coated sample, the ASR is lower than that for the LSM-coated. This is principally due to the fact that oxide scale thickness in the LTM-coated sample is smaller than in the LSM-coated sample. Thus, even though the electronic conductivity of LSM is higher than that of LTM, the net ASR of the LTM-coated sample is lower. As stated earlier, as long as the electronic conductivity of the coating is sufficiently high (above about 1 S/cm), its contribution to the total ASR is negligible (<0.001 Ωcm^2 for a 10 micron coating). That is, the present work shows that the important criterion for the selection of coating material is not its electronic conductivity, but its oxygen ion conductivity which should be as low as possible.

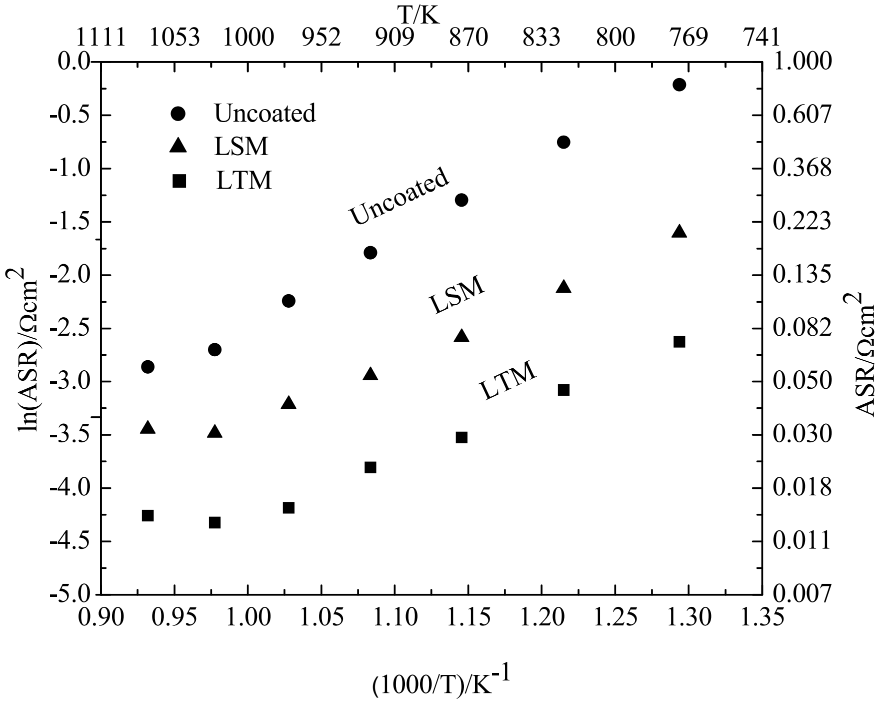

Fig. 2.16: Plots of ASR vs. 1000/T for uncoated and coated H230 metal foils with 1 μm coatings of LSM and LTM, oxidized in air at 800°C for 504 hours.

Second, note that the ASR of the LTM-coated sample is ~0.014 Ωcm^2 while that of the uncoated sample is ~0.07 Ωcm^2, or five times larger. However, the oxide scale thickness in the uncoated sample is not five times that in the LTM-coated sample. Thus, this difference in ASR cannot be attributed solely to differences in oxide scale thicknesses. These results suggest that electronic conductivity of the oxide scale in LTM-coated sample must be higher than in the uncoated sample. This is entirely possible in view of the possible changes that can occur in the composition of the oxide scale (and also of the coating) in coated samples due to the occurrence of interdiffusion. We expect that some Mn and La diffused into the oxide scale thus increasing its electronic conductivity (and some Cr diffused into the coating). Issues pertaining to interdiffusion between the coating and oxide scale are discussed later.

Based on the value of the ASR of 1 micron LTM-coated H230 oxidized for 504 hours in air, the projected ASR after 40,000 hours of operation as interconnect in an SOFC stack is estimated to be ~0.37 Ωcm^2 (corresponding to an oxide scale thickness of ~10.4 μm). This value is too high, and suggests that even with LTM as a coating, which is by far the best coating reported to date, the thickness of the coating will have to be greater than 1 μm. In the case of a 15 μm thick LTM coating, the oxide scale thickness after 40,000 hours is projected to be 1.8 μm with the corresponding ASR of 0.064 Ωcm^2. This shows that the required LTM coating thickness to guarantee 40,000 hour life is ~15 μm. The LTM of composition $LaMn_{0.9}Ti_{0.1}O_{3+\delta}$ used in the present work is by no means optimized. It is expected that by further optimization of composition, a k_c of ~1 x 10^{-15} cm^2/s should be possible, for which the required coating thickness to guarantee 40,000 hour service life is only 5 μm.

2..4.5 Comparison with $La_{0.85}Sr_{0.15}O_{3-\delta}$ (LSM) and Mn_2CrO_4 Spinel Coatings:

Armstrong et al. [24] studied the kinetics of oxidation of H230 in air at 800°C with 1.3 micron coatings of $La_{0.85}Sr_{0.15}O_{3-\delta}$ and Mn_2CrO_4. Coatings of these materials were also deposited by sputtering and the experimental procedure was essentially the same as in the present work. From the oxidation kinetics studies, for LSM of the above composition, the coating kinetic parameter determined is $k_c = 2.86 \times 10^{-14}$ cm^2/s. In the present work on LSM of composition $La_{0.95}Sr_{0.05}MnO_{3-\delta}$, the coating kinetic parameter determined is $k_c = 1.51 \times 10^{-14}$ cm^2/s. The higher value of k_c in the work of Armstrong et al. is entirely consistent with defect chemistry considerations. Note that in the work by Armstrong et al., the Sr content was higher (15% vs. 5% in the present work), which leads to higher oxygen vacancy concentration, and thus higher oxygen ion conductivity, and thus higher k_c. For the Mn_2CrO_4 spinel coating, the kinetic parameter of the coating in the work by Armstrong et al. was determined to be $k_c = 9.1 \times 10^{-14}$ cm^2/s. Note that this value of k_c for spinel coating is ~23 times greater than that for LTM coating of this study. It is thus clear that preferred coating is perovskite-based, and it is far superior to Mn-Cr-based spinels.

2.4.6 Interdiffusion between the Coating and the Oxide Scale:

The oxide scale is predominantly Cr_2O_3, while the coating is a perovskite. Interdiffusion of cations between the coating and the oxide scale is expected. As stated earlier, EDAX measurements suggest the occurrence of some interdiffusion. EDAX measurements, however, are not definitive due to the beam size being on the same order of magnitude as the oxide scale and the coating thicknesses. An alternative albeit indirect evidence of interdiffusion can be obtained from the relative changes in the thicknesses of the coating and the oxide scale. Fig. 2.10 shows edgewise SEM micrographs of samples oxidized for 1080 hours at 800^oC in air. Prior to oxidation, the coating thicknesses were 1 micron in each case. After oxidation, it is noted that the thickness of the LTM coating is ~1 micron, even after 1080 hours of oxidation (Fig. 2.10), indicating very small amount of interdiffusion, not enough to reflect as a significant change in thickness but probably enough to alter electronic conductivity of the scale. For the LSM coating, the measured coating thickness after 1080 hours is ~1.3 microns, which indicates some growth of the coating thickness. This suggests a greater amount of interdiffusion in the case of LSM coatings than LTM coatings.

No systematic studies involving the measurement of oxide scale thickness as a function of oxidation time have been reported with Mn-Co-spinel as a coating material on any of the prospective interconnect alloys. Some work has been reported by Yang et al. on the oxidative behavior of Crofer22 APU alloy with Mn-Co-spinel coating [26]. These studies nevertheless provide some insight into the nature of diffusive processes. This is discussed in what follows.

Figure 3(a) of Yang et al. shows an SEM micrograph of Crofer22 APU alloy with a Mn-Co-spinel coat after a 24 hour treatment at 800^oC. The Mn-Co spinel coating thickness is ~6 μm while the oxide scale formed is ~2 μm, for a total thickness (coating + oxide scale) of ~8 μm. Figure 3(b) of Yang et al. shows an SEM micrograph after 100 hours at 800^oC. The oxide scale is ~1.5 μm, while the Mn-Co-spinel oxide layer is ~ 8 μm, for a total thickness of ~9.5 μm. Several interesting conclusions emerge from these observations. First the net thickness of the oxide + coating increased by about 1.5 μm in 100 hours, indicating significant oxidation. The oxide scale thickness, slightly decreased but the coating thickness increased. This shows significant diffusion and dissolution of the scale into the coating, consistent with generally known rapid cation transport in spinels [34]. Yang et al. have also given an SEM micrograph after 6 month oxidation (4,368 hours) at 800^oC in their Figure 6(a). The coating thickness in this micrograph is ~14 μm while the oxide scale thickness is ~3.5 μm, for a total thickness of ~17.5 μm. That is, the total thickness grew from an initial ~8 μm to ~17.5 μm in 4,368 hours, indicating a significant amount of oxidation. Also seen in Figure 6(a) of Yang et al., morphological changes observed in the alloy extend to a depth over 20 μm, which probably represents the region from which Cr was removed during oxidation. These observations suggest that significant oxidation in fact does occur with Mn-Co-spinel as the coating, and is consistent with expectations based on transport studies in spinels [34].

2.5 Additional substrate materials of study

Apart from Haynes 230 (H230) alloy, Inconnel 718 (INC718), another Ni-Cr alloy, and Stainless steel 430 (SS430), Fe-Cr alloy were also studied. As compared to H230 alloy, INC718 and SS430 exhibit faster oxidation kinetics [13], SS430 exhibiting the fastest kinetics [35]. In this section detail study of oxidation kinetics of coated and uncoated INC718 and SS430 oxidation will be discussed.

Inconnel 718: As mentioned before, Ni-Cr super alloys (composition given in table 2.II) generally have high thermal expansion coefficient (around $15x10^{-6}$ K^{-1}), which is different from rest of the SOFC component materials. This may cause excessive strain during operation cycle. But this can very well be prevented by using thin flexible foil. Oxidation of INC718 develops Cr_2O_3 scale on the surface of the alloy, which is highly resistive and volatile. But its two important properties such as slower oxidation kinetics than Fe-Cr alloys, and adherent oxide scale qualify this material for interconnects usage.

Same experimental procedures were followed for INC718 as that for H230. And its results are discussed in this section.

Table 2.II: Composition (mole%) of INC718 alloy

Elements	Ni	Cr	Fe	Mo	Mn	Co	W
Mole %	53	22	18	1.9	0.38	1	0.9

2.5.1 Results and discussion:

Fig. 2.17 shows the surface micrographs of uncoated INC718 alloy foil and INC718 alloy foil with 1 μm thick LTM coating, oxidized in air at 800^0C for 168 hours. The uncoated foil was completely covered with a grainy oxide layer but coated foil was relatively unchanged. This indicates that coating is effective in inhibiting the ingress of oxygen. Fig. 2.18a and 2.18b show the XRD patterns of oxidized INC718 with and without coating. As in the case of H230, here also, predominant oxide product is Cr_2O_3 along with some $Mn_{1.5}Cr_{1.5}O_4$.

Fig. 2.19 shows the comparison of oxide scale thickness among uncoated INC718 and INC718 coated with LSM, and LTM, oxidized in air at 800^0C for 1080 hours. The uncoated sample formed the thickest oxide scale of 4.9 μm, while LTM coated sample formed the thinnest oxide scale of 1.93 μm with LSM coated foil forming 2.16 μm. This behavior is in accord with defect chemistry approach.

The significant difference in oxide scale thickness, between H230 and INC718 for same duration at same temperature, is because of difference in kinetics of oxidation observed in INC718 and H230 alloy foils. The value of k_f i.e. parabolic rate constant obtained for INC718 by plotting square of oxide scale thickness vs. time of oxidation is $4.3x10^{-14}cm^2/s$ as shown in fig. 2.20, which gives clear indication of faster oxidation kinetics of INC718 as compared to H230. The values of k_c for different coating

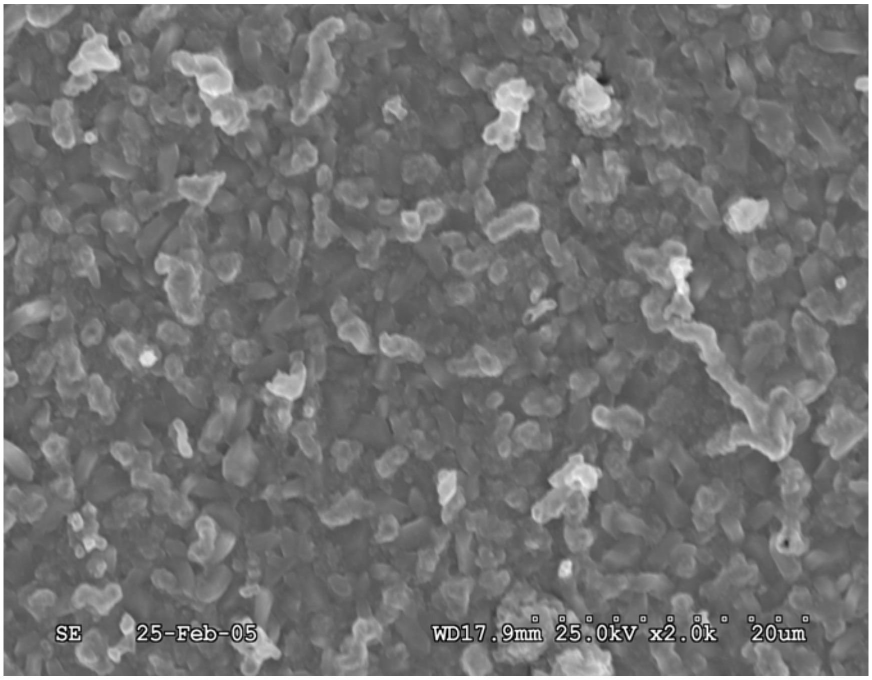

INC718 Uncoated foil

INC718 coated with 1µm LMT

Fig. 2.17: SEM micrographs of the surfaces of uncoated and LTM-coated (1 µm) INC718 foils, oxidized for168 hrs in air at 800°C.

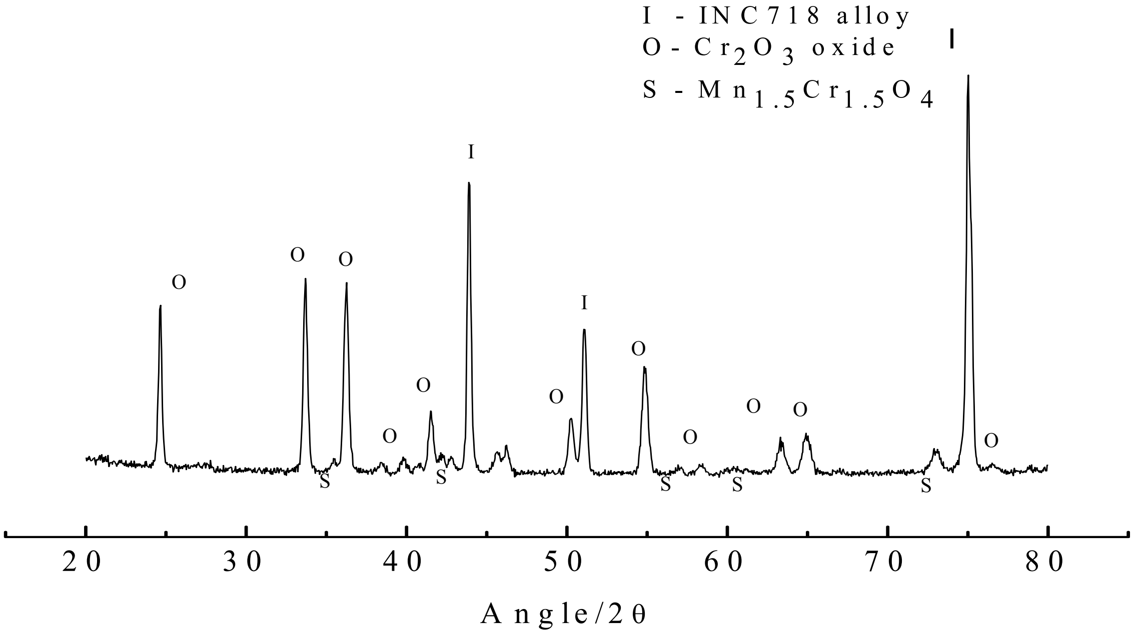

Fig. 2.18a: An XRD pattern of uncoated INC718 foil oxidized for 1080 hrs in air at 800°C.

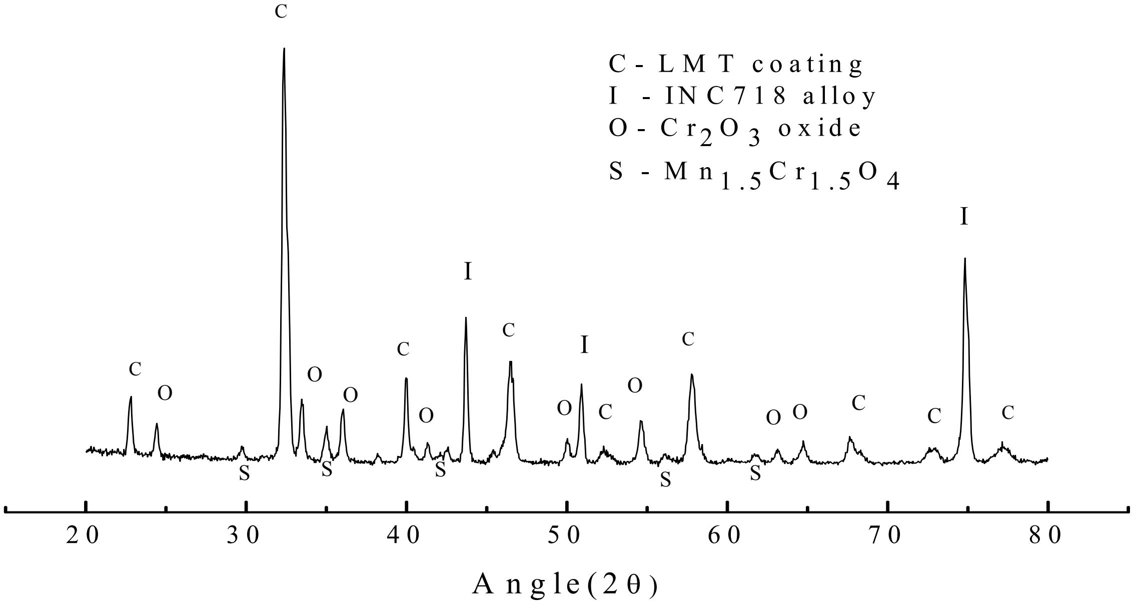

Fig. 2.18b: An XRD pattern of INC718 foil coated with 1 μm of LTM oxidized for 1080 hrs in air at 800°C.

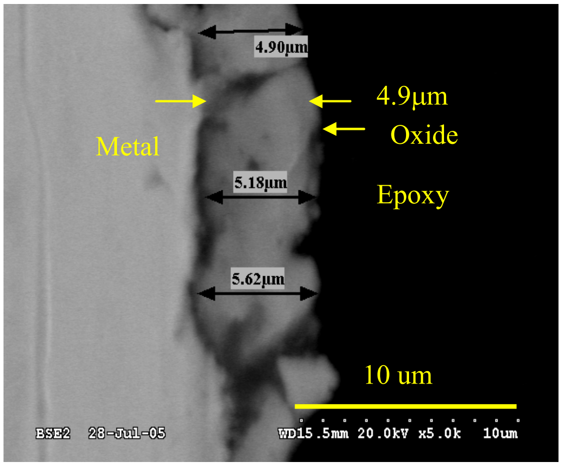

INC718 foil

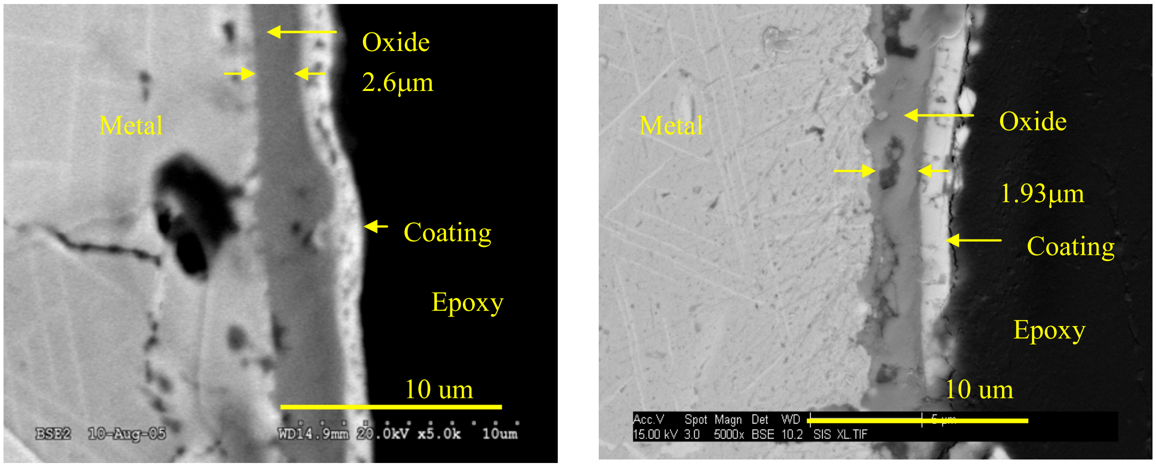

INC718 foil coated with 1µm LSM

INC718 foil coated with 1µm LMT

Fig. 2.19: SEM micrographs (edgewise) of uncoated, LSM-coated (1 µm) and LTM-coated (1 µm) INC718 foils oxidized for 1080 hrs in air at 800^{o}C.

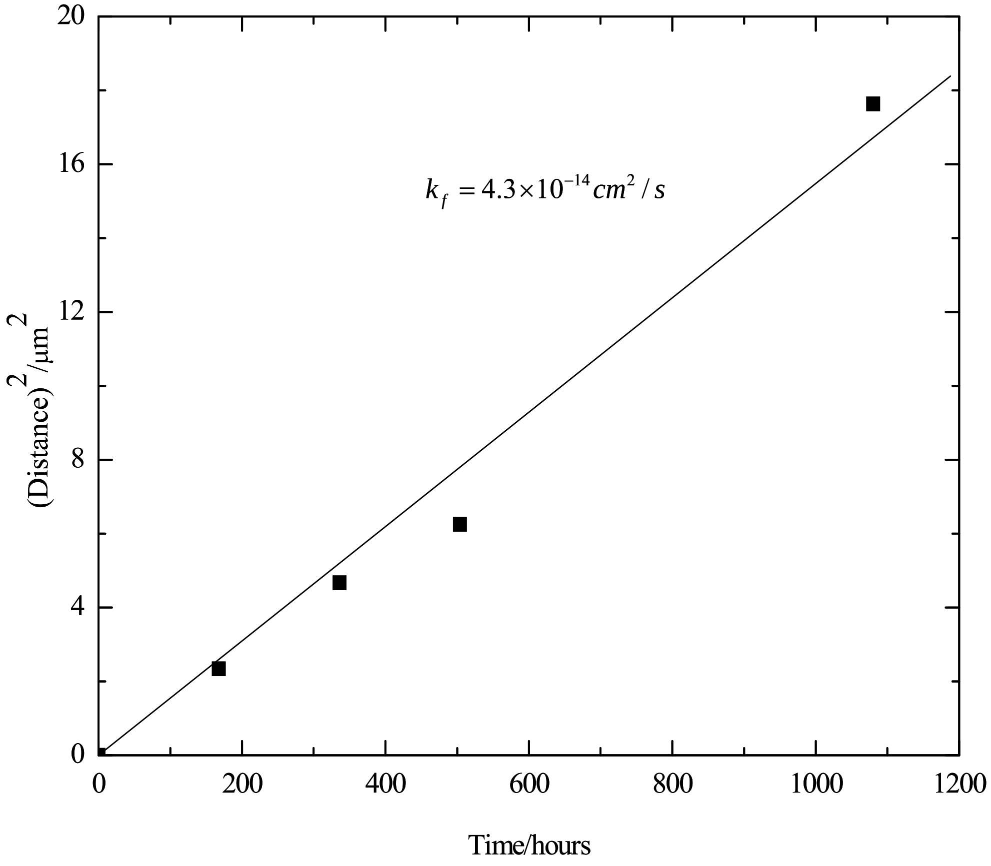

Fig. 2.20: A plot of (oxide scale thickness)^2 vs. time of oxidation at 800°C for uncoated INC718 foil.

materials were also calculated by fitting curve through the experimental obtained data points as shown in fig. 2.21 (using k_f = 4.3x10^{-14}cm^2/s). k_c for LSM = 2.83x10^{-14}cm^2/s, k_c for LM = 2.14x10^{-14}cm^2/s, k_c for LTM = 1.26 x10^{-14}cm^2/s. It is evident from the above data that the kinetics of oxygen permeation through the coating is the lowest for LTM coating and the highest for LSM coating. These graphs, therefore, are in support with the hypothesis that even a small change in defect chemistry of the perovskite, alters its oxygen ion conductivity significantly and donor doping on the B site of $LaMnO_3$ suppresses the oxygen ionic conductivity of the perovskite.

k_c, kinetic parameter of permeation of oxygen through coating, is the property of particular coating. It should be the same irrespective of substrate material. If the coating is protective enough with adequate thickness, oxidation would be governed by the coating and would be independent of the substrate. But in our case, two different values of k_c were obtained for same coating when deposited on H230 and INC718 substrates. This is only possible if the coating is partially protective for the applied thickness, and the kinetics of oxidation is governed by k_c as well as k_f.

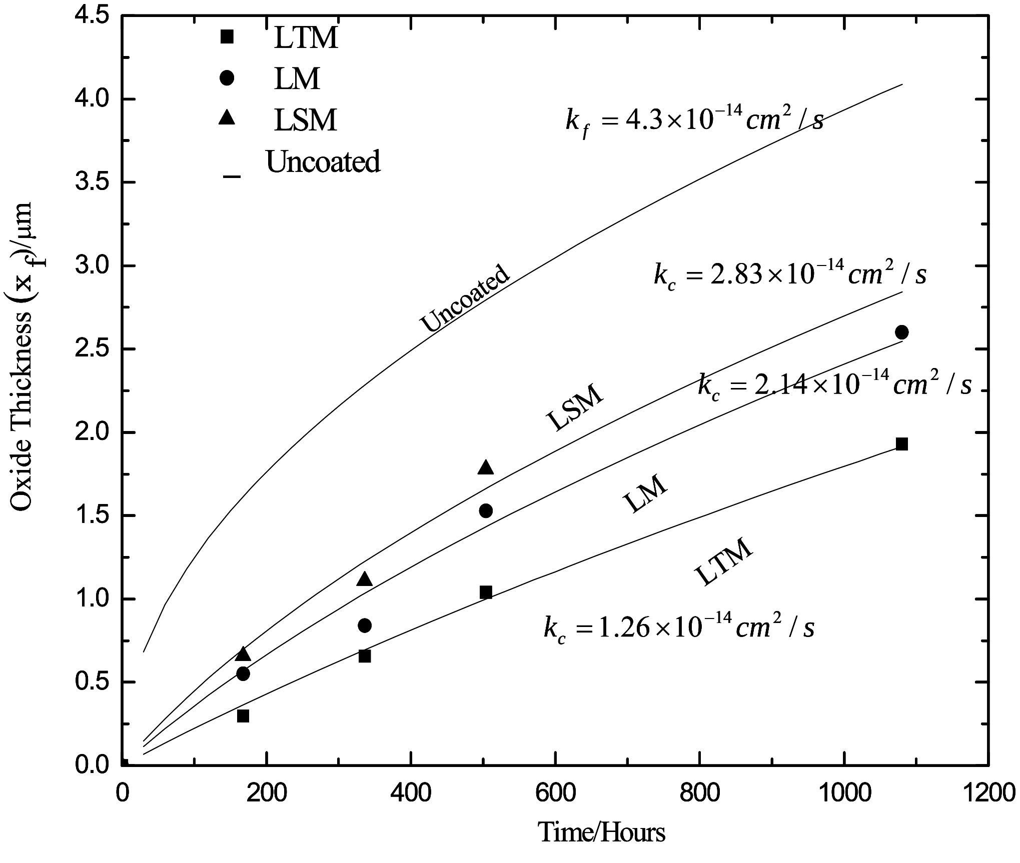

Fig. 2.21: Plots of oxide scale thickness vs. time of oxidation at 800°C for uncoated INC718 and INC718 with 1 µm coatings of LSM, LM and LTM. Lines through data points are fits to equation (2.4).

In these studies values of k_c are calculated indirectly, based on thickness of oxide scale accumulated underneath the coating. Although the coatings are protective, there could be formation of micro-cracks and some spalling as a result of extended oxidation. In such a case, oxide accumulation does not only depend on k_c but it also depends on k_f of the material. Therefore, the calculated k_c values would be different from theoretical k_c value, and would have partial contribution from k_f, which is higher for INC718 and lower for H230. This is the reason for higher value of k_c obtained for the same coating when deposited on the INC718 substrates. If the coating was thicker, effects of formation of micro-cracks and/or spalling would have been minimized and a same (or approximately same) value of k_c for H230 and INC718 would have been obtained; and the ideal value of k_c would be much lower than the calculated value.

Fig. 2.22 shows ASR vs. temperature plots for uncoated INC718 foil, and INC718 foils with 1 μm coatings of LTM and LSM, oxidized in air for 504 hours at 800°C. The ASR was the highest for uncoated foil and the lowest for LTM-coated foil, with the LSM-coated foil exhibiting intermediate behavior. These results further support the hypothesis concerning the role of defect chemistry of the coating material in determining oxidation kinetics of coated foils. The lowest ASR value at 800°C, 0.02 Ωcm^2, was obtained for INC718 foil with 1 μm coating of LTM oxidized for 504 hours. The ASR for the LSM-coated sample is ~0.036 Ωcm^2 and for the uncoated sample the ASR value is ~0.062 Ωcm^2. In this case ASR value of uncoated INC718 is smaller than that of uncoated H230 (but oxidation kinetics of INC718 is faster than H230). Reasonable amount of spalling of oxide formed on INC718 is the principal reason for this discrepancy. Thus, if INC718 substrate is used as interconnect material, thicker coating than in case of H230 alloy is required for protection.

2.6 Stainless Steel 430 (SS430)

Although H230 and INC718 are superior materials from oxidation kinetics standpoint, they are costly for commercialization. This is the principal reason for wide usage of SS430 foils as interconnect materials. But aggressive oxidation kinetics and excessive spalling tendency of formed oxide scale are the major factors of concern. Because of the above reasons protection of this material with 1μm protective coating is hardly effective. Fig. 2.23 shows the edgewise micrographs of uncoated SS430 and SS430 coated with 1 μm thick LTM coating, oxidized in air at 800°C for 168 hours. Here, it is apparent that the coated sample formed thinner oxide scale than the uncoated sample. But it was observed that as the time of oxidation increased, coating started falling apart, exposing SS430 to the atmosphere and causing excessive oxidation as shown in fig. 2.24. Thus, it was clear that thicker coating (5 to 10 μm) has to be applied to SS430 foil. Sputtering is very slow process, depositing coating of 5 to 10 μm in thickness is very time consuming and not at all practical. So, the deposition of coating by dip coating technique was one of the obvious choices. This section deals with the experimental procedures followed for dip coating and their outcome.

2.6.1 Experimental:

Slurry of LSM powder (Praxair, 99.99%) was prepared by dissolving in Methyl ethyl ketone solvent (MEK). (MEK:LSM = 2:1, by weight). Also, 1% binder - Polyvinyl butyral (PVB), 1% dispersant - Hypermer KD1 were added to the slurry. LSM powder was selected because of its easy commercial availability. And from previous chapter, one can claim that if LSM is effective as a coating material, LTM would be more effective. LSM powder and other additives was ball milled for 24 hours. Cleaned SS430 substrate foils were coated with the LSM by dipping in the slurry.

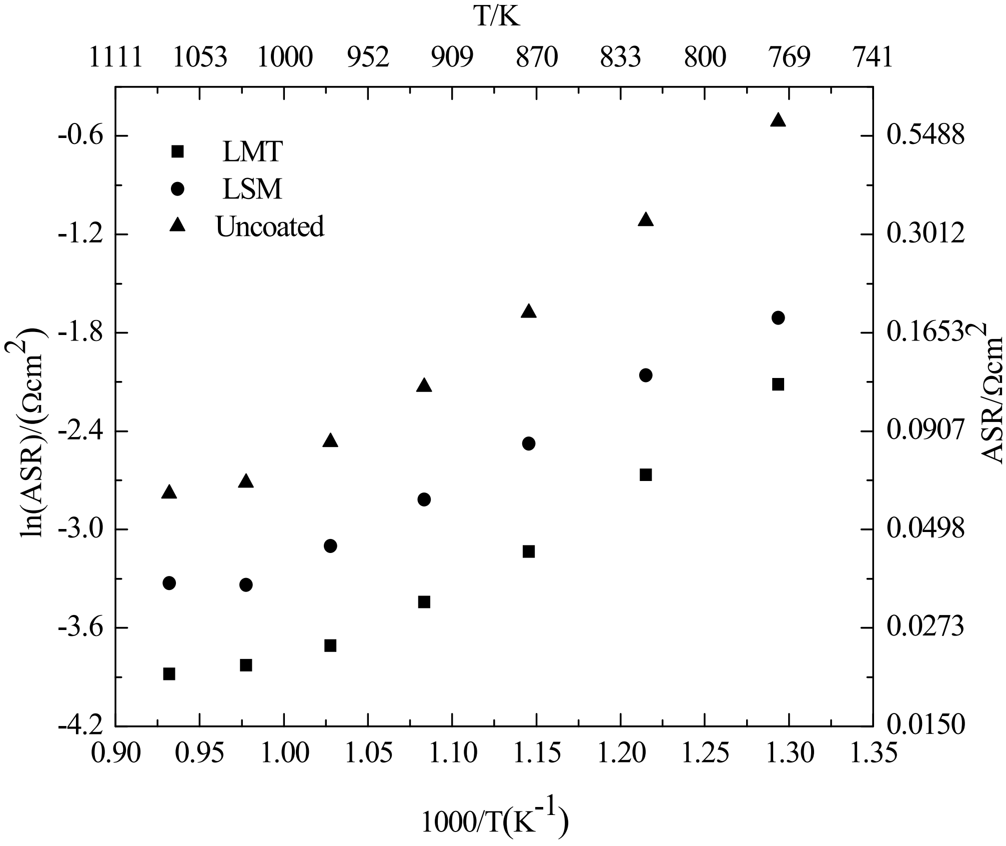

Fig. 2.22: Plots of ASR vs. 1000/T for uncoated and coated INC718 metal foils with 1 μm coatings of LSM and LTM, oxidized in air at 800°C for 504 hours.

A. foil was dipped into the slurry for 2 to 3 seconds, holding one corner by sample holder. As MEK is very volatile solvent, it did not take much time to dry. After drying, dip coated samples were annealed at 1000^{0}C for 2 hours. Some samples were annealed with the application of load. The load was applied with the help of spring loading assembly. After annealing, SEM analysis was conducted to see the difference between two types of samples.

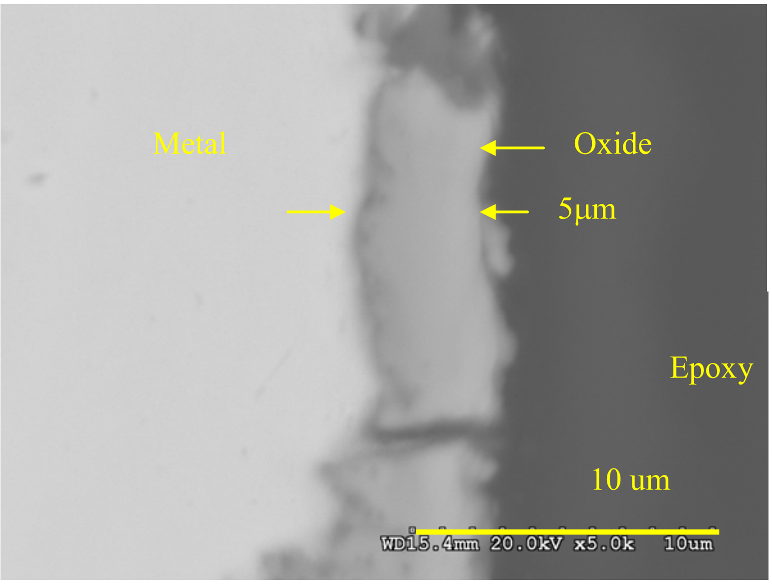

SS430

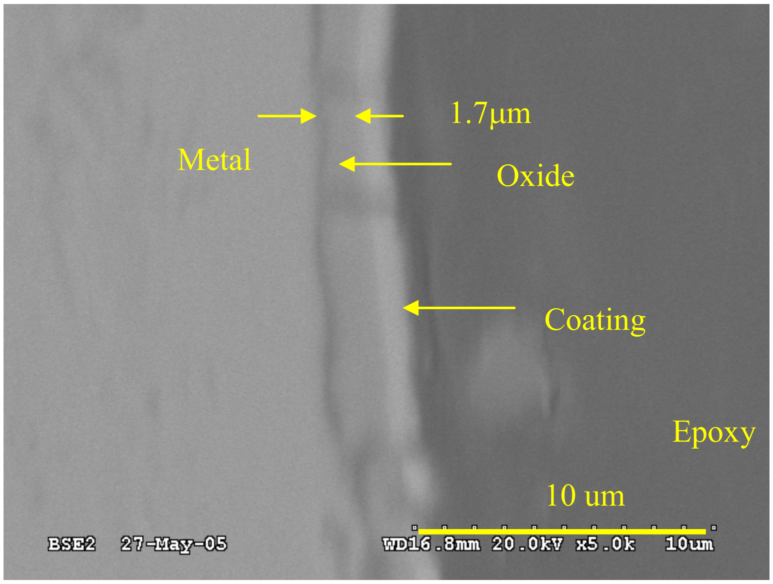

SS430 coated with 1μm
LTM

Fig. 2.23: SEM micrographs of uncoated and LTM coated (1μm) SS430 foils, oxidized for 168 hrs in air at 800^0C.

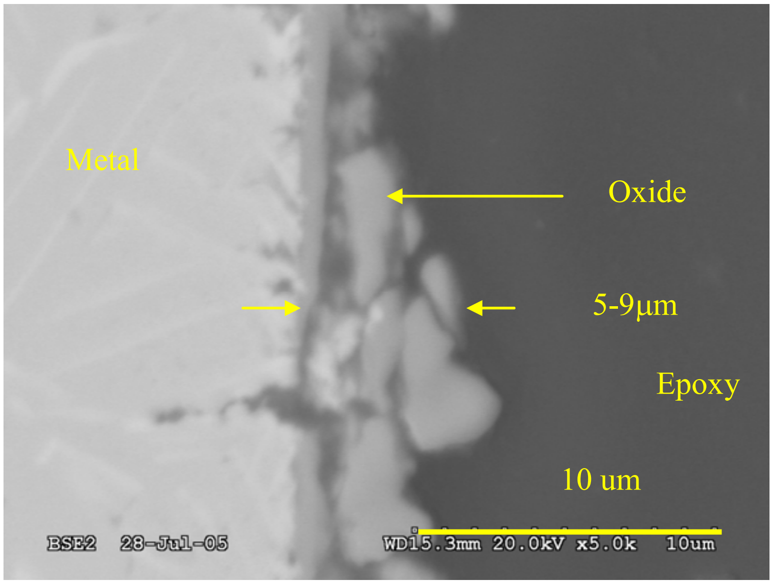

SS430

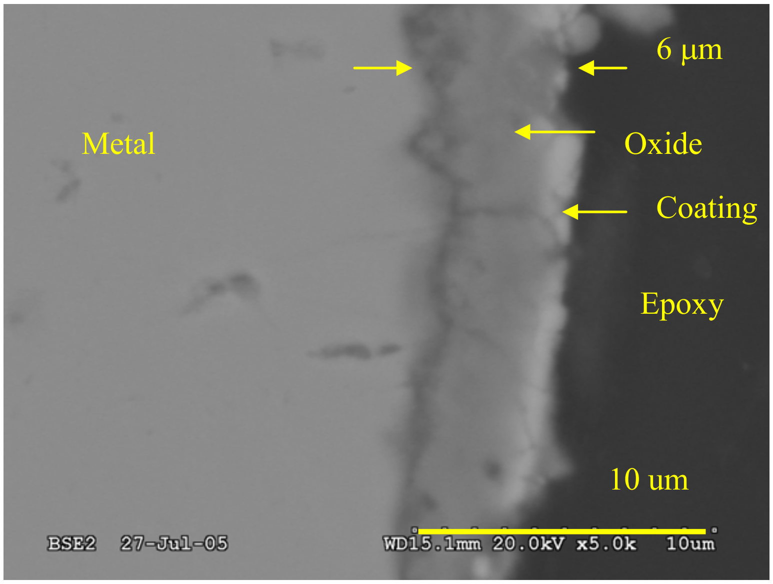

SS430 coated with 1µm
LTM

Fig. 2.24: SEM micrographs of uncoated and LTM coated (1µm) SS430 foils, oxidized for 504 hrs in air at 800^0C.

Remaining samples were heat treated in air at 800^0C for 168 hours. SEM analysis was also conducted on heat treated samples to examine the oxide growth and the surface condition.

2.6.2 Result and Discussion:

Fig. 2.25 shows the edgewise SEM micrographs of dip coated SS430 with LSM coating, annealed for 2 hours in air at 1000^0C. Sample A was annealed without any application of load while sample B was annealed with application of load. Significant difference was observed in the porosity of the coating. Sample B was denser than the sample A. This result was complimented by the surface micrographs of same samples as shown in fig. 2.26. In sample A, percentage of open porosity is significantly higher than in the sample B. This behavior implies that the applied load on the sample during annealing process increases the densification of the sample. Production of this kind of coated interconnect material can be conducted on mass scale by the process of hot rolling.

Fig.2.27 shows SEM micrograph of the dip coated sample after 168 hours of oxidation in air at 800^0C. It was observed that after 168 hours of oxidation, there was very little addition of oxide to the already existing oxide scale that was formed at the time of 1000^0C annealing. This trend indicates that once the coating is densified at 1000^0C, it acts as non porous adherent protection against oxidation. It was also observed that the porosity of the coating reduced further after 168 hours of heat treatment as shown in fig. 2.27. Dip coating technique is reasonable for SS430 because, as mentioned before, thicker coating is required for stainless steel to control its oxidation and sputtering technique can not deposit thick coating. Although quality of sputter-deposited coating is much better than dip coated coating, this technique is inexpensive and can easily be adopted for industrial use.

2.6.3 Future direction:

This technique can easily be adopted in industrial set up. Thus, production of coated interconnect materials is possible on large scale. Hot rolling fabrication process can be used for annealing after dip coating. This can apply adequate pressure for densification and performance of the coating can further be improved.

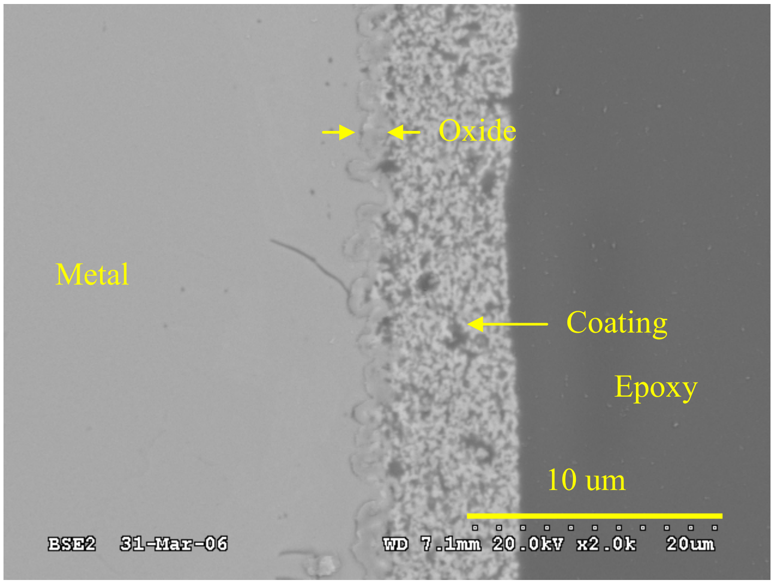

Annealed without application of pressure

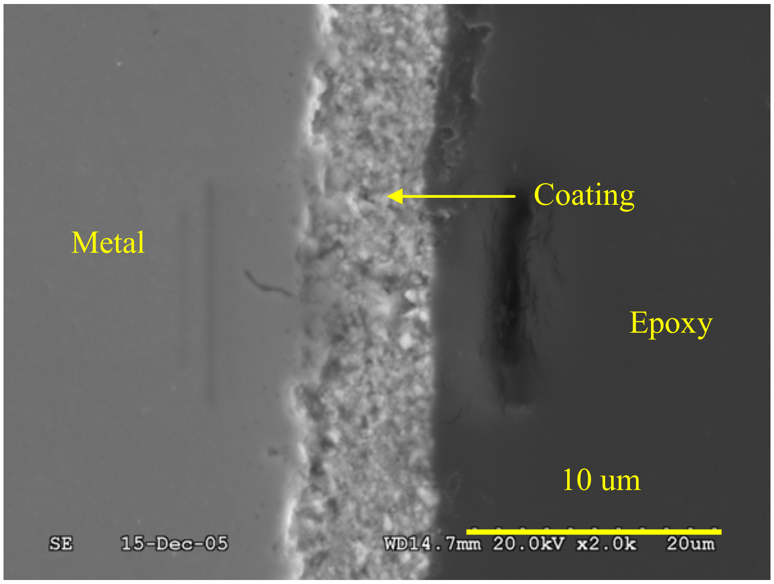

Annealed with application of pressure

Fig. 2.25: SEM micrographs of dip-coated SS430 foils with LSM0.85 coating, annealed at 1000^0C for 2 hours in air.

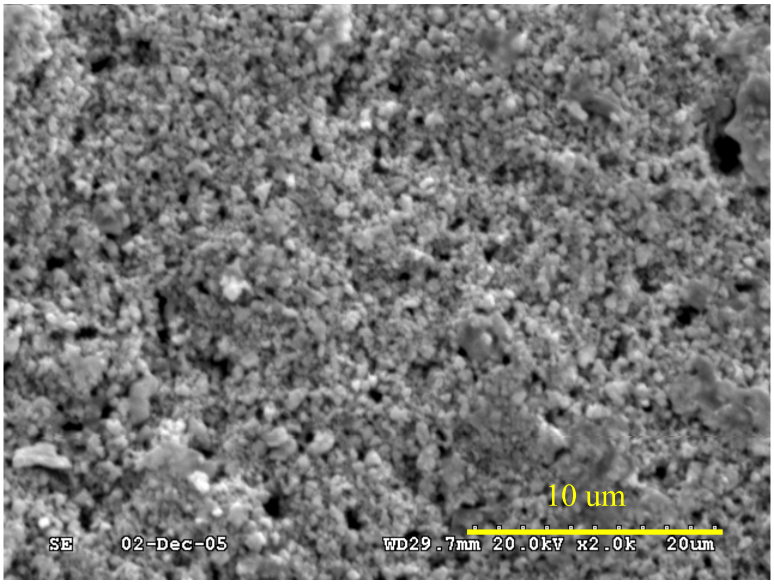

Annealed without application of pressure

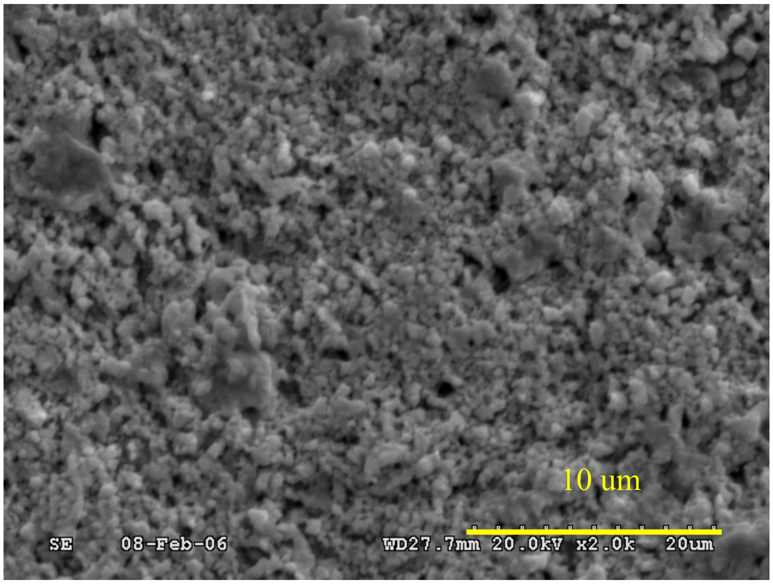

Annealed with application of pressure

Fig. 2.26: Surface SEM micrographs of dip-coated SS430 foils with LSM0.85 coating, annealed at 1000^0C for 2 hours in air.

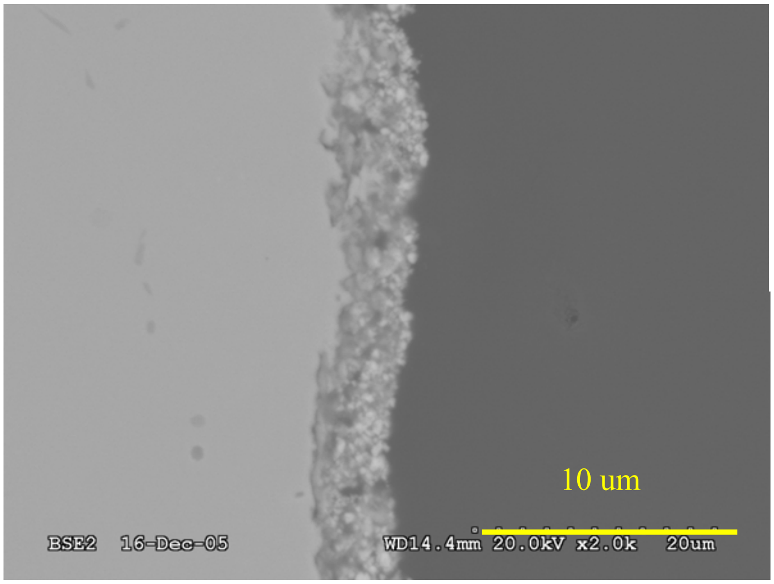

Edgewise micrograph

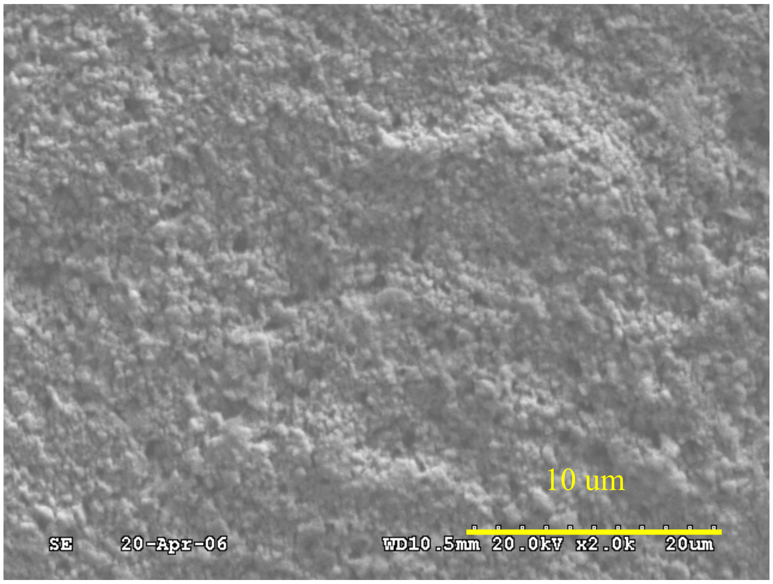

Surface micrograph

Fig. 2.27: SEM micrographs of dip-coated SS430 foils with LSM0.85 coating, annealed at 1000^0C for 2 hours in air and heat treated for 168 hours in air.

3. OXIDATION RESISTANT AND ELECTRICALLY CONDUCTIVE PEROVSKITE COATINGS THROUGH DEFECT CHEMISTRY FOR ANODE SIDE

3.1 Introduction

LTM is interconnect coating material for cathode side. This material is not suitable for anode side, as the oxygen partial pressure is very low (around 10^{-21}atm). In this type of extreme reducing condition very few materials survive. Materials with very low dissociation oxygen partial pressure are required for this application. And certainly, one of the best candidate materials for this application is $LaCrO_3$.

$LaCrO_3$ doped with Sr, Ca, and Mg has been widely studied as interconnect material [36,37], but criterion for selection has always been good electronic conductivity, but not the low oxygen ion conductivity. Moreover, doping $LaCrO_3$ by divalent ions like Sr, Ca, and Mg increases its oxygen ion conductivity. To avoid that, we adopted approach of doping $LaCrO_3$ by higher valent ion, Nb. Based on the hypothesis mentioned in the previous section, it can be claimed that the oxygen vacancy concentration goes down when $LaCrO_3$ is doped with higher valent ion. In other words, oxygen ion conductivity decreases with Nb doping on $LaCrO_3$.

$LaCr_{0.9}Nb_{0.1}O_3$ (LNC) was the chosen material. To prove the validity of the hypothesis, $LaCrO_3$ (LC) was also investigated. LNC was synthesized by solid state route. And the substrate selected was Haynes 230, which was also selected for previous study of LTM coating. Both perovskite ceramics were deposited on H230 metal foil, followed by oxidation in reducing atmosphere.

3.2 Experimental

3.3.1 Synthesis, Characterization, and Sputtering of ceramic coating materials: Method adopted for the synthesis of LNC was the same solid state route method, which was used for synthesis of LTM. La_2O_3 (Alfa, 99.99% pure), Cr_2O_3 (Alfa, 99.99% pure), and Nb_2O_5 (Alfa, 99.99% pure) were mixed in appropriate amount and ball milled for 24 hours (using zirconia media, 0.25” dia). Powder was calcined at 1200^0C for 2 hours. Formation of single phase LNC was checked by carrying out X-ray analysis (Philips X’pert). A bar of dimension 45x10x3 mm^3 was pressed using calcined powder and sintered at 1550^0C for 6 hours in air. Density of the bar was measured using standard fluid immersion method. Also, the disc of dimensions 75mm diameter and 15mm thickness was pressed and sintered to use it as the target in sputtering set up. Disc was attached to copper backing plate using silver epoxy to provide strength. $LaCrO_3$ target disc was custom made from Praxair.

Electrical conductivity of LNC material was measured using D.C. four probe conductivity technique. Set up for measurement was the same as the one used for LTM characterization, as mentioned in the Section 2. Conductivity was measured in the temperature range of 500^0C to 800^0C by increasing the temperature in steps of 50^0C. The total conductivity of the sample was calculated from following equation:

$$\sigma_{total} = \frac{I}{V} \times \frac{L}{A}$$

where I is the constant current of magnitude 0.04 amps and V is the voltage drop measured across the inner probes. L is the distance between the inner probes (27 mm) and A is the cross sectional area of the bar sample (30 mm^2). Total conductivity was plotted as a function of temperature.

1 μm thick LNC and LC materials were deposited separately on the both sides of Haynes 230 foil (12x12 mm^2). A Denton-18 RF Sputtering system was used for deposition. The chamber was evacuated to $2x10^{-6}$ atmospheres. Adequately low chamber pressure was required to obtain dense and adherent coating on the foils. RF power of 150 watts was applied to obtain a sputtering rate of 60 A^0 /min.

3.2.1 Oxidation, and Characterization of oxidized samples:

The H230 foils, coated with LNC and LC were oxidized at 800^0C in reducing atmosphere for different time durations of 336, 504, 1080, and 2160 hours. 10% hydrogen gas cylinder was used to create reducing atmosphere. Hydrogen gas was passed through the water bath maintained at a temperature of 33^0C to obtain 5% H_2O in the gas mix. Pristine metal foils were also oxidized along with coated ones to compare the oxidation behavior of metallic interconnects with and without protective coatings.

After oxidation, sample surfaces were studied under scanning electron microscope (SEM, Hitachi S-3000N). Also, oxide scale thickness was measured by mounting pieces of these samples in the epoxy mold followed by polishing and conducting SEM analysis in backscattered mode (BSE). The thickness of oxide scale was measured at several locations and the mean value was calculated. This process was adopted due to the non-uniformity in oxide scale thickness along the length of the sample. Square of oxide scale thickness was plotted vs. time for uncoated foil to determine k_f of H230 alloy in reducing atmosphere, while oxide scale thickness vs. time was plotted for coated H230 to determine k_c of the coating. X-ray diffraction analysis was conducted on the oxidized samples to examine the phases of oxides that are formed.

3.2.2 Area specific resistance (ASR):

Areas specific resistance of the coated and uncoated H230 foils was conducted using the same set up mentioned in chapter 2. ASR of oxide accumulated on H230 was plotted vs. temperature for samples oxidized for 336 hours.

3.3 Results and Discussion

3.3.1 Synthesis, Characterization, and Sputtering of ceramic coating materials:

XRD pattern of LNC was observed to match with XRD pattern of LC as shown in the fig. 3.1. No extra peaks of Nb_2O_5 were observed. This indicates that Nb is completely dissolved in LN, forming 100% solid solution. Nb replaced Cr due to its ionic size proximity with Cr (Ionic radius of Cr = 0.616A^0 and Nb = 0.67A^0).

Plot of total conductivity vs. temperature for LNC material is shown in fig.3.2. LN is p-type conductor with negligible ionic conductivity. Therefore total conductivity of the material can be considered as electronic conductivity. When it is doped with donor ion such as Nb, its ionic and electronic conductivities decrease as mentioned in chapter 2. The total conductivity (or electronic conductivity) of LNC at 800^{0}C is 0.07S/cm, which is smaller than that of LC or LC doped with acceptor ion such as Ca, Sr [38]. This is in accord with the theoretical predictions made in chapter 2. In case of LTM, the total conductivity is 48 S/cm at 800^{0}C, which contributes to the ASR of 2x10^{-6}Ωcm^2 for 1μm of coating. This value is too low to consider. Similarly, ASR value of LNC would be 1x10^{-3} Ωcm^2 for 1μm of LNC coating, which is also small. In LTM, even if the thickness of coating was increased, there would not be any significant increase in ASR of the coating; but in case of LNC material, change in coating thickness can enhance the ASR value significantly. As long as we are in the range of 1 μm thick coating, even LNC should not cause the problem. But definitely, thick coating application of LNC material is not the option.

3.3.2 Oxidation and Characterization of oxidized samples:

Fig.3.3a and fig.3.3b show the x-ray pattern of uncoated and coated H230 alloy foils with 1μm thick LNC, oxidized in reducing atmosphere at 800^{0}C for 504 hours. Cr_2O_3 and $Mn_{1.5}Cr_{1.5}O_4$ are the oxide products, Cr_2O_3 being the predominant oxide phase. This indicates that the oxide formation on H230 metal foil is same in both reducing and oxidizing atmosphere. The reason being the equilibrium p_{O_2} for Cr_2O_3 and $Mn_{1.5}Cr_{1.5}O_4$ formation is 10^{-28} and 10^{-30} atm. respectively [39-42]. Fig.3.4 shows the edgewise SEM micrographs of the uncoated H230 foils and foils coated with 1 μm of LC, and LNC oxidized in reducing atmosphere at 800^{0}C for 2160 hours. It is clear from the micrographs that the oxide forms underneath the coating. Uncoated H230 foil formed the thickest oxide scale of 3.18 μm followed by foils coated with LC and LNC. Foils coated with LNC formed the thinnest oxide scale of 0.94 μm. The reason for this was the suppression of oxygen vacancies by higher valence (donor) ion doping on Cr site of LC as discussed in theoretical background section 2.2.

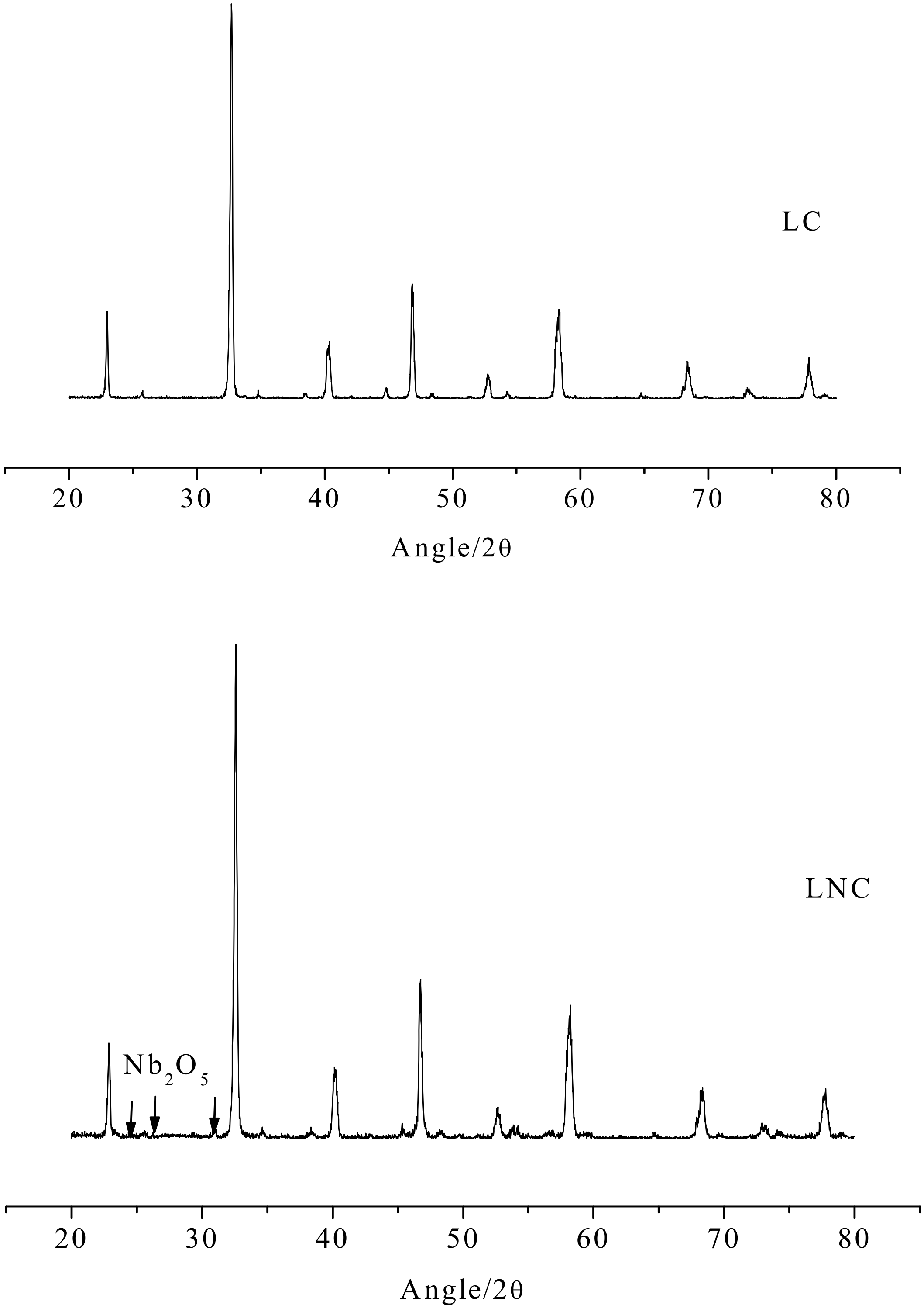

Fig.3.1: XRD patterns of LC, and LNC

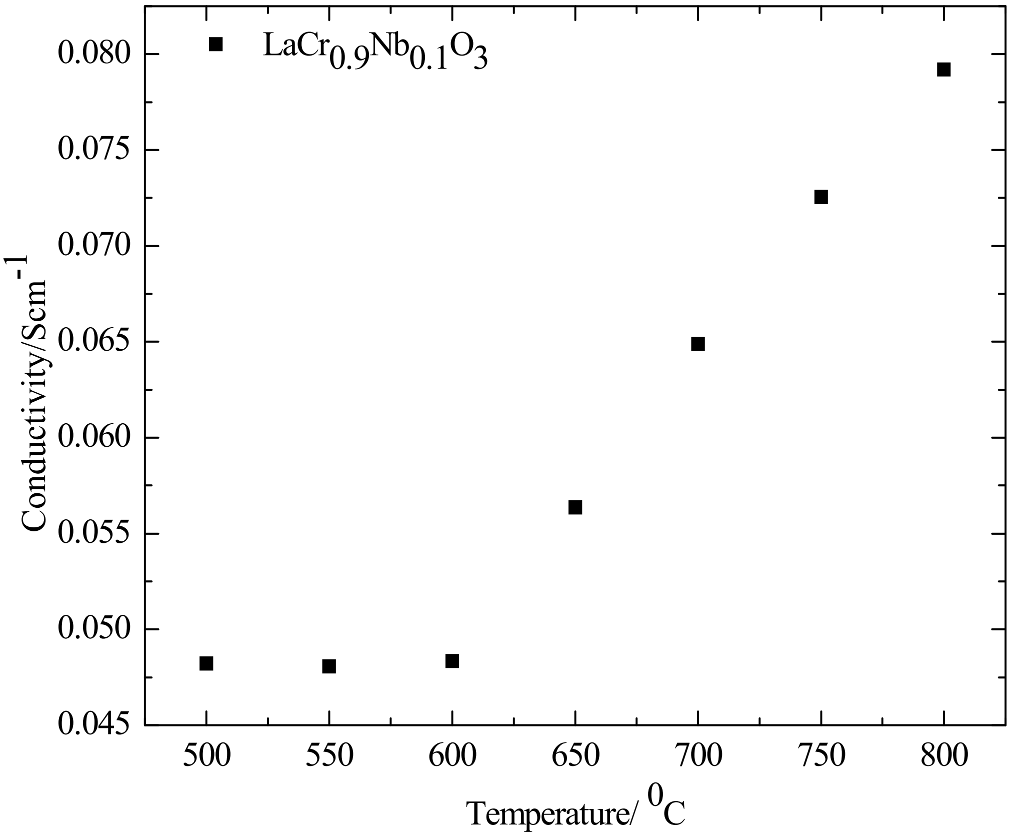

Fig. 3.2: Total conductivity vs. temperature for LNC

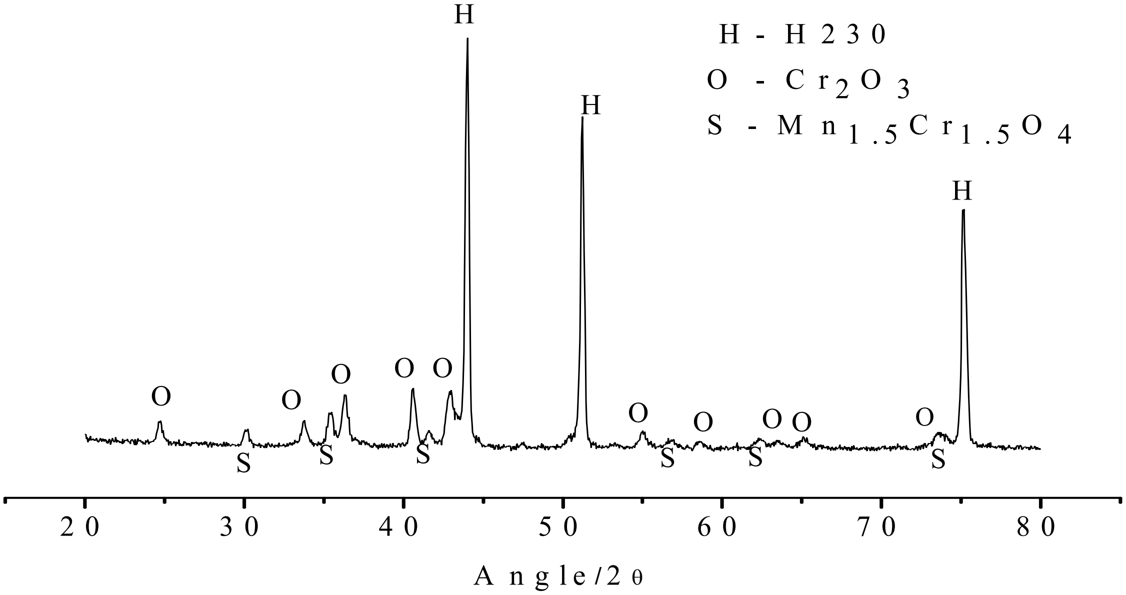

Fig. 3.3a: An XRD pattern of uncoated H230 foil oxidized for 504 hrs in reducing atmosphere at 800°C.

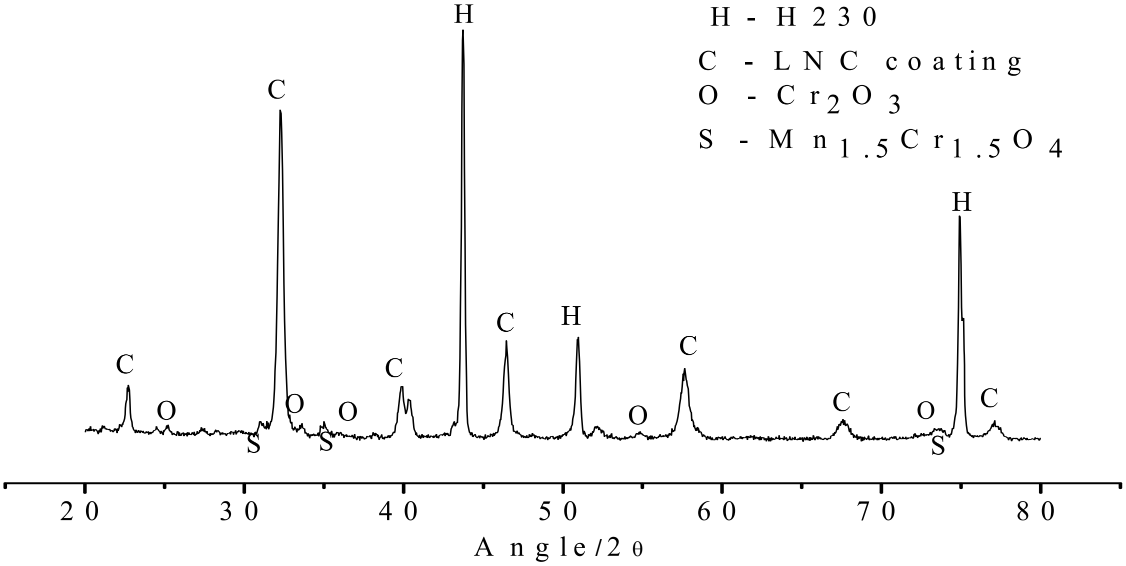

Fig. 3.3b: An XRD pattern of H230 foil coated with 1 μm of LNC oxidized for 504 hrs in reducing atmosphere at 800°C.

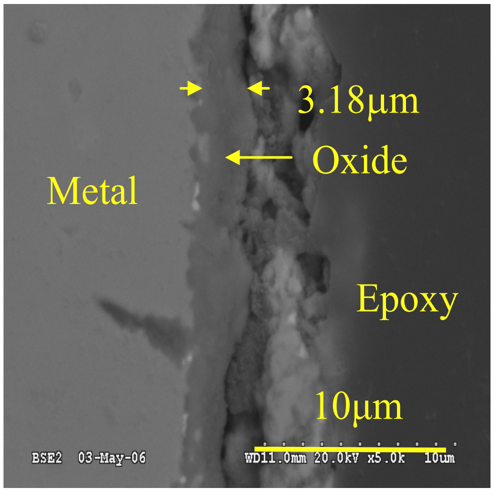

Uncoated H230

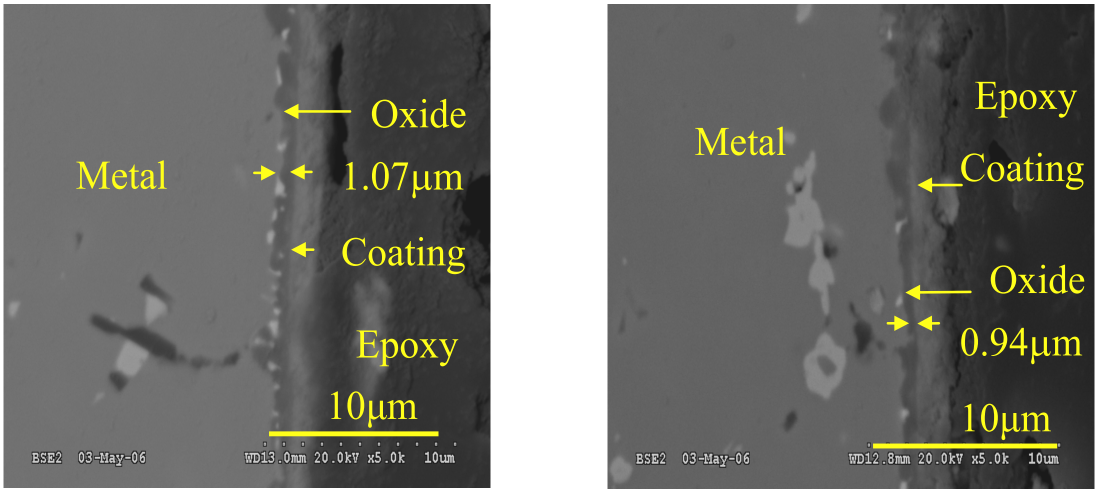

H230 coated with 1µm
LC

H230 coated with 1µm
LNC

Fig. 3.4: SEM micrographs (edgewise) of uncoated, LC-coated (1 µm) and LNC-coated (1 µm) H230 foils oxidized for 2160 hrs in reducing atmosphere at 800^{o}C.

3.3.3 Kinetics of oxidation :

Fig.3.5 shows the plot of square of oxide scale thickness vs. time of oxidation for H230 uncoated foils. The slope of the graph gives the values of k_f i.e. parabolic rate constants in reducing atmosphere, which is equal to 1.34x10^{-14}cm^2/s. This value is higher than the k_f of H230 in air. Same trend was observed by D. England et al. [43].

Fig.3.6 shows plot of oxide scale thickness vs time of oxidation for H230 foil coated with 1μm thick coating of LC, and LNC. The growth of the oxide layer vs time can be expressed by the equation (2.4) (or equation (2.1)) i.e.

$$x_f = \frac{\sqrt{\left(k_f^2 x_c^2 + k_f k_c^2 t\right)} - k_f x_c}{k_c}$$

The values of k_c i.e. kinetic parameter for oxygen permeation through the coating may be obtained by fitting the parabolic equation (2.4) through the experimentally obtained data points in fig.3.6 (k_f = 1.34x10^{-14}cm^2/s is considered while fitting the curve). From the best fit to the data points, corresponding values of k_c for different coating materials were estimated. The values are: k_c for LC =3.24x10^{-15}cm^2/s, and k_c for LNC = 2.64x10^{-15}cm^2/s. These results are in accord with defect chemistry. Comparison of all interconnect coating materials studied is given in fig.3.7

Oxygen flux reaching the metal foil through the coating is given by fick's first law,

$$J_{O_2} = D_v \times \frac{\partial c}{\partial x} \tag{3.1}$$

where, D_v is the diffusion coefficient of oxygen vacancies through the coating, and $\frac{\partial c}{\partial x}$ is the oxygen concentration (or pressure) gradient across the coating. I. Yasuda et al. studied the diffusion coefficient of oxygen vacancies through LSM20 (i.e. LM doped with 20 % Sr) and LCC20 (i.e. LC doped with 20% Ca) at 1000^{0}C; their respective values are 2.79x10^{-5}cm^2/s [44]and 7.94x10^{-6}cm^2/s [45]. Although these are not the exact materials that are undertaken in this study, they belong to the same families of materials under consideration. It is reasonable to assume almost same diffusivity values for materials under consideration. Thus, it can be claimed that vacancy diffusion coefficient in LNC, and LN is smaller than that of LTM, LM, and LSM.

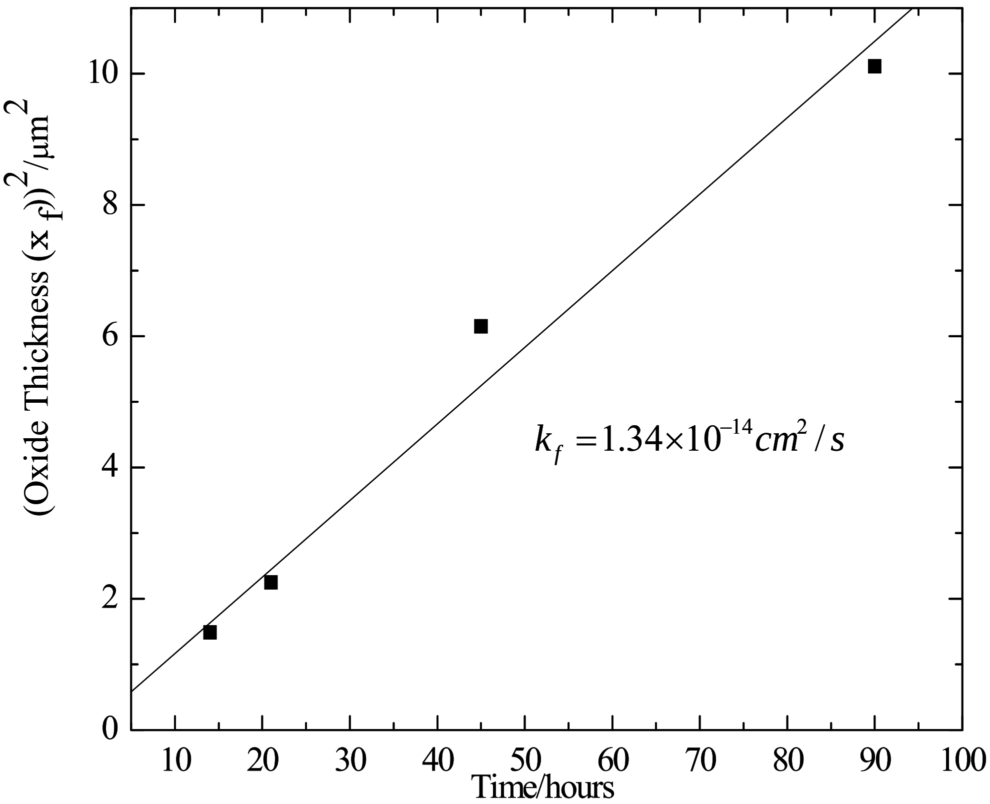

Fig.3.5: A plot of (oxide scale thickness)^2 vs. time of oxidation at 800°C for uncoated H230 foil in reducing atmosphere.

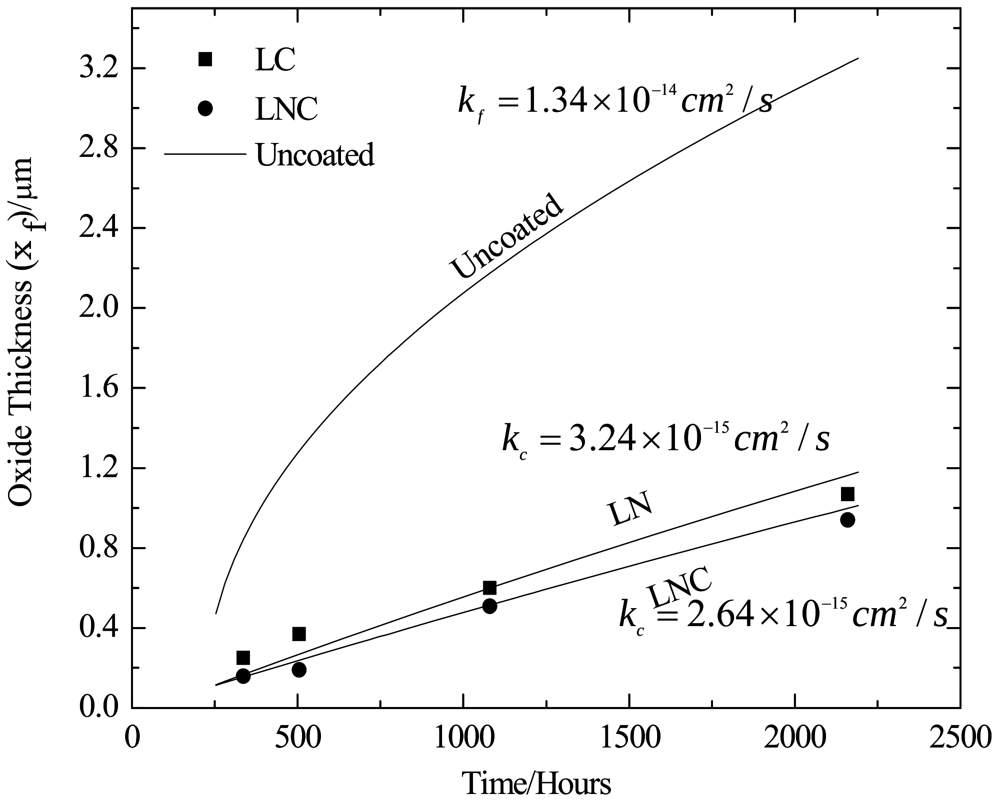

Fig. 3.6: Plots of oxide scale thickness vs. time of oxidation at 800°C for uncoated H230 and H230 with 1 μm coatings of LSM, LM and LTM. Lines through data points are fits to equation (2.4).

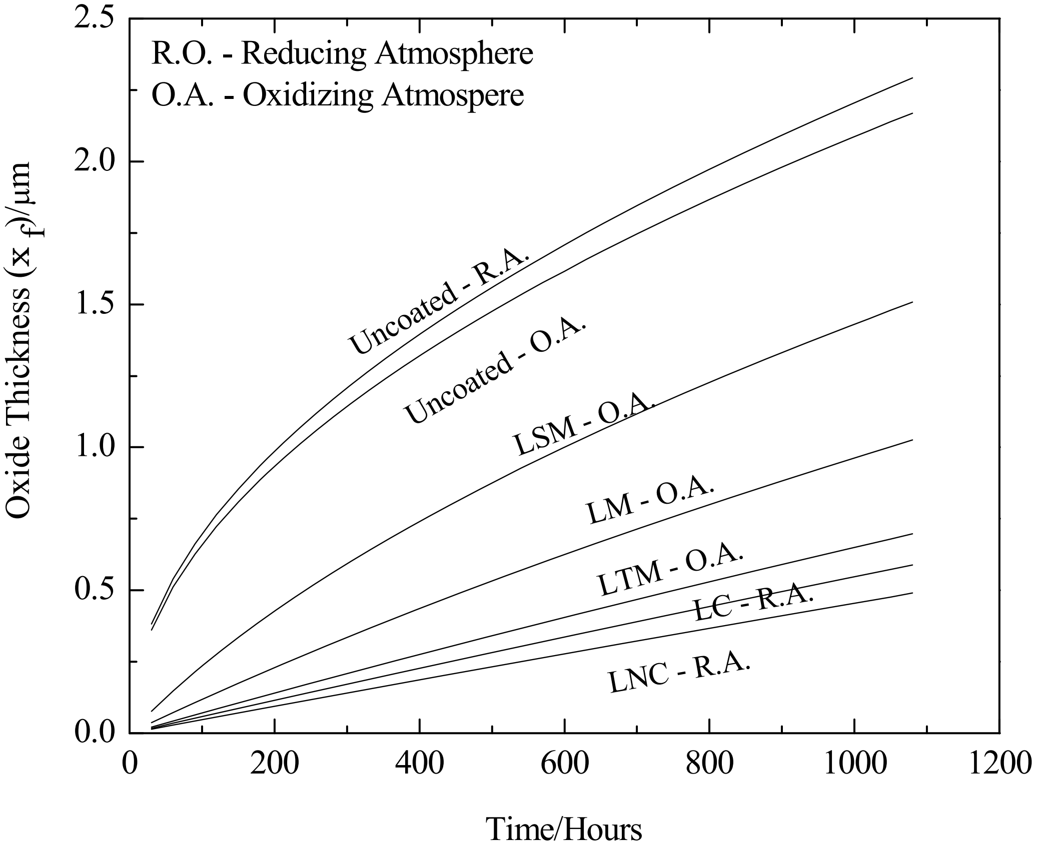

Fig.3.7 Plots of oxide scale thickness vs. time of oxidation at 800°C for uncoated H230 and H230 with 1 µm coatings of different coating materials in different environmental conditions.

This is the one reason for obtaining smaller value of k_c for LN, and LNC. Other reason being smaller pressure difference across the coating.

If only oxygen diffusivity through the coating was the criterion for selection of coating material, LNC would be better than LTM, as LNC's oxygen diffusivity is smaller than LTM's oxygen diffusivity. If electron conductivity was the criterion for selection of coating materials, LTM would be more appropriate choice. If both criteria were used to select the coating materials, LTM would be the definite choice for both cathodic and anodic side, because of very high electronic conductivity and reasonably low oxygen ion conductivity (although its oxygen ion conductivity is higher than LNC). But the principal difficulty in using LTM on anode side is its instability in reducing environment. LTM dissociates under reducing atmosphere forming dual phase which is highly resistive [46, 47]. This is the reason of using LNC material on anode side.

There could be the possibility of using LNC coating materials on both oxidizing and reducing sides, as it is stable over wide partial oxygen pressure, but its very low electronic conductivity is the major impediment. As mentioned before, its electronic conductivity is small but is adequate enough if coating thickness is from 1 to 5 μm. Above this thickness ohmic losses could be significant. And in our case thickness has to be in the range of 10 μm to effectively reduce the oxidation kinetics. (This is not the case with LTM, even if the thickness of coating exceeds 10 μm, it does not contribute to any ohmic losses.) Analyzing all the situation, it is advisable to use thick LTM coating (around 5 to 10μm) on cathode side and thin LNC coating (around 1 to 5μm) on the anode side to get optimum result.

3.3.4 Area Specific Resistance (ASR):

Fig. 3.8 shows ASR vs. temperature plots for uncoated H230 foil, and H230 foils with 1 μm coatings of LNC and LC, oxidized in reducing atmosphere for 336 hours at 800^{o}C. The ASR was the highest for uncoated foil and the lowest for LNC-coated foil, with the LN-coated foil exhibiting intermediate behavior. These results further support the hypothesis concerning the role of defect chemistry of the coating material in determining oxidation kinetics of coated foils. In Fig. 3.7, the ASR data are plotted on an Arrhenius graph. The lowest ASR value at 800^{o}C, 0.015 Ωcm^2, was obtained for H230 foil with 1 μm coating of LNC oxidized for 336 hours. The ASR for the LC-coated sample is ~0.04 Ωcm^2.

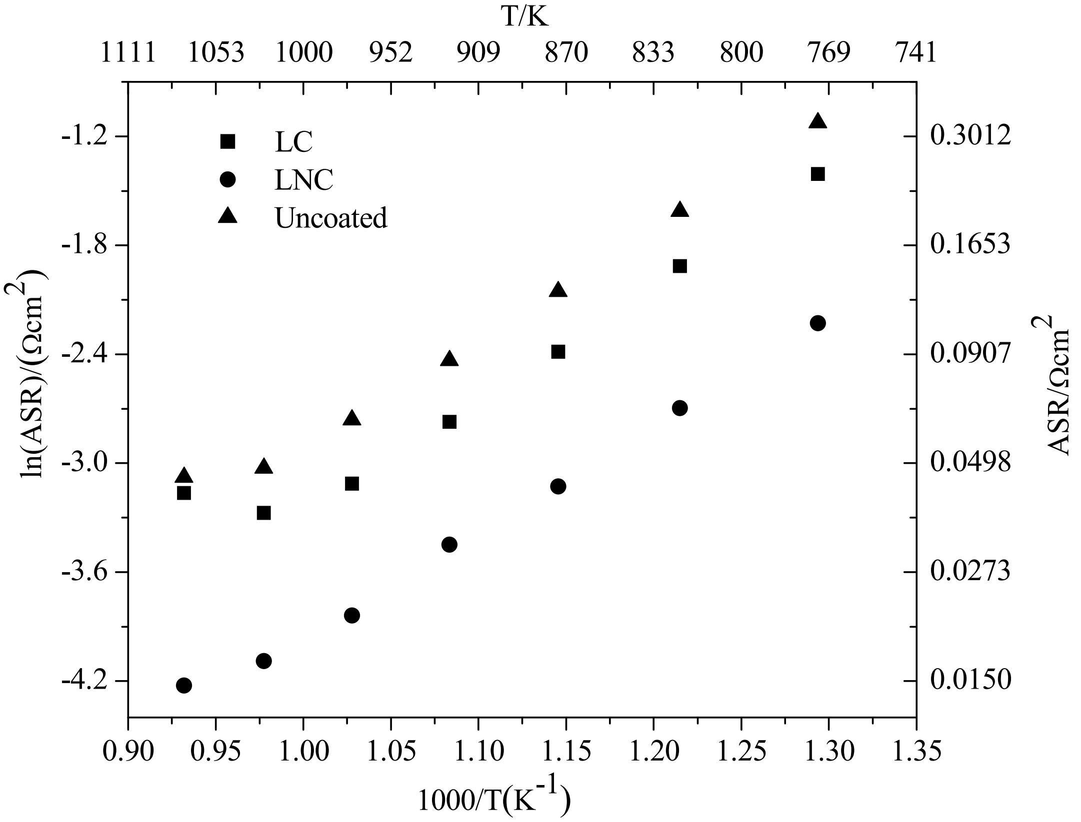

Fig. 3.8: Plots of ASR vs. 1000/T for uncoated and coated H230 metal foils with 1 μm coatings of LNC and LN, oxidized in reducing atmosphere at 800°C for 336 hours.

4. MEASUREMENT OF OXYGEN ION CONDUCTIVITY IN PREDOMINANTLY ELECTRONIC CONDUCTOR USING ELECTRON BLOCKING ELECTRODE TECHNIQUES.

4.1 Introduction

Measurement of oxygen ion/electron conductivity of mixed ion conductors by electron blocking/ion blocking electrode technique is a routine method. Publications by I. Riess [48-51] and W. Worrel [52] discuss these techniques in details. This method is called Hebb-Wagner polarization method. Fig. 4.1 depicts the schematic diagram of ion blocking electrode cell to measure the electronic conductivity of MIEC (Mixed Ionic Electronic Conductor). Consider MIEC consists of metal oxide MO, which is electron (e^-) and cation (M^+) conductor. Electrode R on the left hand side is a reversible electrode (M^+ and e^- both can flow through the electrode) while electrode C on right hand side is an ion blocking electrode (only electrons can flow through this electrode). When current is passed through the circuit, the following reaction takes place:

$$M_{(R)} \rightarrow M^+ + e^-$$

where is M is elemental metal. M^+ ions flow through MIEC but are blocked at blocking electrode C. Electrons can complete the circuit by passing through electrode C. Thus whatever voltage drop results across MIEC, is due to passage of electrons and value of electron conductivity can be calculated. Similarly, ionic conductivity of the MIEC can be measured by blocking the passage of electrons (this can be done by using an electron blocking electrode instead of an ion blocking electrode). In our case, the latter principle was used to measure ionic conductivity of the material, but our samples were predominantly electronic conductors and exhibited very low ionic conductivity. In other words, we tried to measure the ionic conductivity values of predominantly electronic conductors.

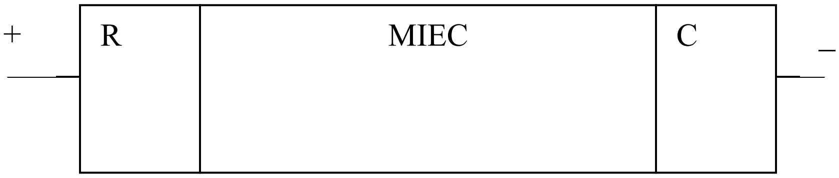

Fig. 4.1: Hebb-Wagner polarization measuring cell.

In section 2, the dependence of k_c (the kinetic parameter of oxygen permeation through the LSM, LM, and LTM) on composition and defect chemistry was established. Oxygen permeation through LTM was the lowest while through LSM was the highest, LM exhibiting intermediate value. In this chapter, the oxygen ion conductivity of these materials was measured using Hebb-Wagner polarization method by blocking electronic conductivity of materials using 8-YSZ electrodes. Different cell configurations were used for Hebb-Wagner polarization method, which will be discussed in section 4.3.

4.2 Theoretical background

Fig. 4.2a depicts the simple configuration of electron blocking electrode cell (for simplicity only one electron blocking electrode is assumed). Fig. 4b shows the voltage and chemical potential profile across the sample. MO electrode represents the LM/LSM/LTM in our case, which is p-type conductor and exhibits very low oxygen ion conductivity (this material is treated as mixed conductor). The second electrode is YSZ, which exhibits very high oxygen ion conductivity and negligible electrical conductivity. Critical condition for blocking of the electrons in this cell configuration is $\sigma_e^{YSZ} << \sigma_i^{Sample}$ [4], where σ_e^{YSZ} is electrical conductivity of YSZ and σ_i^{Sample} is oxygen ion conductivity of sample (LSM/LM/LTM). From work by Pal [53], it can be concluded that electronic conductivity of YSZ is below 10^{-10} S/cm. Platinum (porous) electrodes are applied on both sides of the cell. The partial pressure of oxygen is maintained constant at both electrodes and constant D.C. voltage is applied.

Now,

$$I_t = I_e + I_i \tag{4.1}$$

where I_t is total current density, I_e is electrical current density, and I_i is oxygen ion current density. In steady state change in current density is zero.

$$\nabla I_t = 0 \qquad \nabla I_e = 0 \qquad \nabla I_i = 0 \tag{4.2}$$

That is, the ionic and electrical currents are uniform throughout the cell. Now, the electrical current in YSZ is nearly zero, thus the electrical current in MO must be zero even though $\sigma_e^{MO} \neq 0$. Now,

$$I_e = \frac{\sigma_e^{MO}}{e} \nabla \eta_e^{MO} = 0 \tag{4.3}$$

$$I_e = \frac{\sigma_e^{MO}}{e} \left\{ \nabla \mu_e^{MO} - e \nabla \phi^{MO} \right\} = 0 \tag{4.4}$$

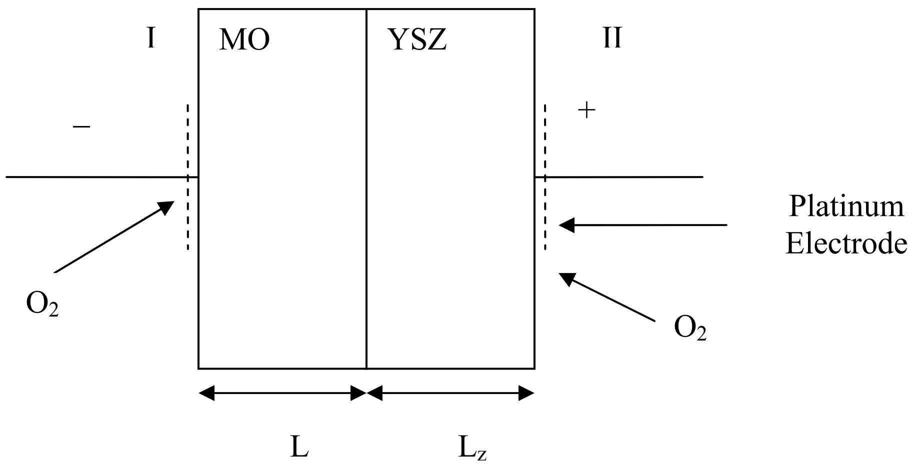

Fig. 4.2a: Electron blocking cell assembly for Hebb-Wagner polarization measurements

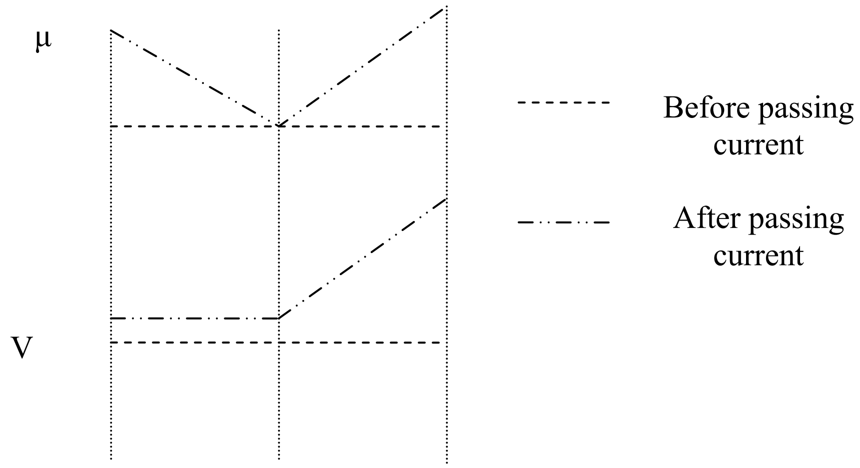

Fig. 4.2b: Profile of voltage and chemical potential of oxygen across the cell.

where σ_e^{MO} is electrical conductivity of MO, $\nabla \eta_e^{MO}$ is change in electrochemical potential of electrons across MO, $\nabla \mu_e^{MO}$ is change in chemical potential of electrons across MO, and $\nabla \phi^{MO}$ is change in electrostatic potential across MO.

As $\sigma_e^{MO} \neq 0$, $\nabla \eta_e^{MO}$ has to be equal to zero. $\nabla \mu_e^{MO} = 0$ since μ_e will equilibrate between the platinum electrode and the MO pellet. Thus, $\nabla \phi^{MO} = 0$ in MO. That is, the entire voltage will drop across YSZ as shown in fig. 4b.

Now, $$I_t = \frac{\sigma_t^{MO}}{e} \nabla \eta_e^{MO} + \frac{\sigma_i^{MO}}{4e} \nabla \mu_{O_2}^{MO} \tag{4.5}$$

$$I_t = 0 + \frac{\sigma_i^{MO}}{4e} \nabla \mu_{O_2}^{MO} = I_i \tag{4.6}$$

Now, $$\nabla \mu_{O_2}^{MO} = \frac{\mu_{O_2(Interface)} - \mu_{O_2}^{I}}{L} \tag{4.7}$$

$$\therefore I_i = \frac{\sigma_i^{MO}}{4e} \frac{\left(\mu_{O_2(Interface)} - \mu_{O_2}^{I}\right)}{L} \tag{4.8}$$

where σ_t^{MO} is total conductivity of MO, σ_i^{MO} is oxygen ion conductivity of MO, $\nabla \mu_{O_2}^{MO}$ is change in chemical potential of oxygen across MO pellet, $\mu_{O_2(Interface)}$ is chemical potential of oxygen at interface, $\mu_{O_2}^{I}$ is chemical potential of oxygen on side I, and L is the length of MO pellet.

For Zirconia (YSZ)

$$I_t = \frac{\sigma_t^{Z}}{e} \nabla \eta_e^{Z} + \frac{\sigma_i^{Z}}{4e} \nabla \mu_{O_2}^{Z} \tag{4.9}$$

where σ_t^{Z} is total conductivity of YSZ, $\nabla \eta_e^{Z}$ is change in electrochemical potential of electrons across YSZ, $\nabla \mu_{O_2}^{Z}$ is change in chemical potential of oxygen across YSZ, and σ_i^{Z} is ionic conductivity of YSZ. But $\sigma_e^{Z} = 0$, therefore $\sigma_t^{Z} = \sigma_i^{Z}$

$$\therefore I_t = \frac{\sigma_i^Z}{e}\nabla\eta_e^Z + \frac{\sigma_i^Z}{4e}\nabla\mu_{O_2}^Z \tag{4.10}$$

Again, it is assumed that μ_e is equilibrated across YSZ.

$$\nabla\eta_e^Z = \nabla\mu_e^Z - e\nabla\phi^Z = e\nabla\phi^Z \tag{4.11}$$

$$I_t = -\sigma_i^Z\nabla\phi^Z + \frac{\sigma_i^Z}{4e}\nabla\mu_{O_2}^Z = I_i \tag{4.12}$$

$$I_t = -\sigma_i^Z\frac{\left(\phi_{II} - \phi_{Interface}\right)}{L_Z} + \frac{\sigma_i^Z}{4e}\frac{\left(\mu_{O_2}^{II} - \mu_{O_2(Interface)}\right)}{L_Z} = I_i \tag{4.13}$$

Now, $\phi_{II} - \phi_{Interface}$ is the applied voltage V, $\mu_{O_2}^{II}$ is the chemical potential of oxygen at side II, and L_Z is the length of YSZ pellet. In the above equation everything except $\mu_{O_2(Interface)}$ is known. Solving equations (4.13) and (4.8):

$$I_t = -\frac{\sigma_i^{MO}}{4e}\left\{\frac{\frac{L_Z 4eI_t}{\sigma_i^Z} + 4eV}{L}\right\} \tag{4.14}$$

$$I_t = -\frac{\sigma_i^{MO}}{\sigma_i^Z}\frac{L_Z}{L}I_t - \frac{\sigma_i^{MO}}{L}V \tag{4.15}$$

In our case, $\sigma_i^Z \gg \sigma_i^{MO}$

$$\therefore I_t = -\frac{\sigma_i^{MO}V}{L} \tag{4.16}$$

$$\therefore \sigma_i^{MO} = \frac{I_t L}{V} \qquad \text{(Magnitude only)} \tag{4.17}$$

Thus, using this approach, ionic conductivity of MO i.e. LSM, LM, and LTM can be determined. This is called blocking electrode technique.

4.3 Experimental

4.3.1 Co-pressed cell:

Circular three layered sandwich structure of 8-YSZ, LSM/LM/LTM, and 8-YSZ was co-pressed followed by cold isostatic pressing. Sandwich structure was co-sintered at 1400^0C for two hours. Very slow heat treatment cycle of 1^0/min was used because of difference in thermal expansion coefficient of the materials. Values of thickness of 8YSZ and LSM/LM/LTM after sintering were 2 mm and 1 mm respectively. Circular platinum electrodes of 10 mm diameter were coated on both sides of the cell using platinum paste followed by curing at 1000^0C for one hour. After curing, two electrodes were connected to silver wires with the help of fine silver mesh (mesh was used to increase the contact surface area. The cell was placed in spring loading apparatus and two honeycomb structures were placed on either side of the cell for exerting pressure to ensure proper contact between silver mesh and platinum electrodes. The schematic of complete assembly is shown in fig 4.3. This assembly was placed in the furnace and heated to 800^0C. Silver wires from either side of the electrodes were

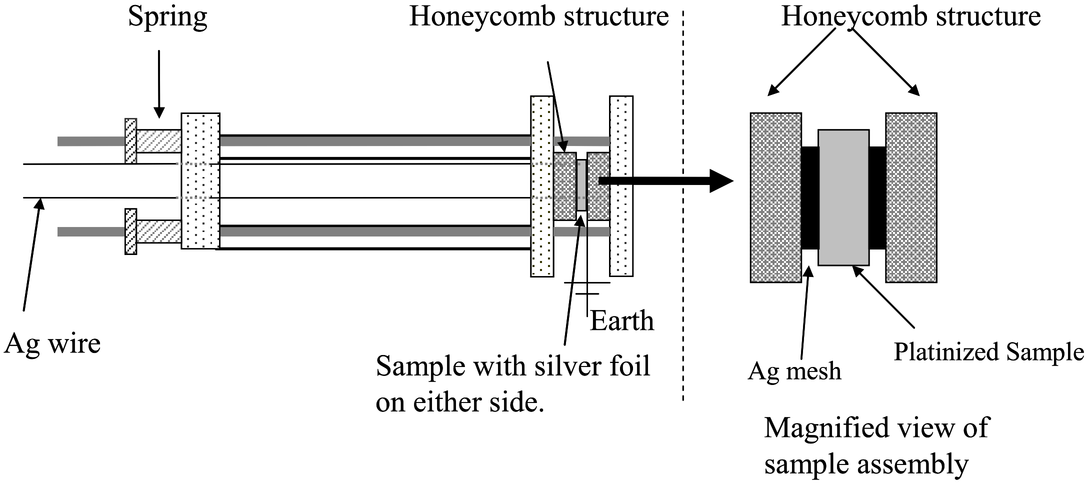

Fig. 4.3: Spring loading assembly for Hebb-Wagner polarization measurements.

connected to the voltage probes and current probes. Solartron instrument was used to supply current of $5x10^{-5}$amp. Very low magnitude of current was selected because of very high resistance of the sample. Voltage data points were acquired using Corrware software as a function of time. This experiment was conducted for long time duration (one to two days) to ensure stabilization of the sample. As the diffusivity of oxygen ions through the sample is very low, it takes long time to obtain steady state condition. Fig. 4.4 shows the schematic of the cell design.

4.3.2 Co-pressed cell with guard electrode:

Because of very high resistivity of the sample, there is possibility of electrons traveling through low resistant path i.e. surface of the sample. To avoid the surface conductivity of the sample, third electrode called guard electrode was introduced in design of the cell. Fig. 4.5 shows the cell design. Guard electrode is nothing but ring of platinum paste at the circumference of the cell, both sides of the sample. This third electrode was connected to the earth, so that voltage drop across sample is due to the resistance of bulk of the sample and not due to its surface resistance.

4.3.3 PVD sputtered cell:

As the ionic conductivity of LSM/LM/LTM samples is very low, thickness of the sample plays important role in obtaining steady state condition. To reduce the stabilization time and obtain steady state in lesser time, the sample thickness was reduced to the scale of microns. This was done by sputtering the LSM/LM/LTM material on thin YSZ disc. Thickness of the sputtered material was 1.5 μm. Electroding and earthing was done as explained earlier. Fig. 4.6 shows the schematic diagram of the cell design.

4.3.4 Tapecast cells:

In the above case, PVD sputtered coating was not very strong. To overcome this limitation, tapes of 8-YSZ and LSM/LM/LTM were prepared by tapecasting technique and sandwich structure as mentioned in 4.2.1 was made by laminating the tapes together. Cell structure was bisque fired followed by sintering at 1400^0C for 2 hours. Same procedure was followed for measurements as explained in 4.3.2. Fig. 4.7 shows the schematic diagram of the cell design.

4.4 Results and Discussion

In first case of co-pressed cell structure, conductivity values obtained for LSM, LM, and LTM are as shown in table 4.I, which are in the range of 10^{-5}S/cm. This value of conductivity is very high for these materials. As per our hypothesis, LTM should exhibit the lowest oxygen ion conductivity whereas LSM should exhibit the highest. But obtained conductivity value of LSM is lower than LM, which is contradictory to our hypothesis. The only reason that explains this ambiguity is the surface conductivity across the sample. As resistance of sample is very high, electrons would flow through the least resistant path i.e. surface of the sample. And recorded value would consist of

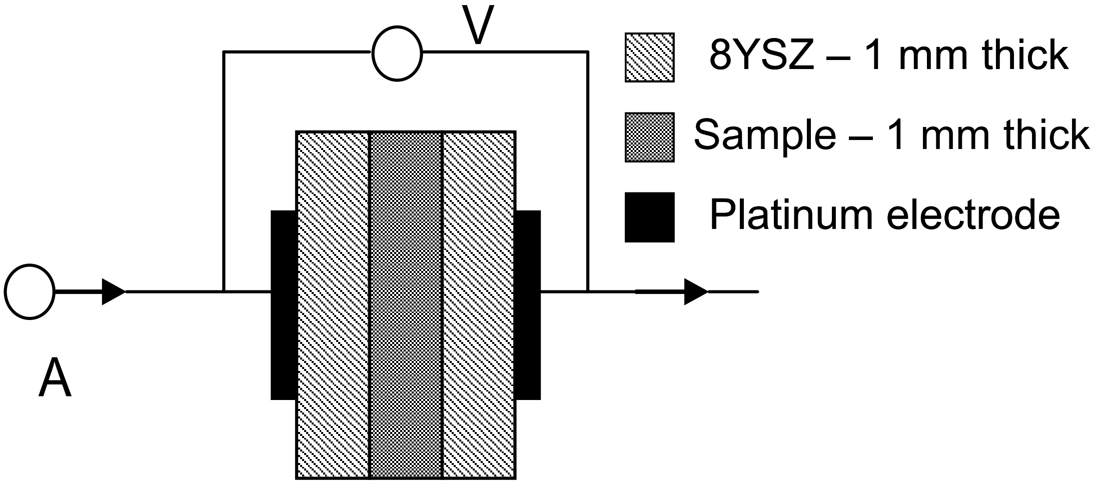

Fig. 4.4: Co-pressed sandwich structure for Hebb-Wagner polarization measurement

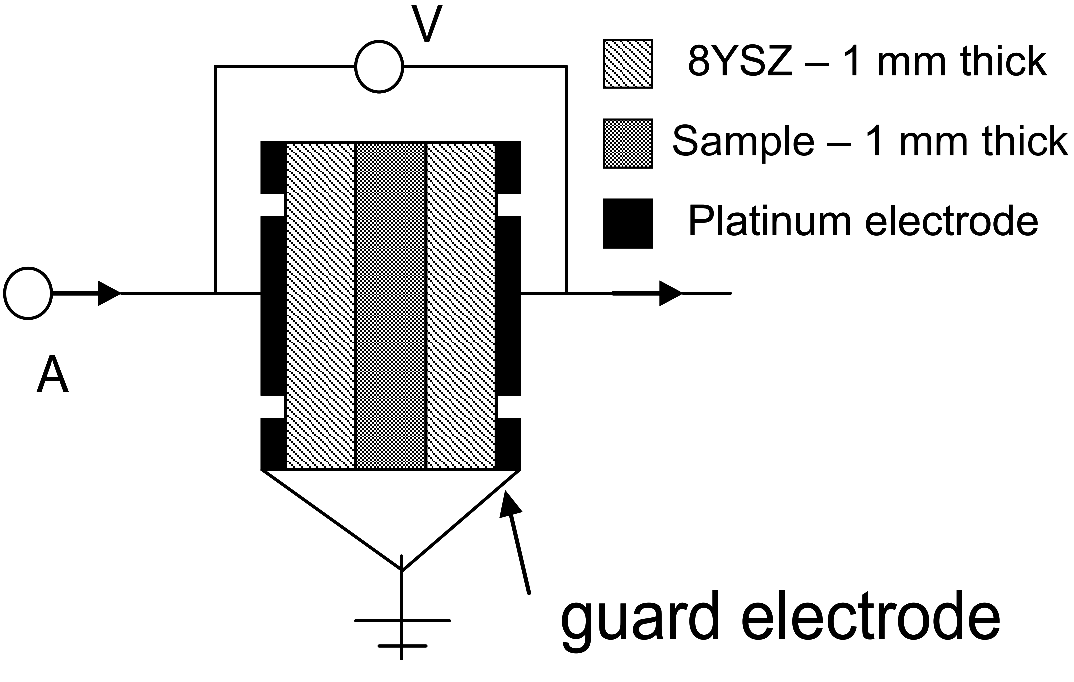

Fig. 4.5: Co-pressed sandwich structure with guard electrode for Hebb-Wagner polarization measurement

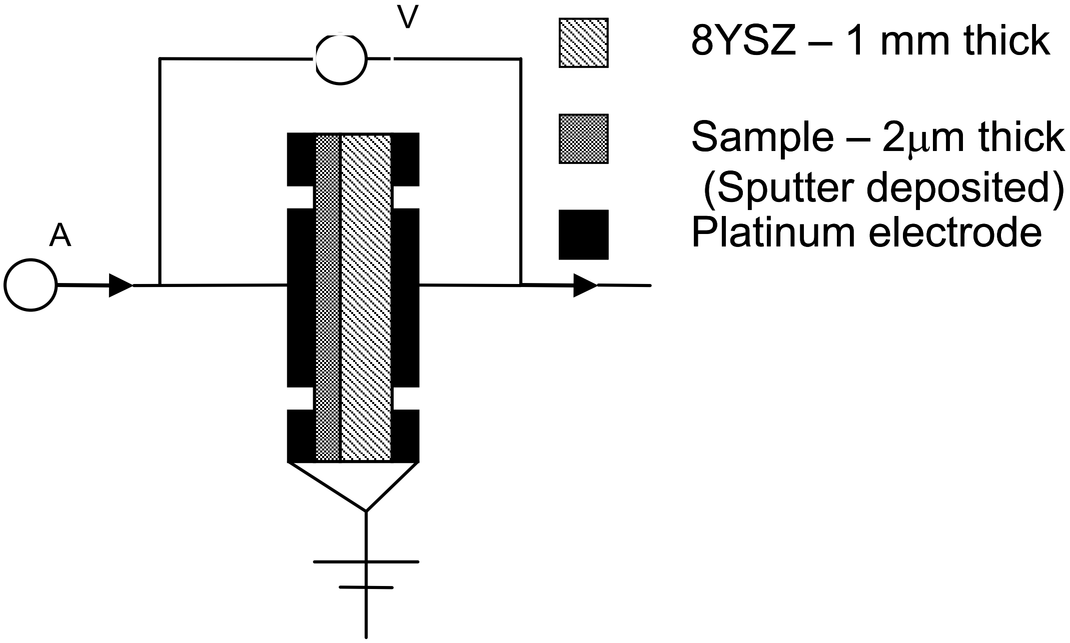

Fig. 4.6: Sputter deposited couple for Hebb-Wagner polarization measurement

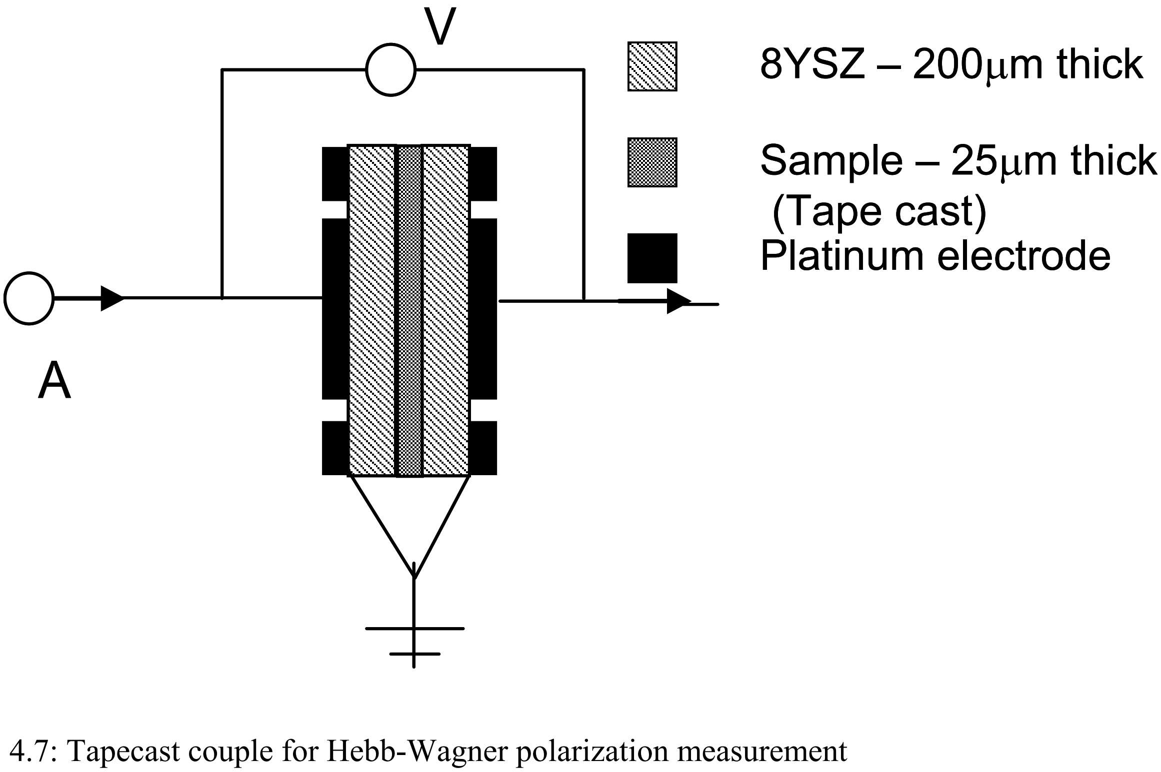

Fig. 4.7: Tapecast couple for Hebb-Wagner polarization measurement

resistance of bulk sample as well as surface resistance in parallel. To overcome this limitation, guard electrode was introduced in the cell design as explained in the previous section. This guard electrode was connected to the earth so that the conductivity value obtained would be contributed by the voltage drop across bulk material only. Table 4.II shows the ionic conductivity values of coating materials. In this case, conductivity values are recorded in the range of 10^{-6} S/cm. This improvement (decrease in conductivity values) is solely because of suppression of surface conductivity. Also, as per our hypothesis, LTM exhibited the lowest value of conductivity while LSM exhibited the highest. Fig. 4.8 shows the plot of voltage drop across sample vs. time, which is a representative graph of the above two cases. Even after 24 hours sample did not stabilize, which is an indication of slow diffusion rate of oxygen vacancies in the coating materials [54,55]. This could be overcome by reducing the thickness of sample, which was achieved by sputtering 1μm thick LSM/LM/LTM on 1mm thick YSZ. Improvement in stabilization time was observed after reducing the thickness of sample as shown in table 4.III and the conductivity values decreased by one order to 10^{-7} S/cm. But sputter-deposited coating was too thin, some micro-cracks were observed after measurement at 800^0C. To confirm the results, new design of cell using tapecast technique was adopted. Table 4.IV shows the oxygen ion conductivity values for tapecast cell design that are also in the range of 10^{-7} S/cm. Fig. 4.8 shows the plot of voltage vs. time, which is representative graph for above two designs, and it was observed that stabilization time drastically decreased. In former two cases conductivity values were recorded in non-steady state, while in latter two cases they were recorded in almost steady state. Thus, conductivity values obtained in latter two designs are more accurate than obtained in former two designs. There is no experimental data about ionic conductivity of LM and LSM. But paper by I. Yasuda et al [56] discusses the theoretical calculations of ionic conductivity of these materials, which match our results.

Table 4.I

Oxide	LTM	LM	LSM
Conductivity(S/cm)	1.24×10^{-5}	8.48×10^{-5}	7.45×10^{-5}

Table 4.II

Oxide	LTM	LM	LSM
Conductivity(S/cm)	5.9×10^{-6}	9×10^{-6}	2.1×10^{-5}

Table 4.III

Oxide	LTM	LM	LSM
Conductivity(S/cm)	2.0×10^{-7}	2.3×10^{-7}	4.5×10^{-7}

Table 4.IV

Oxide	LTM	LM	LSM
Conductivity(S/cm)	4.2×10^{-7}	7.4×10^{-7}	9.1×10^{-7}

CONCLUSIONS:

Based on this work, the following conclusions are drawn.

1) Of the materials studied, the Sr-doped $LaMnO_3$ (LSM) exhibited the highest total conductivity (which is mainly electronic), undoped $LaMnO_3$ (LM) exhibited intermediate conductivity, and Ti-doped $LaMnO_3$ (LTM) exhibited the lowest conductivity, in accord with expectations based on defect chemistry. An important point is that still the electronic conductivity of LTM, which is ~48 S/cm at 800°C, is more than adequate for application as a coating material for SOFC interconnect.
2) Oxidation studies on uncoated H230/INC718 and H230/IN718 with 1 micron thick coatings of LSM, LM, and LTM were conducted in air for up to 1080 hours at 800°C. Uncoated samples exhibited the largest oxide scale thickness (~2.2 microns in case of H230 and 4.9 microns in case of INC718), followed by LSM-coated, LM-coated, with the LTM-coated showing the smallest oxide scale thickness of ~0.64 microns in case of H230 and 1.93 microns in case of INC718 . The lowest oxide scale thickness for LTM-coated H230 suggests than LTM exhibits the lowest oxygen ion conductivity of the materials studied here, in accord with defect chemistry.
3) The kinetic parameter, k_c, which governs transport through coating and thereby dictates its protectiveness against oxidation was the lowest for LTM ($k_c \approx 3.96\times10^{-15}$ cm^2/s), intermediate for LM ($k_c \approx 7.1\times10^{-15}$ cm^2/s), and the highest for LSM ($k_c \approx 1.51\times10^{-14}$ cm^2/s) in case of H230 substrate, in accord with defect chemistry. While for INC718 substrate, values obtained were $k_c \approx 2.83\times10^{-14}$cm^2/s for LSM, $k_c \approx 2.14\times10^{-14}$cm^2/s for LM, and $k_c \approx 1.26\times10^{-14}$cm^2/s for LTM. (Difference in k_c values, for same coating material when deposited on different substrate, is because of some micro-cracks and spalling in coating). Thus, of the materials studied, LTM is the preferred coating material.
4) The area specific resistance (ASR) of the samples, which predominantly reflects the ASR of the oxide scale, was measured on uncoated and coated samples. The LTM-coated H230 exhibited the lowest ASR while the uncoated H230 exhibited the highest ASR, in accord with defect chemistry. Same is true for INC substrate. Some interdiffusion occurred between the coating and the oxide scale formed under the coating, and this effectively helped further lower the ASR of the LTM-coated samples. This shows that diffusion of cations which invariably occurs into the oxide scale (and also into the coating) during oxidation actually lowers its resistance and thus has a beneficial effect. Excessive interdiffusion, however, is undesirable.
5) The LTM coating developed in this work is expected to be satisfactory to ensure 40,000 hour service life of SOFC stack operated at 800°C, provided its thickness is about 15 microns. Further improvements in protective ability are deemed possible by optimization of the coating material composition through defect chemistry. If a $k_c \approx 1.0\times10^{-15}$ cm^2/s can be achieved, the required coating thickness to assure 40,000 hour life will be only about 5 microns. The projected

oxide scale thickness is < 2 microns after 40,000 hours of operation in case of H230 substrate.

6) A comparison of the measured k_c from the present work and literature shows that LTM perovskite as a coating material is a factor of ~23 superior to Mn-Cr spinel.
7) Unlike H230 and INC718, SS430 exhibits aggressive oxidation kinetics and therefore thicker coating by dip coating technique was deposited on the substrate. Dip coated SS430 sample annealed at 1000^0C under applied pressure exhibited less porosity than one without application of pressure. And porosity further decreased after 168hours of oxidation studies.
8) Oxidation studies on uncoated H230 and H230 with 1 micron thick coatings of LC, and LNC were conducted in reducing atmosphere for up to 2160 hours at 800^oC. Uncoated sample exhibited the largest oxide scale thickness (~3.18 microns), followed by LC-coated (~ 1.07microns), LNC-coated (~0.94 microns), The lowest oxide scale thickness for LNC-coated H230 suggests than LNC exhibits the lowest oxygen ion conductivity of the materials studied here, in accord with defect chemistry.
9) The kinetic parameter, k_c, which governs transport through coating and thereby dictates its protectiveness against oxidation was the lower for LNC ($k_c \approx 2.6410^{-15}$ cm^2/s), and higher for LC ($k_c \approx 3.24 \times 10^{-15}$ cm^2/s), in accord with defect chemistry.
10) The area specific resistance (ASR) of the samples, which predominantly reflects the ASR of the oxide scale, was measured on uncoated and coated samples. The LNC-coated H230 exhibited the lowest ASR while the uncoated H230 exhibited the highest ASR, in accord with defect chemistry.
11) Out of all coating materials studied (LM, LSM, LTM, LC, LNC) LNC showed the lowest ionic conductivity in reducing atmosphere.
12) 10 to 15 microns thick coating of LTM on cathode side and 1 to 5 microns thick LNC coating on anode side is required for optimum results.
13) Ionic conductivity of interconnect coating materials (LSM/LM/LTM) was measured by using electron blocking electrode technique (Hebb-Wagner polarization technique). It was observed that thickness of the sample plays an important role in achieving the steady-state condition as the oxygen ion conductivity of samples is very low. Thus, thin sample gave more accurate and lower value than thicker one. Lowest value of ionic conductivity ($2.2 \text{x} 10^{-7}$) was recorded in sputter-deposited couple where thickness of the sample was around 1.5 microns. LM sample showed higher ionic conductivity value followed by LSM. This also supports our hypothesis of defect chemistry i.e. when LM is doped with higher valent ion, say Ti, it's ionic conductivity decreases and when doped with lower valent ion , say Sr, its ionic conductivity increases.

LIST OF FIGURES

.

REFERENCES:

1. K. Hipert, W. J. Quadakkers, and L. Singheiser, *Handbook of fuel cells*, **4**(8), 1037-1054 (2003).
2. K. Yoshida, T. Hashimoto, Y. Inagaki, H. Tagawa, and M. Dokiya, *Electrochem. Soc. Proceedings*, **19**, SOFC-VI, 657-665 (1999).
3. S. W. Paulik, S. Baskaran, and T. R. Armstrong, *J. Materials Science*, **33**, 2397-2404 (1998).
4. T. Hashimoto, T. Nakamura, Y. Matsui, T. Katsube, and T. Suyama, *Electrochem. Soc. Proceedings,* **16,** SOFC-VII, 820-827 (2001).
5. E. Konyesheva, H. Penkalla, E. Wessel, J. Mertens, U. Seeling, L. Singheiser, and K. Hilpert, *J. Electrochem. Soc.*,**153**(4), A765-A773 (2006).
6. K. Hilpert, D. Das, M. Miller, D. H. Peck, and R. Weib, *J. Electrochem. Soc*., **143**(11), 3642-3647 (1996).
7. C. Gindorf, K. Hilpert, and L. Singheiser, *Electrochem. Soc. Proceedings*, **16**, 793-802 (2001).
8. T. Brylewski, M. Nanko, T. Maruyama, and K. Przybylski, *Solid State Ionics*, **143**, 131-150 (2001).
9. J. Piron Abellan, V. Shemet, F. Tietz, L. Singheiser, and W. J. Quadakkers, *Electrochem. Soc. Proceedings*, **16**, 811-815 (2001).
10. J. Pu, and J. Li, *J. Power Sources*, **158**(1), 354-360 (2006).
11. S. P. Jiang, S. Zhang, and Y. D. Zhen, *J. Materials Research*, **20**(3), 747-758 (2005).
12. Z. Yang, J. S. Hardy, M. S. Walker, G. Xia, S. P. Simner, and J. W. Stevenson, *J. Electrochem. Soc.*, **151**(11), A1825-A1831 (2004).
13. D. M. England, and A. Virkar, *J. Electrochem. Soc.*,**146**(9), 3196-3209 (1999).
14. D. M. England, and A. Virkar, *J. Electrochem. Soc.*,**148**(4), A330-A338 (2001).
15. J. Li, J. Pu, X. Jianzhong, and Q. Xiaoliang, *J. Power Sources*, **139**, 182-187 (2005).
16. G. A. Greene, and C. C. Finfrock, *Oxidation of Metals*, **55**(5/6), 505-521 (2001).
17. S. J. Geng, J. H. Zhu, and Z. G. Lu, *Solid State Ionics*, **177**, 559-568 (2006).
18. J. H. Chen, P. M. Rogers, and J. A. Little, *Oxidation of Metals*, **47**(5/6), 381-410 (1997).
19. G. M. Ecer, and G. M. Meier, *Oxidation of Metals*, **13**(5), 119-158 (1979).
20. S. Taniguchi, M. Kadowaki, H. Kawamura, T. Yasuo, Y. Akiyama, Y. Miyake, and T. Saitoh, *J. Power Sources*, **55**, 73-79 (1995).
21. Y. Matsuzaki, and I. Yasuda, *J. Electrochem. Soc*., **148**(2), A126-A131, (2001).
22. Y. Larring and T. Norby, *J. Electrochem. Soc*., **147** (9) 3251-3256 (2000).
23. J. Kim, R. Song, and S. Hyun, *Solid State Ionics*, **174**, 185-191 (2004).
24. T. J. Armstrong, M. Smith, and A. V. Virkar, in SOFC-IX, edited by S. C. Singhal and J. Mizusaki, Proceedings Volume 2005-07, p. 1795-1805 (2005).
25. Z. Yang, G. Xia, and J. W. Stevenson, *Electrochem. and Solid State Lett.*, **8**(3), A168-A170 (2005).
26. Z. Yang, G. Xia, S. P. Simner, and J. W. Stevenson, *J. Electrochem. Soc*., **152**(9), A1896-A1901 (2005).

27. X. Chen, P. Y. Hou, C. P. Jacobson, S. J. Visco, and L. C. De Jonghe, *Solid State Ionics*, **176**, 425-433 (2005).
28. D. J. Fisher, 'Defect and Diffusion Forum: Diffusion in Ceramics – 10 Years of Research', Scitec Publications, Volumes 169-170 (1999).
29. J. Jue, J. Jusko, and A. Virkar, *J. Electrochem. Soc*., **139**(9), 2458-2465 (1992).
30. J. H. Kuo, H. U. Anderson and D. M. Sparlin, *J. Solid State Chemistry*, **83**, 52-60 (1989).
31. S. J. Kim, Z. C. Chen and A. V. Virkar, *J. Am. Ceram. Soc.*, **71** (10) C428-C432 (1988).
32. S. Gopalan and A. V. Virkar, *J. Am. Ceram. Soc*., **82** (10) 2887-2899 (1999).
33. O. Muller and R. Roy, '*The Major Ternary Structural Families*', Springer-Verlag, Berlin (1974).
34. F. H. Lu and R. Dieckmann, *Solid State Ionics*, **67** 145-55 (1993).
35. I. Saeki, T. Saito, R. Furuichi, H. Konno, T. Nakamura, K. Mabuchi, and M. Itoh, Corrosion Sci., 40-8, 1295-1302 (1998).
36. I. Yasuda, T. Ogiwara, and H. Yakabe, SOFC VII, eds. H. Yokokawa, and S. C. Singhal, *Electrochem. Soc. Proceedings*, **2001-16**, 783 (2001).
37. I. Yasuda, and M. Hishinuma., **143**, 1583 (1996).
38. I. Yasuda, and T. Hikita, Proc. 2nd Int. Symp. on SOFC, eds. F. Groaa, P. Zeggers, S. C. Singhal, and O. Yamamoto, *Comission of European Communities, Report EUR* 13564 EN, Athens, 645 (1991).
39. A. C. S. Sabioni, B. Lesage, and A. M. Huntz, *Philos. Mag. A,* **66,** 333 (1992).
40. P. Kofstad, and K. P. Lillerud, *Oxid. Met*., **17**, 177 (1982).
41. I. Brian, *Thermodynamical Data of Pure Substances,* VCH Publications (1989).
42. A. Holt, and P. Kofstad, *Solid State Ionics*, **69**, 127 (1994).
43. D. M. England, A. V. Virkar, *J. Electrochem. Soc.,* **148**(4), A330-A338 (2001).
44. I. Yasuda, K. Ogasawara, M. Hishinuma, T. Kawada, and M. Dokiya, *Solid State Ionics,* **86-88**, 1197-1201 (1996).
45. I. Yasuda, and M. Hishinuma, *J. Solid State Chem.*, **115**, 152-157 (1995).
46. H. Tagawa, N. Mori, H. Takiya, Y. Yonemura, H. Minamiue, H. Inaba, J. Mizusaki, and T. Hashimoto, Proc. Of the 5th Int. Symp. on SOFC-V, Germany, *Electrochem. Soc. Proceedings***, 97-18**, 785 (1997).
47. J. H. Kuo, H. U. Anderson, and D. M. Sparlin, *J. Solid State Chem.*, **83**, 52-60 (1989).
48. I. Riess, *Solid State Ionics*, **44**, 199-205 (1991).
49. I. Riess, *Solid State Ionics*, **51**, 219-229 (1992).
50. I. Riess, *Solid State Ionics*, **66**, 331-336 (1993).
51. I. Riess, *Solid State Ionics*, **91**, 221-232 (1996).
52. W. L. Worell, *Solid State Ionics*, **52**, 147-151 (1992).
53. U. B. Pal and S. C. Singhal, *J. Electrochem. Soc*., **137**(9), 2937 (1990).
54. A. Belzner, T. M. Gur, and R. A. Huggins, *Solid State Ionics*, **57**, 327-337 (1992).
55. I. Yasuda, and M. Hishinuma, *J. Solid State Chem*., **123**, 382-390 (1996).
56. I. Yasuda, K. Ogasawara, M. Hishinuma, T. Kawada, and M. Dokiya, *Solid State Ionics*, **86-88**, 1197-1201 (1996).

LIST OF ACRONYMS AND ABBREVIATIONS

ASR:	Area specific resistance
DC:	Direct current
EMF:	Electromotive force
LC:	$LaCrO_3$
LM:	$LaMnO_3$
LMT:	Ti-doped $LaMnO_3$
LNC:	Nb-doped $LaCrO_3$
LSM:	Sr-doped $LaMnO_3$
NDA:	Non disclosure agreement
OFHC:	Oxygen free high conductivity
RF:	Radio frequency
SECA:	Solid-state Energy Conversion Alliance
SEM:	Scanning electron microscope or microscopy
SS430:	Stainless steel 430
XRD:	X-ray diffraction
YSZ:	Yttria-stabilized zirconia